

ANALYSIS AND DESIGN OF ARTICULATE NEUROENDOSCOPIC INSTRUMENTS USING
CONTACT-AIDED COMPLIANT MECHANISMS

by

Kyle W. Eastwood

A thesis submitted in conformity with the requirements
for the degree of Doctor of Philosophy
Institute of Biomaterials and Biomedical Engineering
University of Toronto

Abstract

Neuroendoscopy is a form of minimally invasive brain surgery that uses millimeter sized instruments and long, thin cameras to safely access deep brain structures. These procedures significantly reduce morbidity and blood-loss as surgeons operate through small, centimetre sized, incisions. However, the design of present instruments limit the scope of diseases that can safely be treated using these techniques. Specifically, present hand-held tools lack dexterity at their tip, which prevents surgeons performing the same range of maneuvers that are used in classic, open microsurgery.

This manuscript describes the development of hand-held wristed tube-shaft instruments designed to expand the dexterity of current neuroendoscopic tools. The specific tools described herein are designed to allow surgeons to perform a combined endoscopic third ventriculostomy (ETV) and endoscopic tumor biopsy (ETB) procedure from a single incision. This procedure requires surgeons to access two distinct targets located near the center of the brain, and completing this maneuver from a single opening in the skull is very challenging. Here, an analysis of this clinical problem has been simulated using three-dimensional models generated from magnetic resonances (MR) images of patients from the Hospital for Sick Children. This analysis generates important design specifications for the development of dexterous neuroendoscopic instruments.

Following the work-space analysis, an investigation of the design and optimization of a tube-shaft joint mechanism is described, considering surgical task and workspace requirements specific to neurosurgery. This study has led to the development of a novel contact-aided compliant joint mechanism that addresses a significant design challenge encountered in neuroendoscopic tissue manipulation. Namely, the trade-off in joint stiffness and range-of-motion when developing tube-shaft compliant joints at the millimeter scale. Here, we present a novel notch design with an accompanying kinematics and statics model. These models are verified using experimental results of physical prototypes in addition to finite element models for the mechanism.

The joint design is incorporated into a hand-held neuroendoscopic instrument and the reach and function of the instrument is compared to the original simulation based design specifications. This work concludes with preliminary testing of the instrument using phantom models, and a description of the potential applications and future directions of the project.

Contents

1	Introduction	1
1.1	Chapter Overview	1
1.2	Neuroendoscopy	1
1.2.1	The Current State of Neuroendoscopy	2
1.2.2	The Neurosurgical Operating Environment	3
1.2.3	Neurosurgical Technology Under Development	5
1.3	Thesis Overview	10
1.3.1	Purpose	10
1.3.2	Thesis Organization	10
1.4	References	11
2	Design Optimization of Neuroendoscopic Instruments	15
2.1	Abstract	15
2.2	Introduction	15
2.3	Prior Work	16
2.4	Geometric Modelling	16
2.4.1	Anatomical Model	16
2.4.2	Instrument Kinematic Model	17
2.5	Problem Definition	17
2.5.1	Method Inputs	18
2.5.2	Penalty Functions	19
2.5.3	Optimizing Surgical Incision and Orientation	20
2.5.4	Algorithm	20
2.6	Numerical Example	21
2.7	Conclusion	22
2.8	References	22
3	Design of Flexible Instruments for Combined ETV-ETB	24
3.1	Abstract	24
3.2	Introduction	25
3.3	Methods	26
3.3.1	Patient Selection	26
3.3.2	Imaging	26
3.3.3	Anatomical Measurements and Analysis	26

3.3.4	Virtual Instrument Measurements and Analysis	29
3.4	Results	30
3.4.1	Anatomical Measurements	30
3.4.2	Virtual Instrument Measurements	31
3.5	Discussion	31
3.6	Conclusion	34
3.7	References	34
4	Kinetostatic Design of Asymmetric Notch Joints for Surgical Robots	36
4.1	Abstract	36
4.2	Introduction	36
4.3	Review of Prior Modelling	37
4.4	Problem Definition	39
4.5	Model Development	39
4.5.1	Development of Force-Deflection Model	40
4.5.2	Modelling Non-Prismatic Second Moment of Area	40
4.5.3	Beam Deflection Using Castiglianios Second Theorem	42
4.6	Model Validation	43
4.6.1	Validation of Force-Deflection Model	43
4.6.2	Sensitivity Analysis	46
4.7	Experimental Implementation	48
4.7.1	Problem Definition	48
4.7.2	Development of a Task-Specific Surgical Wrist	49
4.8	Conclusion	51
4.9	References	51
5	Design of CCM Notched-Tube Joint	53
5.1	Abstract	53
5.2	Introduction	53
5.3	Proposed Design of CCM Notched-Tube Joint	56
5.4	Prototype Development with a Focus on Neuroendoscopic Instrument Design	57
5.4.1	Finite Element Modelling for Contact-Aid Sizing	58
5.4.2	Simulation Results of Contact Aid Sizing	59
5.5	Modelling Joint Behavior	61
5.5.1	Kinematics Modelling	61
5.5.2	Statics Modelling	62
5.6	Fabrication of Notched-Tube Joint Prototypes	65
5.7	Experimental Methods	65
5.7.1	Force-Deflection Testing	65
5.7.2	Range-of-Motion Testing	66
5.8	Experimental Analysis and Model Validation	67
5.9	Discussion	68
5.10	Conclusion	71
5.11	References	72

6 Developing A Dexterous Neuroendoscopic Instrument	74
6.1 Abstract	74
6.2 Introduction	74
6.3 Design and Prototyping of Articulate Neuroendoscopic Instrument	75
6.3.1 Overall Instrument Design	76
6.3.2 Design of Instrument Tube-Shaft and Steerable Tip	76
6.3.3 Design of Control Handle	77
6.3.4 Instrument Prototyping	78
6.4 Kinematic Analysis	80
6.4.1 Kinematic Model and Frame Convention	80
6.4.2 Validation of Kinematics Model	81
6.5 Task Specific Analysis of ANI Performance	82
6.5.1 Patient Data	82
6.5.2 Comparison of ANI Geometry to Design Requirements	83
6.5.3 ANI Reachability Assessment	83
6.6 Surgical Task Simulation	84
6.6.1 Surgical Task Results	85
6.7 Discussion	85
6.8 Conclusion	88
6.9 References	88
7 Summary	90
7.1 Overview	90
7.2 Overview of Contributions and Limitations of Proposed Technology	90
7.2.1 ETV-ETB Specific Articulate Neuroendoscopic Instruments	90
7.2.2 Notched-Tube Contact-Aided Compliant Joints	92
7.2.3 Instrument Handle Design	93
7.3 Next Steps in Instrument Development	94
7.3.1 Multi-Instrument Design Considerations	94
7.3.2 Navigation and Procedure Planning	94
7.3.3 Biocompatibility	95
7.3.4 Education and Training	95
7.3.5 Intellectual Property and Commercialization	96
7.4 Future Research Projects	96
7.4.1 Neurosurgical Instrument User Feed-back Study	96
7.4.2 Development of a Contact-aided Compliant Joint Robotic Prototype	97

List of Tables

2.1	Burr Hole Positions Relative to Skull Landmarks	22
2.2	Section Radii of Curvature and Lengths	22
3.1	Summary of Patient Demographic Data ^a	27
3.2	Summary of MR Imaging Data ^a	27
3.3	Summary of CT Imaging Data	28
3.4	Comparison of Anatomical Measurements	30
3.5	Angular Orientation of the Foramen of Monro	31
3.6	Comparison of Surgical Incision Locations	31
3.7	Virtual Tissue Shift Compared by Burr-Hole Location	32
3.8	Estimated Geometry of Dexterous Instruments by Burr-Hole Location	32
4.1	Summary of Test Sample Geometry	45
4.2	Bounds for Simulation Parameters	47
5.1	Rectangular Notch Joint Geometry Used as Starting Point for Design	58
5.2	Constitutive Model of Nitinol	58
5.3	Constitutive Model of Steel	58
5.4	Selected Contact-Aided Joint Parameters (Labelled in Fig. 5.5)	61
5.5	Constitutive Model Used with MATLAB Simulation	68
6.1	Summary of Instrument Shaft Geometry	79
6.2	Comparison of Design Specifications to ANI Geometry	83
6.3	Simulated Joint Value Ranges	84

List of Figures

1.1	Standard neuroendoscopic instruments and approach	2
1.2	Images of NRBTR, Neurobot and Evolution 1 Neurosurgical Robots	7
1.3	Images of Compliant Joint Neurosurgical Robots and Instruments	9
2.1	Notation for Space Curve	17
2.2	Mark-up GUI in MATLAB	19
2.3	Optimal Instrument Configuration	21
3.1	Patient Models in MATLAB	28
3.2	Surgical Targets for ETV and ETB	30
4.1	Prototype Surgical Instrument	37
4.2	Cutting Parameters of Notched Tube Joint	39
4.3	Asymmetric Notched Tube Joint Transformations	40
4.4	Asymmetric Notched Tube Joint Cross-section	41
4.5	Asymmetric Notched Tube Joint Circular Segment Geometry	41
4.6	Joint with loading notation for Castigliano Model.	43
4.7	MATLAB Simulation of Joint Deflection	44
4.8	Testing and fabrication of test sample (1.3 mm Diameter)	45
4.9	Plot of % Error between Model and Experimental Results	46
4.10	Scatter Plot of Parameters for Force-Displacement Model	47
4.11	Scatter Plot of Parameters for Kinematics Model	48
4.12	Two-Tube Active Cannula Design Space	49
4.13	Wrist Design Prototype	50
4.14	Tendon Tension and Force Deflection of Prototype	50
5.1	Examples of Notch Tube Topologies in Literature	54
5.2	Notched tube segment and tube cross-section	55
5.3	Panel of CCM Notched-tube Joint Features	56
5.4	Illustrative Example Demonstrating the Behavior of CCM Notched-tube Joint	57
5.5	Finite Element Model Constraints and Boundary Conditions	59
5.6	Finite Element Model of Contact-Aided Notched-Tube Joint	60
5.7	Sensitivity Analysis of Contact-Aid Joint Geometry h_i	61
5.8	Schematic of CCM Notched-Tube Kinematics Model	62
5.9	Schematic of CCM Notched-Tube Cross-Section Geometry	63

5.10	Ellipse segment shape fit	64
5.11	Comparison of Rectangular and Contact-Aided Notch	66
5.12	Experimental set-up for measuring blocking force and joint range-of-motion	66
5.13	Finite element and physical specimen of contact-aided joint and rectangular joint	67
5.14	Experimental and FEM Blocking Force Results	68
5.15	Comparison of Kinematics Model with Experimental and FEM Results	69
5.16	Bending angle versus cable tension for notched-tube prototypes	70
6.1	Features and design of the ANI	76
6.2	Panel depicting mapping of control motions of handle to steerable tip	77
6.3	Instrument control handle exploded assembly view	78
6.4	Primary components used to assemble the instrument control handle	79
6.5	Contact-Aided Joint Design and Kinematics	80
6.6	Place Holder for Kinematics Experiments	82
6.7	Predicted vs ANI Geometry	83
6.8	Reachable Workspace of ANI for ETV-ETB Procedure	84
6.9	Simulation Set-up for ETV-ETB using ANI	85
6.10	Endoscopic Views of Simulated ETV-ETB using ANI	86
7.1	Proposed future contact-aided notch joint	92

Chapter 1

Introduction

1.1 Chapter Overview

The purpose of this chapter is to outline the motivation behind the original research presented within this thesis. The chapter begins by describing a form of minimally invasive neurosurgery referred to as neuroendoscopy. The current state of this standard surgical approach is discussed, and the important technological limitations are highlighted. Next, an overview of the neurosurgical operating environment is described. This discussion examines the forces required to manipulate brain tissue during standard operations and also explains the anatomy encountered in common neuroendoscopic procedures. These subjects provide important context when considering new technologies that aim to address the limitations of existing tools. Following these topics, an overview of new instruments being developed to improve neuroendoscopy are presented. Subsequently, a discussion of relevant new technologies that could be used to construct new neuroendoscopic instruments is reviewed.

Chapter one concludes by presenting the aim this thesis which is to develop new dexterous surgical instruments for neuroendoscopy. Such tools are intended to provide surgeons with greater surgical access when performing endoscopic procedures. The final sections of the chapter provide a detailed overview of the organization of the thesis and the relevance of each subsequent chapter.

1.2 Neuroendoscopy

Neuroendoscopy is a form of minimally invasive brain surgery that is performed through centimeter-sized incisions. This technique utilizes miniature cameras and long, thin instruments to visualize and reach structures deep within the brain [1]. Fig. 1.1 provides an overview of this standard surgical technique. Fig. 1.1-A illustrates an example of how a trocar and instruments may be positioned with respect to a patient. The trocar is a long, cylindrical device whose tip is inserted into the brain through an opening in the skull, referred to as a burr-hole craniotomy, which is approximately 2 cm in diameter [1], [2]. The trocar consists of an optical lens assembly inside of a tube, with integrated illumination. This lens assembly is referred to as a neuroendoscope. The trocar also consists of several long, thin holes running along its length, referred to as working channels [2]. The purpose of the trocar is to provide a protected corridor through which to pass hand-held instruments to reach deep structures within the brain. A camera can be externally attached to the trocar, and the integrated neuroendoscope lens assembly allows

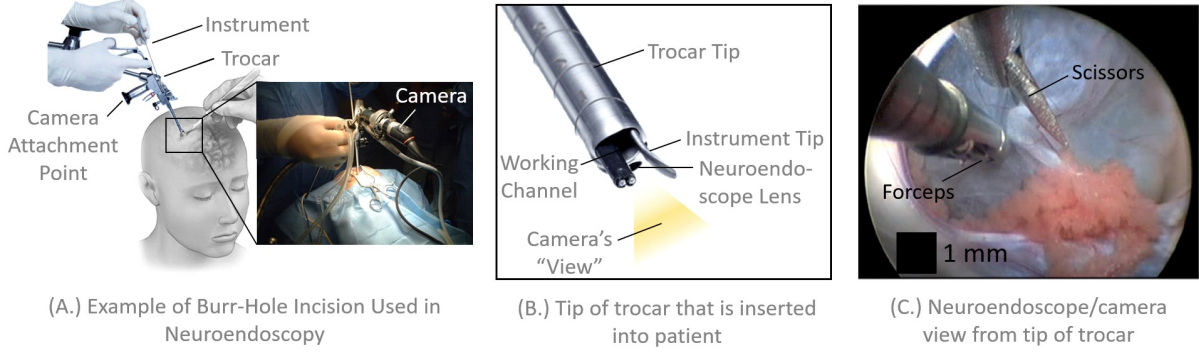


Figure 1.1: Standard neuroendoscope, trocar and semi-rigid instrument that may be used when performing an endoscopic third ventriculosotomy procedure (A). A detailed view of the tip of the trocar which is inserted inside of the brain (B). A camera view taken from a neuroendoscope inside of the lateral ventricles of the brain (C).

the camera to capture images from the perspective of the tip of the trocar. Fig. 1.1-B demonstrates how the distal ends of instruments, passing through the working channels of the trocar, appear at the tip of the trocar. These instruments exit the trocar directly adjacent to the neuroendoscope lens, and therefore appear in the cameras field-of-view. Some common instruments used for neuroendoscopy include forceps and scissors, which have a tube-shaft design that ranges between 1 mm to 2 mm in diameter and approximately 30 mm in length [1], [2]. Fig. 1.1-C depicts the camera view as seen from a trocar tip inserted inside the cerebral ventricles. Generally, the images from the neuroendoscope and camera are projected onto a digital display which allows neurosurgeons to view the motions of their tools in real-time.

The most frequently used types of endoscopes and trocars in neurosurgery are rigid lens endoscopes, but semi-rigid mini-fiberscopes, flexible fiberscopes, and video-endoscopes (distal chip) also exist [3]. These devices differ from rigid lens endoscopes in that the endoscope and working channels are steerable, allowing the surgeon to change the viewing direction of the camera.

1.2.1 The Current State of Neuroendoscopy

In 2011, Qiao *et al.* conducted a study to determine the major trends in operative techniques for the treatment of intraventricular tumors [4]. This work provides a variety of pertinent information with regards to the state of the art in neuroendoscopic techniques, based on a survey of 15 experts with a total of 264 years of cumulative experience. This study also identified the technological limitations of existing equipment, highlighting important unmet needs. In the study, the authors begin by discussing the most important features of the most commonly used endoscopes and trocars. For example, most respondents prefer neuroendoscopes with diameters less than 2 mm and trocars that have diameters less than 6 mm. Additionally, most surgeons favored trocars with working channels in the 1-3 mm range, with larger sizes being preferred in order to more easily facilitate the bulk removal of tumors. Further, the study confirmed that the majority of surgeons prefer to use rigid endoscopes because of their superior image quality. These findings are consistent with the example surgical work-flow depicted in Fig. 1.1. This information is very relevant to the development of new instrumentation to address current technological limitations, as it provides valuable design guidelines and constraints.

In terms of instrumentation, Qiao *et al.* found that at least eighty-five percent of surgeons routinely use cupped biopsy forceps, suction and aspiration, scissors and grasping forceps. However, the survey also highlighted that existing instruments must be improved to facilitate bimanual operation, which was indicated as *most important* by sixty-seven percent of respondents [4]. Current instruments are restricted to articulating in a straight-line (linear) trajectory from the tip of the trocar. This motion limitation creates several practical problems for bimanual instrumentation. First, the inability to triangulate the tools creates a situation in which the instrument bodies block the field of view of the camera. Second, without a distal joint at the instrument tip, the co-linear nature of the trocar working channels prevents instrument tips from being opposed together, which is a necessary motion for complex tissue manipulation.

A similar qualitative survey was conducted in 2013 by Marcus *et al.* where forty expert neurosurgeons, specializing in neuroendoscopic techniques, were asked to comment on technological barriers and future technological advances within the field [3]. This more recent survey captured the resurgence of interest in endoscopic and keyhole approaches as alternatives to microsurgical techniques. Effectively, surgeons are using this technology more frequently in new applications in order to achieve the goal of accessing deep structures through the narrowest practical approach, while maximizing effectiveness and efficacy [1]. However, with this trend, addressing the dexterity limitations of existing equipment identified by Qiao *et al.* becomes even more important. The findings of Marcus *et al.* agree with the earlier results found by Qiao *et al.* In particular, addressing challenges in manipulation was the theme most frequently identified by the forty participants as key to developing more efficacious and safe neuroendoscopic approaches. To summarize the results, "currently available instruments do not allow for dissection in the same way as conventional microsurgical approaches, reducing surgical dexterity to largely co-axial control through narrow corridors, and often limiting neurosurgeons to single-handed manipulation" [3].

Both of the surveys in [3] and [4] indicate that the present performance of manual tools is hindered by a lack of dexterity in their design. Current standard neuroendoscopic instruments are semi-rigid and straight which require surgeons to operate in a straight-line direction from the tip of their trocars. Further, both rigid-lens and flexible or steerable endoscopes are subject to this limitation. Although this constraint has been an accepted standard for decades, these operating conditions pose ergonomic problems for the surgeons, and importantly, make even geometrically *simple* tasks very challenging and time consuming. These observations indicate a need for new instruments with increased dexterity in order to continue to advance the scope of intraventricular endoscopic surgery [1]. Improving the reach and dexterity of standard instruments will continue to allow surgeons to apply this technology in new and innovative ways.

1.2.2 The Neurosurgical Operating Environment

Neuroendoscopic instrumentation is among the smallest and most delicate of surgical instruments. These tools are specially designed to be stiff and durable enough to manipulate brain tissue while also being compact enough to fit within small volumes inside of the brain. The development of effective new instruments, capable of addressing the technological limitations of current tools, is contingent on a thorough understanding of the forces required to manipulate brain tissue and the size of the workspaces in which the tools must fit.

Operating Forces

Several studies have been conducted to understand the forces required to manipulate brain tissue during neurosurgery. These investigations began very generally by studying animal tissues using simple penetration tasks, and over time, have come to study the forces needed for specific surgical manipulation maneuvers using cadaveric and live human brain.

Initially, many investigators have focused on determining the mechanical properties of the brain, with the aim of developing constitutive models that could predict manipulation forces. For example, Walsh *et al.* used a diaphragm pressure sensor to measure the non-linear response of brain tissue in dogs [5]. Subsequently, Miller *et al.* developed a hyper-viscoelastic constitutive model and compared the models predictions to a porcine brain. This work found that 0.3 N were required to displace brain tissue 4 mm during retraction [6]. However, the properties of brain tissue have been demonstrated to vary both regionally and also depend on the surgical task being performed [7]. Therefore, investigators interested in developing surgical devices have instead focused on measuring the forces required to perform specific tasks. Here, initial work has focused on performing basic penetration tasks. Howard *et al.* measured the penetration forces on 2.5 mm spheres and the drag forces on a 3 mm ventricular catheter advanced 20 mm to 30 mm deep within porcine brain tissue [8]. These experiments elicited forces in the range of 0.08 N and 0.03 N, respectively.

More recently, a series of studies have investigated more relevant surgical tasks such as the blunt and sharp dissection of cadaveric human brain tissue. Marcus *et al.* conducted several microsurgical dissections on two fresh human cadaveric brains, performing coagulation with bipolar cautery on tissues in the cerebrum, cerebellum and brain stem, as well as completing a corpus callosotomy and perforating the floor of the 3rd ventricle [7]. Forces were recorded as this tissue was cut and retracted, where a stab incision required 0.01 N, a carrying incision required 0.05 N, and retracting required 0.08 N. Regional differences were significant between the brain stem, with a median cutting force of 0.05 N, compared to the cerebellum with a median cutting force of 0.02 N and the cerebrum with a median cutting force of 0.03 N. The median force during blunt dissection was 0.22 N compared to 0.03 N for sharp dissection when dissecting the circle-of-willis. Similarly, Maddahi *et al.* performed over fifty different microsurgical grasping and bipolar maneuvers on a previously frozen human cadaveric brain [9], [10]. Here, the mean force recordings varied in the range of 0.42 N to 1.5 N, and included the opening of the liliquist membrane, dissection of vessels and coagulation of the dura, to name a few.

Subsequently, researchers have also recorded the forces required for brain dissection tasks during live surgery in humans. Bekeny *et al.* conducted a studying using a six degree-of-freedom force sensor attached to a Hardy transsphenoidal bayonet ring curette, and recorded the forces during three in vivo skull-base pituitary surgeries. In this study, the forces were reported in components in the [X,Y,Z] directions [11]. Here, the Z-axis aligns with the long axis of the instrument, and the X-axis and Y-axis are orthogonal to the shaft. The mean forces recorded for soft tissue interactions were 0.097 0.088 N, 0.12 0.096 N and 0.13 0.094 N, for X, Y and Z respectively. Finally, Sugiyama *et al.* analyzed the forces encountered in arteriovenous malformation surgery in two living human patients to determine the safe force cut-off limits for training and medical education purposes [12]. The two surgeries were performed by an expert surgeon, and force data was acquired for 251 and 332 trial maneuvers using bipolar forceps equipped with strain gauges. A total of 474 successful coagulation maneuvers were completed with mean forces of 0.23 0.06 N and maximum forces of 0.35 0.11 N. A receiver-operator-curve was used to determine safe force cut-offs limits, before damaging tissue, of 0.299 N for mean force and 0.457 N for

peak force.

Ultimately, these series of studies indicate that the forces required for brain tissue manipulation range between 0.01 N to 0.5 N, with mean forces for the sharp dissection of soft tissue ranging from 0.1 N to 0.2 N. This data provides an indication of the loads that new surgical instruments must be capable of transmitting in order to perform neurosurgical maneuvers.

Operating Workspace

Understanding the size of the surgical workspace in which neuroendoscopic instruments are used is necessary for the design of new tools. The most common procedures currently performed using neuroendoscopic instruments are either intraventricular or endonasal transsphenoidal approaches [3].

In the case of intraventricular procedures, the trocar is used to access a naturally occurring, fluid filled cavity within the center of the brain referred to as the cerebral ventricles. The tip of the trocar is placed such that the instrument tips are free to move inside of this volume and the neuroendoscopes field-of-view can visualize the inside of the ventricles. In this manner, the trocar acts as a protective corridor connecting the outside of the patients body, through the burr-hole craniotomy, to the fluid filled ventricle cavity. While the surgeon operates, the trocar protects healthy brain tissue which is easily injured and has limited ability to regenerate. By navigating through the volume of the ventricles, surgeons can access pathologies located deep within the center of the brain while disrupting a minimal amount of healthy brain tissue. Further, because the ventricles are centrally located and span over large regions of the brain, many vital structures can be accessed by making small incisions through the floor, walls or roof of the ventricles. Ultimately, neuroendoscopic instruments are designed to fit within the volume of the ventricles without making any undesired contact with the healthy brain tissue that makes up the ventricle's floor, walls or roof.

A study by Morgenstern *et al.* reported the geometry of some key landmarks inside of a region of the ventricles referred to as the third ventricle [13], [14]. The third ventricle is adjacent to some of the most centrally located regions of the brain, and it is where one of the most common neuroendoscopic procedures is performed. An endoscopic third ventriculostomy (ETV) is a standard surgical maneuver used to treat hydrocephalus, an enlargement of the fluid spaces of the brain, and it is one of the most common current applications of neuroendoscopic instruments. In the study, Morgenstern *et al.* describe the approximate height, width and length of this volume, and also describe the shape and size of other obstacles that naturally exist in this space. Similar studies have also been published by Knaus *et al.* and Zhu *et al.* [15], [16]. Ultimately, these reports describe an operative volume with length, width and height dimensions in the range of 10 mm to 20 mm. However, these studies have all been reported in the context of using existing tools for operation, and there are few studies that have focused on the space required to fit wristed or dexterous instruments into this volume. Analyzing the shape and space requirements of wristed tools for work in the ventricles is an important question that must be addressed before new instruments can be developed.

1.2.3 Neurosurgical Technology Under Development

The difficulty in both producing and assembling articulated joints in the millimeter scale is well known. As a result of these challenges, several different strategies for developing dexterous instruments for neuroendoscopy have been pursued. The earliest and most common approaches to creating wristed

instruments have arguably been the most complex. For example, the first wristed neuroendoscopic instrument designs published are teleoperated robotic platforms, built with miniaturized revolute joint mechanisms, inspired by the laparoscopic surgical robot da Vinci, developed by Intuitive Surgical. These systems have been slow to translate into clinical practice, and new mechanism designs using continuum and compliant based joints have been investigated to address the limitations of these robots. These technologies aim to reduce the complexity of the instruments construction to reduce fabrication costs and the need for skilled labor in assembly. More recently, developers have transitioned away from tele-operated robotic platforms and have begun to develop small, simplified hand-held tools with added dexterity. Paradoxically, robotic systems were developed for neuroendoscopy before designers attempted to improve the dexterity of manual instruments. Although jointed tube-shaft hand-held instrument designs have been successfully adopted in laparoscopy to reduce tool collisions and provide triangulation, much of this technology does not effectively reduce in size from 5 mm to 1 mm diameters. Therefore, new mechanism designs are actively under investigation to produce both robotic and wristed manual instruments for neuroendoscopy.

Robotic Neuroendoscopy Systems

A review paper by Karas *et al.* published in 2007 highlights the development of the first robotic instruments designed for neurosurgery [17]. This study assesses several brain and spine applications, and describes some of the first neuroendoscopy inspired systems. Three similar papers have been published following this initial article, providing periodic updates to the state-of-the-art in neurosurgical robotics. The first study by Kronreif *et al.*, published in 2012, focuses on robotic assistance in neurosurgery, the second study by Di Ieva in 2009 discusses micro-technologies in neurosurgery, and the third study by Marcus *et al.*, published in 2014, focuses on robotic systems in keyhole and endoscope assisted neurosurgeries [18][20]. Each of these reviews cover the following systems in detail.

The Neurobot system is a minimally invasive teleoperated robotic platform, first described in 2002 by Koyama *et al.* and shown in Fig. 1.2 [21], [22]. The slave robot consists of a 10 mm diameter trocar with an integrated 3D neuroendoscope and three micromanipulators. The micromanipulators are constructed using traditional pin joints, actuated with ultrasonic motors, and are each capable of articulating in three degrees-of-freedom. This system is tele-operated by a surgeon using a master console in a similar configuration to the da Vinci robot. A very similar system, called the Neurosurgical Robot for Brain Tumor Removal (NRBTR), was developed by Arata *et al.* and first described in 2011 [23], [24]. This system also includes a 10 mm diameter trocar with an integrated 3D neuroendoscope and three micromanipulators. Each of the micromanipulators include two degrees-of-freedom and are based on a pin jointed mechanism design. In the review by Marcus *et al.*, the limitations of both the Neurobot and NRBTR robotic manipulators are discussed [20]. First, the 10 mm trocars used in these systems are considered too large. Second, the micro-manipulators, with only two and three degrees-of-freedom, have limited maneuverability and a restricted workspace. Considering the cost and complexity of their design, the number of degrees-of-freedom of these tools are comparable to the wristed manual instruments developed for laparoscopy. This similarity raises questions about the need for a robotic design. Further, the joint mechanisms are constructed from many small components that require skilled labor to assemble. Therefore, these mechanisms can be both challenging and costly to fabricate.

The Evolution 1 robot is a supervisory controlled stereotactic robot designed for microsurgery that has recently been adopted for neuroendoscopy [25]. This system is based on a pin-jointed Steward-Platform

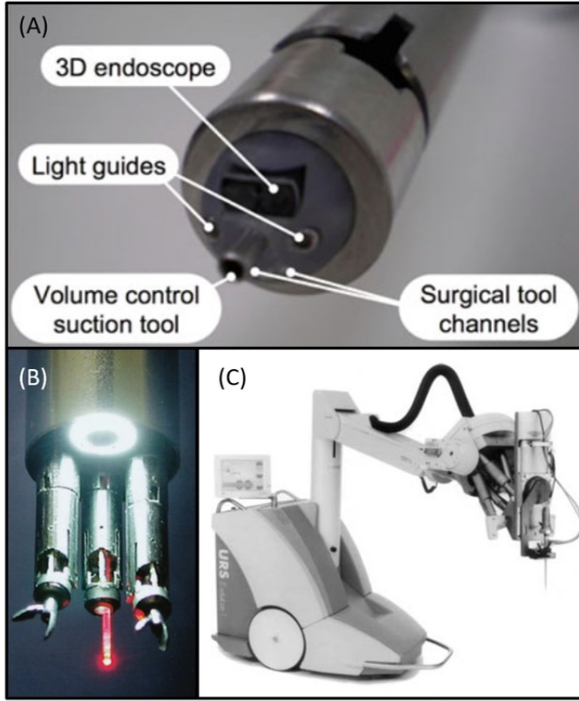


Figure 1.2: Published Images of the Neurosurgical Robot for Brain Tumor Removal [23-24] (A), The Neurobot [21-22] (B) and the Evolution 1 [25](C)

design with six degrees-of-freedom, and it has been used to position and hold a neurosurgical trocar. Although this system does not possess any micro-manipulators intended to create wristed neuroendoscopic tools, it does aim to increase the dexterity of neurosurgeons when performing neuroendoscopic procedures. By more precisely positioning and controlling the orientation of the trocar tip, neurosurgeons can maximize the performance of existing manual tools without modifying their design. A similar robotic trocar surgical assistant was developed by Kang *et al.* where a seven degree-of-freedom Kuka robotic arm was used to position a standard neuroendoscope [26]. This system was based on a master-slave configuration where one surgeon tele-operates the Kuka to position the neuroendoscope and trocar, and a primary surgeon operates at the patient-side through the robotically positioned trocar. While these approaches do improve surgical manipulation, they do not directly address the challenges of instrument collisions, or the goal of developing neuroendoscopic instruments capable of bimanual operation similar to microsurgery.

There are also several relevant micro-neurosurgical robotic systems that have been developed. These robots are similar to the Neurobot in that they are teleoperated and include multiple pin-jointed micro-manipulator wrist instruments. However, these systems are not integrated into trocar configurations and therefore have limited applicability to neuroendoscopy. These systems include the Neuroarm developed by Sutherland *et al.* [27], the Steady-Hand microsurgical robot developed by Mitsuishi *et al.* [23], the MM-1 robot developed by *et al.* [23], and a meso-scale SMA-actuated MRI-compatible robot developed by Ho *et al.* [28]. It is also worth noting that Marcus *et al.* have studied the da Vinci surgical system for use in keyhole neurosurgical operations [29]. All of these systems share similar limitations in that the joint mechanisms are complex, costly to produce and challenging to assemble. Additionally, many of the microsurgical robots are too large for neuroendoscopic applications.

To address some of the limitations of miniature pin-jointed mechanisms, concentric tube robots have been investigated for neuroendoscopy applications [30][35]. These robots are based on a compliant joint design and typically consist of two or three pre-curved super-elastic tubes assembled together concentrically. Compliant joints are mechanisms consisting of a single part that elastically bends and deforms in shape. Almost all compliant joint based designs used for medical devices are constructed from a nickel-titanium alloy called nitinol. This metal has an elastic strain limit in the range of four to eight percent, and therefore can undergo reversible deformations orders of magnitude higher than most metals. This characteristic is referred to as *super-elasticity*. To articulate concentric tube robots, the tubes are translated and rotated with respect to each other, causing them to elastically interact. These motions cause tubes of different orientation and curvature to conform to one common orientation and curvature. This operating principle is used to steer an end-effector attached to the end of the innermost tube, and create a continuously bending wrist similar to a tentacle or trunk. Concentric tube robots are fabricated from a small number of simple components that are easily assembled, making their design very desirable compared to pin-jointed wrists. These mechanisms are also capable of achieving a high number of degrees-of-freedom, where the redundant degrees-of-freedom can be used to avoid collision with obstacles in the workspace. An example of this technology is compared to a da Vinci Endowrist in Fig. 1.3. The complexity of motion of these devices combined with their redundant degrees of freedom are two of the major reasons why this technology is primarily controlled using tele-operated robotic master-slave systems. One of the major limitations of these devices is that for tube combinations with particularly high pre-curvatures, the manipulator tends to rapidly and unpredictably move between orientations; this phenomena is referred to as snapping [5]. Snapping is caused by static friction buildup and limits the compactness of the robots workspace. To avoid snapping, the radius of curvature of the pre-bent tubes must be several times the outer diameter of the tube itself, which requires the manipulator to take-on an elongated shape when bending to a desired orientation. Therefore, designing these manipulators for bimanual tissue manipulation to fit inside of the 3rd ventricle may be a challenge.

An alternative compliant robotic manipulator design that has been proposed for neurosurgical applications are tendon actuated systems with flexible backbones. These devices are comparable to concentric tube robots in terms of their overall diameter, but they tend to have more compact workspaces. That is to say, these designs can bend to a desired orientation while taking up a smaller foot-print. One example of such a system is a multi-backbone wristed manipulator developed by Khan *et al.* [36]. This system is constructed from a series of bundled wires bound together by spacer-disks around a central nitinol tube that comprises the back-bone. This system was specifically designed for neuroendoscopy and also operates based on master-slave teleoperation set-up. This mechanism is more complex to assemble than a concentric tube robot and is significantly more compliant which limits the forces that the end-effector can generate. Similarly, another tendon driven continuum robot with multiple links was developed by Kato *et al.* [37], [38]. This system has a series of spacer-disks that are all in direct contact with each other.

Another variation based on the tendon actuation theme is a notched-tube robot design developed by Mitsuishi *et al.* that includes a force sensing gripper [39]. The slave robot in this system is constructed from two concentric tubes, functioning as the mechanisms back-bone, that both have large sections of material removed from the tubes wall. These missing notches create regions of the tube that are more compliant in a particular bending direction. The mechanism is actuated in two degrees-of-freedom pitch and yaw using tendons routed within the tube and fixed to its distal end. A third degree-of-freedom

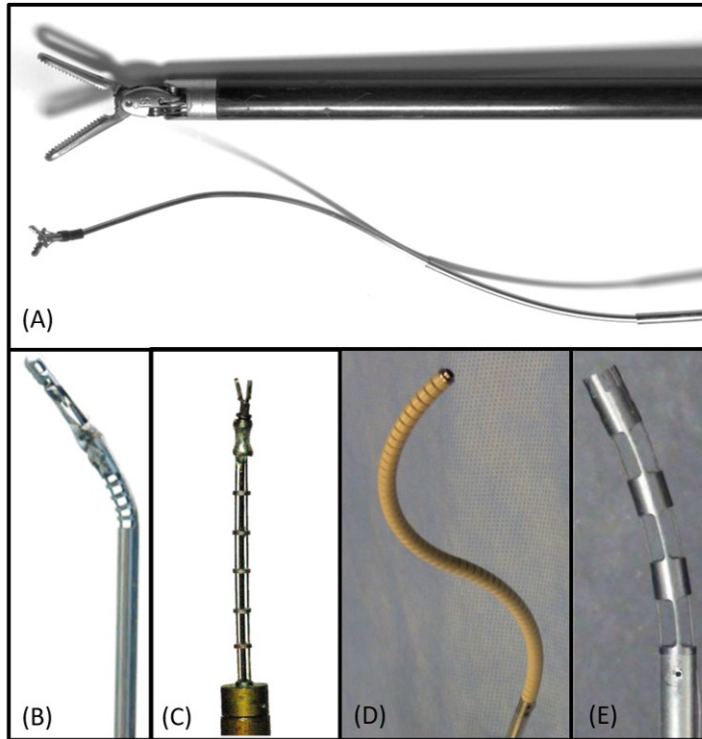


Figure 1.3: Published Images of a Concentric Tube Robot Compared to a da Vinci Endowrist (A); a Notched-Tube Joint (B); the Multi-Backbone System by Khan *et al.* [36] (C); the Multi-Backbone System by Kato *et al.* [37-38] (D); and the Notched-Tube System by Mitsuishi *et al.* [39] (E).

is achieved through rolling the mechanism about its long axis. This joint design demonstrates a well-balanced compromise between simplicity of fabrication and assembly, compact bending and the forces its end-effector can apply on tissues because of the devices overall stiffness.

Hand-Held Wristed Neuroendoscopy Instruments

Two studies have proposed the design of wristed hand-held instruments for neuroendoscopy. In 2013, Dewaele *et al.* proposed a steerable tube-shaft instrument design based on laser cut nitinol, capable of achieving three degrees-of-freedom [40]. This mechanism was proposed for both robotic and manual tool configurations, and it is physically similar to the laser-cut concentric tube design proposed by Mitsuishi *et al.* in [39]. However, the design in [40] uses three concentric laser-cut tubes, where the inner most tube is used to actuate the bending of the overall device in-lieu of using cables or tendons. Further, the laser cutting topology differs significantly between [39] and [40]. This system was tested in a phantom model and the results were assessed qualitatively. The inventors have also published a patent on the technology, but to-date, there are no further publications demonstrating its clinical use or design. Further, no details have been presented on the design of the instrument's handle.

Another notched tube-shaft wrist design was proposed by York *et al.* for applications in neuroendoscopy [41], [42]. This mechanism was developed to augment robotic manipulators while also being presented as a potential mechanism to be used in a hand-held manual tools. This design is similar to the work presented by both Dewaele *et al.* and Mitsuishi *et al.* but includes a simplified tube cutting topology that is fabricated using micro-milling instead of laser-cutting. The mechanism is capable of

achieving one degree-of-freedom in very compact bending, and is actuation by a tendon. This mechanism is an evolution from a series of designs that are based on laser-cutting nitinol to create other miniature dexterous medical instruments, such as articulated fiber-optic endoscopic cameras, articulated lasers, suction and irrigation probes, as well as wristed forceps, scissors and drills [43][49].

Overall, these notch-tube, tendon actuated, joint designs appear to be one of the most favourable new mechanisms used to increase the dexterity of minitaure tube-shaft instruments. These joints are well suited for neuroendoscopy because they achieve an excellent compromise between simplicity in both fabrication and assembly, compact bending and the output forces that the joints can transmit. However, these mechanisms have not yet been developed for a specific clinical application, and their performance while promising, has not been directly assessed compared to the performance needs of neuroendoscopy. The tissue manipulation forces required for neurosurgery, coupled with the small working volumes encountered in neuroendoscopy, create unique design challenges that may push the performance limits of these compliant mechanisms.

1.3 Thesis Overview

1.3.1 Purpose

The objective of this work is to develop a novel wrist-like actuation mechanism that can be incorporated into neuroendoscopic instruments to add additional degrees-of-freedom to the tools and enable neurosurgeons to endoscopically dissect in the same manner as conventional microsurgery.

1.3.2 Thesis Organization

Chapter two and chapter three of this thesis focus on analysing the workspace of the 3rd ventricle for performing a combined ETV and endoscopic tumor biopsy (ETB) procedure. These studies provide design guidelines that constrain the shape and size requirements for a wristed instrument. The study in chapter two was published in the 2015 IEEE Engineering in Medicine and Biology conference and describes an algorithm that places virtual instruments inside of virtual patient ventricle models, generated from medical images of patients at the Hospital for Sick Children [50]. The study in chapter three was published in the Journal of Operative Neurosurgery and describes the application of the algorithm in chapter two to fifteen different pediatric patients previously treated with a combined ETV-ETB [52]. Together, these chapters contribute the additional dimensions necessary to describe the geometry of the 3rd ventricle and importantly, they describe the shape and space requirements for new wristed instruments.

The main findings of these chapters suggest that many of the miniature articulation technologies currently being used for millimeter scale medical devices are not suitable for creating wristed neuroendoscopic instruments. The small, 10 mm to 20 mm, sizes of the instruments' workspaces require that wristed tools articulate in a very compact manner. Combining this requirement with the forces that the tools must transmit for surgical manipulation eliminates many candidate actuation technologies used in miniature medical devices.

Chapter four and chapter five are focused on studying one type of actuation mechanism that was deemed to have a high likelihood of achieving both the force output and size requirements needed for wristed neuroendoscopic tools. The actuation mechanism is referred to as a notched-tube compliant joint and can be easily incorporated into tube-shaft instruments. The study in chapter four was published

in the 2016 IEEE/RSJ International Conference on Intelligent Robots and Systems, and describes a model to predict the forces that a notched-tube compliant joint can transmit [51]. In this study, the model was examined for a range of notch-tube joint sizes and the joint's force bearing capabilities were compared to their range-of-motion and compactness. The findings of chapter four inspire the design of a novel notch-tube mechanism topology referred to as a contact-aided compliant notch-tube joint. The study in chapter five provides a detailed analysis of this contact-aided compliant notch-tube joint and experimental validation of its performance. The results of this study have been published in the American Society of Mechanical Engineers (ASME) Journal of Mechanisms and Robotics [53]. Together, these chapters contribute a detailed analysis of the performance limitations of traditional notch-tube compliant joints. The results demonstrate that only a subset of the design-space will adequately achieve the performance requirements of neuroendoscopic instruments. To expand this design-space, a new design topology that incorporates the concept of contact-aids into notch-tube compliant mechanisms is presented. This work represents the first example of contact-aids being added to tube-shaft based compliant mechanisms. The contact-aid increases the forces that the notched-tube joint can transmit and also helps to increase the joint's compactness. Both of these outcomes better enable notch-tube joint mechanisms to achieve the performance needed for neuroendoscopy.

Chapter six describes the development of a neuroendoscopic instrument that incorporates a notched-tube contact-aided compliant joint. Specifically, this section describes the design of a hand-held instrument with an articulating tube-shaft and handle control. This explanation includes several illustrations depicting the operation of the tool and the fabrication and assembly of its sub-components. Next, the kinematics model from chapter five is extended and used to simulate the reachable workspace of a prototype wristed-forceps. This workspace model is compared to patient-specific data from the study in chapter 3, and the instruments ability to reach the ETV and ETB target sites is assessed. Here, it is found that both target sites can be accessed using the new instrument design with the trocar in a fixed position. This result is not possible using conventional tools which require the surgeon to reposition the trocar during operation. Further, an experimental assessment of the instruments use in a physical brain model is described. The physical simulations of the instruments in the synthetic brain model demonstrate that the surgeon-operator now has the ability to oppose the instruments tip-to-tip. This capability is not feasible using conventional tools, and it significantly contributes to the goal of allowing neuro-endoscopists to dissect in the same manner as conventional microsurgery.

Chapter seven concludes the thesis by discussing the key results, outlining the major obstacles and limitations of the work, and proposing future directions for the project. The end of the chapter synthesizes the main concepts from each of the limitations and obstacles, and proposes future studies that will move the project towards addressing these next-steps.

1.4 References

- [1] A. Grotenhuis, Neuroendoscopic Instruments and Surgical Technique, in *Neuroendoscopy*, 2014, pp. 8191.
- [2] M. R. Gaab, Instrumentation: Endoscopes and equipment, *World Neurosurg.*, vol. 79, no. 2 SUPPL., pp. S14.e11S14.e21, 2013.
- [3] H. J. Marcus, T. P. Cundy, A. Hughes-Hallett, G.-Z. Yang, A. Darzi, and D. Nandi, Endoscopic and keyhole endoscope-assisted neurosurgical approaches: A qualitative survey on technical challenges and technological solutions., *Br. J. Neurosurg.*, vol. 28, no. August 2013, pp. 15, 2014.
- [4] L. Qiao and M. M. Souweidane, Purely endoscopic removal of intraventricular brain tumors: a consensus

- opinion and update., *Mimin. Invasive Neurosurg.*, vol. 54, no. 4, pp. 14954, Aug. 2011.
- [5] E. K. Walsh, W. W. Furniss, and a Schettini, On measurement of brain elastic response in vivo., *Am. J. Physiol.*, vol. 232, no. 1, pp. R2730, 1977.
- [6] K. Miller and K. Chinzei, Constitutive modelling of brain tissue: Experiment and theory, *J. Biomech.*, vol. 30, no. 1112, pp. 11151121, 1997.
- [7] H. J. Marcus, K. Zareinia, L. S. Gan, F. W. Yang, S. Lama, G.-Z. Yang, and G. R. Sutherland, Forces exerted during microneurosurgery: a cadaver study, *Int. J. Med. Robot. Comput. Assist. Surg.*, 2014.
- [8] J. A. Molloy, R. C. Ritter, M. S. Grady, M. A. Howard, E. G. Quate, and G. T. Gillies, Experimental determination of the force required for insertion of a thermoseed into deep brain tissues, *Ann. Biomed. Eng.*, vol. 18, no. 3, pp. 299313, 1990.
- [9] Y. Maddahi, J. Huang, J. Huang, L. S. Gan, K. Zareinia, and G. R. Sutherland, Real - time Measurement of Tool - tissue Interaction Forces in Neurosurgery: Quantification and Analysis, in 2016 IEEE International Conference on Advanced Intelligent Mechatronics (AIM), 2016, pp. 14051410.
- [10] Y. Maddahi, A. Ghasemloonnia, K. Zareinia, N. Sepehri, and G. R. Sutherland, Quantifying force and positional frequency bands in neurosurgical tasks, *J. Robot. Surg.*, vol. 10, no. 2, pp. 97102, 2016.
- [11] J. R. Bekeny, P. J. Swaney, R. J. Webster, P. T. Russell, and K. D. Weaver, Forces Applied at the Skull Base during Transnasal Endoscopic Transsphenoidal Pituitary Tumor Excision, *J. Neurol. Surg. - Part B*, vol. 74, no. 6, pp. 33741, Dec. 2013.
- [12] T. Sugiyama, L. S. Gan, K. Zareinia, S. Lama, and G. R. Sutherland, Tool-Tissue Interaction Forces in Brain Arteriovenous Malformation Surgery, *World Neurosurg.*, vol. 102, pp. 221228, 2017.
- [13] P. F. Morgenstern, N. Osbun, T. H. Schwartz, J. P. Greenfield, A. J. Tsioris, and M. M. Souweidane, Pineal region tumors: An optimal approach for simultaneous endoscopic third ventriculostomy and biopsy, *Neurosurg. Focus*, vol. 30, no. 4, pp. 15, Apr. 2011.
- [14] P. F. Morgenstern and M. M. Souweidane, Pineal region tumors: Simultaneous endoscopic third ventriculostomy and tumor biopsy, *World Neurosurg.*, vol. 79, no. 2, pp. 913, 2013.
- [15] H. Knaus, S. Matthias, A. Koch, and U.-W. Thomale, Single burr hole endoscopic biopsy with third ventriculostomy-measurements and computer-assisted planning, *Childs Nerv. Syst.*, vol. 27, no. 8, pp. 12331241, Aug. 2011.
- [16] X. L. Zhu, R. Gao, G. K. C. Wong, H. T. Wong, R. Y. T. Ng, Y. Yu, and R. K. M. Wong, Single burr hole rigid endoscopic third ventriculostomy and endoscopic tumor biopsy: What is the safe displacement range for the foramen of Monro?, *Asian J. Surg.*, vol. 36, no. 2, pp. 7482, 2013.
- [17] C. S. Karas and E. A. Chiocca, Neurosurgical robotics: a review of brain and spine applications, *J. Robot. Surg.*, vol. 1, no. 1, pp. 3943, Feb. 2007.
- [18] G. Kronreif, W. Ptacek, M. Kornfeld, and M. Frst, Evaluation of robotic assistance in neurosurgical applications, *J. Robot. Surg.*, vol. 6, no. 1, pp. 3339, Nov. 2011.
- [19] a Di Ieva, Microtechnologies in neurosurgery., *Proc. Inst. Mech. Eng. H.*, vol. 224, no. 6, pp. 797800, 2010.
- [20] H. J. Marcus, C. A. Seneci, C. J. Payne, D. Nandi, A. Darzi, and G.-Z. Yang, Robotics in Keyhole Transcranial Endoscope-assisted Microsurgery: A Critical Review of Existing Systems and Proposed Specifications for New Robotic Platforms., *Neurosurgery*, vol. 10, no. 1, pp. 8496, Mar. 2013.
- [21] S. Kobayashi and K. Takakura, System for Minimally Invasive Surgery, vol. 51, no. 4, pp. 985988, 2002.
- [22] H. Takasuna, T. Goto, Y. Kakizawa, T. Miyahara, J. Koyama, Y. Tanaka, T. Kawai, and K. Hongo, Use of a micromanipulator system (NeuRobot) in endoscopic neurosurgery., *J. Clin. Neurosci.*, vol. 19, no. 11, pp. 15537, Nov. 2012.
- [23] A. Morita, S. Sora, M. Mitsuishi, S. Warisawa, K. Suruman, D. Asai, J. Arata, S. Baba, H. Takahashi, R. Mochizuki, and T. Kirino, Microsurgical robotic system for the deep surgical field: Development of a prototype and feasibility studies in animal and cadaveric models, *J. Neurosurg.*, vol. 103, no. 2, pp. 320327, Aug. 2005.
- [24] J. Arata, Y. Tada, H. Kozuka, T. Wada, Y. Saito, N. Ikeda, Y. Hayashi, M. Fujii, Y. Kajita, M. Mizuno, T. Wakabayashi, J. Yoshida, and H. Fujimoto, Neurosurgical robotic system for brain tumor removal., *Int. J. Comput. Assist. Radiol. Surg.*, vol. 6, no. 3, pp. 37585, May 2011.
- [25] M. Zimmermann, R. Krishnan, A. Raabe, and V. Seifert, Robot-assisted navigated endoscopic ventriculostomy: implementation of a new technology and first clinical results., *Acta Neurochir. (Wien)*, vol. 146, no.

7, pp. 697704, 2004.

- [26] B. Kang, V. Castelli, C. Diversi, M. Niccolini, B. M. Ieee, F. Mussa, E. Sinibaldi, and I. Member, Towards Accurate Robot-Assisted Neuroendoscopy using an Ergonomic Handling Interface and a Lightweight Robot, in Engineering in Medicine and Biology Society (EMBC), 2014, pp. 68766879.
- [27] G. R. Sutherland, S. Wolfsberger, S. Lama, and K. Zarei-nia, The evolution of neuroArm., Neurosurgery, vol. 72 Suppl 1, no. January, pp. 2732, Jan. 2013.
- [28] M. Ho, A. McMillan, J. M. Simard, R. Gullapalli, and J. P. Desai, Towards a meso-scale SMA-actuated MRI-compatible neurosurgical robot, IEEE Trans. Robot., vol. 28, no. 1, pp. 213222, Oct. 2011.
- [29] H. J. Marcus, A. Hughes-Hallett, T. P. Cundy, G.-Z. Yang, A. Darzi, and D. Nandi, da Vinci robot-assisted keyhole neurosurgery: a cadaver study on feasibility and safety, Neurosurg. Rev., vol. 38, no. 2, pp. 367371, 2014.
- [30] T. Anor, J. R. Madsen, P. Dupont, R. M. Joseph, and P. Dupont, Algorithms for design of continuum robots using the concentric tubes approach: A neurosurgical example, in 2011 IEEE International Conference on Robotics and Automation (ICRA), 2011, pp. 667673.
- [31] E. J. Butler, R. Hammond-oakley, S. Chawarski, A. H. Gosline, P. Codd, T. Anor, J. R. Madsen, P. E. Dupont, and J. Lock, Robotic neuro-endoscope with concentric tube augmentation, in 2012 IEEE/RSJ International Conference on Intelligent Robots and Systems, 2012, pp. 29412946.
- [32] V. Bodani, H. Azimian, T. Looi, and J. Drake, Design and Evaluation of a Concentric Tube Robot for Minimally- Invasive Endoscopic Paediatric Neurosurgery, in The Hamlyn Symposium on Medical Robotics, 2014, vol. 1, no. 1, pp. 2526.
- [33] J. S. Schneider, J. Burgner, R. J. Webster, and P. T. Russell, Robotic surgery for the sinuses and skull base: what are the possibilities and what are the obstacles?, Curr. Opin. Otolaryngol. Head Neck Surg., vol. 21, no. 1, pp. 116, Feb. 2013.
- [34] J. Burgner, D. C. Rucker, H. B. Gilbert, P. J. Swaney, P. T. Russell, K. D. Weaver, and R. J. Webster, A Telerobotic System for Transnasal Surgery, IEEE/ASME Trans. Mechatronics, vol. 19, no. 3, pp. 9961006, 2014.
- [35] P. E. Dupont, A. Gosline, N. Vasilyev, J. Lock, E. Butler, C. Folk, R. Chen, G. Schmitz, H. Ren, and P. Nido, Concentric Tube Robots for Minimally Invasive Surgery, pp. 24.
- [36] F. Khan, B. Carrillo, T. Looi, and J. M. Drake, A dexterous instrument for minimally invasive neurosurgery, in The Hamlyn Symposium on Medical Robotics, 2013, vol. 1, no. June, pp. 1516.
- [37] T. Kato, I. Okumura, H. Kose, K. Takagi, and N. Hata, Extended Kinematic Mapping of Tendon-Driven Continuum Robot for Neuroendoscopy, no. Iros, pp. 19972002, 2014.
- [38] T. Kato, I. Okumura, H. Kose, K. Takagi, and N. Hata, Tendon-driven continuum robot for neuroendoscopy: validation of extended kinematic mapping for hysteresis operation, Int. J. Comput. Assist. Radiol. Surg., vol. 11, no. 4, pp. 589602, 2016.
- [39] M. Mitsuishi, P. Bartolo, Y. Kanada, T. Yoneyama, T. Watanabe, H. Kagawa, N. Sugiyama, K. Tanaka, and T. Hanyu, Force feedback manipulating system for neurosurgery, First CIRP Conf. BioManufacturing, vol. 5, no. 1, pp. 133136, 2013.
- [40] F. Dewaele, a. F. Kalmar, F. De Ryck, N. Lumen, L. Williams, E. Baert, H. Vereecke, J. P. Kalala Okito, C. Mabilde, B. Blanckaert, V. Keereman, L. Leybaert, Y. Van Nieuwenhove, J. Caemaert, and D. Van Roost, A Novel Design for Steerable Instruments Based on Laser-Cut Nitinol, Surg. Innov., vol. 21, no. 3, pp. 303311, 2014.
- [41] P. A. York, P. J. Swaney, H. B. Gilbert, and R. J. Webster III, A Wrist for Needle-Sized Surgical Robots, in IEEE International Conference on Robotics and Automation, 2015, pp. 17761781.
- [42] P. J. Swaney, P. A. York, H. B. Gilbert, J. Burgner-Kahrs, and R. J. Webster III, Design, Fabrication, and Testing of a Needle-sized Wrist for Surgical Instruments, ASME J. Med. Devices, no. c, 2016.
- [43] J. A. Bell, C. E. Saikus, K. Ratnayaka, V. Wu, M. Sonmez, A. Z. Faranesh, J. H. Colyer, R. J. Lederman, and O. Kocaturk, A Deflectable Guiding Catheter for Real-Time MRI-Guided Interventions, J. Magn. Reson. Imaging, vol. 35, no. 4, pp. 908915, 2012.
- [44] H. Fischer, B. Vogel, W. Pfleging, and H. Besser, Flexible distal tip made of nitinol (NiTi) for a steerable endoscopic camera system, Mater. Sci. Eng. A, vol. 273275, pp. 780783, 1999.
- [45] Y. Haga, Y. Muyari, S. Goto, T. Matsunaga, and M. Esashi, Development of Minimally Invasive Medical Tools Using Laser Processing on Cylindrical Substrates, Electr. Eng. Japan, vol. 176, no. 1, pp. 6574, 2011.

- [46] J. Peirs, H. Van Brussel, D. Reynaerts, and G. De Gersem, A Flexible Distal Tip with Two Degrees of Freedom for Enhanced Dexterity in Endoscopic Robot Surgery, in The 13th Micromechanics Europe Workshop, 2002, pp. 271274.
- [47] S. C. Ryu, P. Renaud, R. J. Black, B. L. Daniel, and M. R. Cutkosky, Feasibility Study of an Optically Actuated MR-compatible Active Needle, in IEEE International Conference on Intelligent Robots and Systems, 2011, pp. 25642569.
- [48] A. Gao, R. Murphy, H. Liu, I. Iordachita, and M. Armand, Mechanical Model of Dexterous Continuum Manipulators with Compliant Joints and Tendon/External Force Interactions, IEEE/ASME Trans. Mechatronics, 2016.
- [49] M. D. M. Kutzer, S. M. Segreti, C. Y. Brown, R. H. Taylor, S. C. Mears, and M. Armand, Design of a New Cable-Driven Manipulator with a Large Open Lumen: Preliminary Applications in the Minimally-Invasive Removal of Osteolysis, in IEEE International Conference on Robotics and Automation, 2011, pp. 29132920.
- [50] Eastwood KW, Looi T, Naguib HE, Drake JM. Design optimization of neuroendoscopic continuum instruments for third ventriculostomy and tumor biopsy. Proceedings of the 37th Annual International Conference of the IEEE Engineering in Medicine and Biology Society (EMBC), 2015, pp. 4853-4856.
- [51] Eastwood KW, Azimian H, Carrillo B, Looi T, Naguib HE and Drake JM . Kinetostatic design of asymmetric notch joints for surgical robots. Proceedings of the 2016 IEEE/RSJ International Conference on Intelligent Robots and Systems (IROS), 2016, pp. 2381-2387.
- [52] Eastwood KW, Bodani VP and Drake JM. Three-Dimensional Simulation of Collision-Free Paths for Combined Endoscopic Third Ventriculostomy and Pineal Region Tumor Biopsy: Implications for the Design Specifications of Future Flexible Endoscopic Instruments. Operative Neurosurgery, 2016, 12(3), 231-238.
- [53] K. W. Eastwood, P. Francis, H. Azimian, A. Swarup, T. Looi, J. M. Drake, and H. E. Naguib, Design of a Contact-Aided Compliant Notched- Tube Joint for Surgical Manipulation in Confined Workspaces, J. Mech. Des., vol. Accepted, 2017.

Chapter 2

Design Optimization of Neuroendoscopic Continuum Instruments for Third Ventriculostomy and Tumor Biopsy

2.1 Abstract

A simulation-based approach to the design of procedure-specific dexterous neuroendoscopic continuum instruments for endoscopic third ventriculostomy and tumor biopsy is proposed. Given pre-operative CT and MRI images, the algorithm returns instrument design specifications including lengths, curvatures and alternative positions for the surgical incision while respecting anatomical boundaries. This methodology proposes a novel clinically-guided geometric representation of surgical targets specific to this indication. The additional constraints imposed by the presence of surgical trocars and endoscopes are also considered. Finally, we conclude with a clinical example to demonstrate the proposed approach.

2.2 Introduction

Within the field of minimally invasive neurosurgery, the array of procedures that can be performed with standard neuroendoscopes is limited. There is a defined need for novel instruments with increased dexterity to advance the scope of intraventricular endoscopic surgery, particularly for pathologies of the third ventricle [1]. Recent advancements within the field of continuum robotics have offered a robust solution to this problem through the development of teleoperated concentric-tube robotic surgical platforms, and other continuum robotic and manually operated dexterous instruments [2][9].

The expansion of continuum based tools necessitates the development of customized design strategies. Since the attainable motions of these devices are non-intuitive, we propose a framework for determining the geometric design specifications for a generic continuum based dexterous neuroendoscopic instrument. The aim of this work is to develop a method for determining the optimal instrument configuration for performing a single incision endoscopic third ventriculostomy (ETV) and pineal region endoscopic tumor

biopsy (ETB). Further, these design specifications should be applicable to developing either manual or robotic tools.

A combined ETV/ETB procedure is indicated for patients presenting with obstructive hydrocephalus secondary to an intra- or para-ventricular tumor. This condition represents a swelling of the cerebral ventricles, which are naturally occurring spaces within the brain filled with cerebrospinal fluid (CSF). For the cases considered within this study, the swelling occurs because a pineal region tumor occludes the cerebral aqueduct, preventing the normal circulation of CSF. The ETV/ETB surgery is performed through a burr hole (surgical incision) in the frontal bone of the skull, providing the tools access to move within the ventricles.

2.3 Prior Work

Many prior studies regarding design optimization strategies for continuum based minimally invasive instruments have focused on concentric-tube robots for cardiovascular, thoracic and neurosurgical applications [3], [10], [11]. The optimization approaches have been developed from geometric models into specific kinematic and mechanics-based algorithms particular to concentric-tube robots, and have recently been incorporated into follow-the-leader pathplanning algorithms [3], [5], [10], [11]. These approaches have implemented cost functions or gradient field approaches to determine the shape of an active cannula navigating from some assumed initial configuration [starting point, orientation] to a series of surgical targets represented by points [spheres with radial tolerance δ] . The optimization goals are to minimize the number of segments of the robot, and minimize the segment lengths and curvatures while respecting virtual anatomical boundaries generated from patients preoperative images.

This work provides the following contributions beyond the design optimizations presented previously: In section III-B an alternative geometric representation of the surgical targets used to constrain the design, customized for ETV/ETB, is presented. Further, section IV-C outlines a framework for including the burr hole and base frame orientation as optimization variables. Small changes in burr hole position can impact the geometry and ultimately the stiffness of the final instrument design. This result is significant considering the small size scales and tight outer-diameter, tip force and range of motion requirements encountered in neurosurgery. Finally, the numerical simulation of section V considers the impact that standard surgical equipment, such as rigid endoscopes and surgical trocars, have on constraining the instrument segments.

2.4 Geometric Modelling

2.4.1 Anatomical Model

Anatomical models of the skull, cerebral ventricles and pineal region tumor were obtained by magnetic resonance imaging (MRI). Through the application of threshold segmentation, STL models of these structures were imported into a MATLAB (Mathworks, Massachusetts) work environment for analysis. The anatomical data was utilized to denote instrument workspace boundaries A , which are assumed to be closed and nonintersecting surfaces. We have assumed that all instruments must strictly respect the boundaries of A and avoid contact with the delicate walls of the ventricles. For implementation purposes, a KD-tree nearest-neighbor method was utilized to efficiently determine instrument collisions

with anatomical boundary data.

2.4.2 Instrument Kinematic Model

For the purpose of this investigation, we define the design of a generic dexterous continuum neuroendoscopic instrument as a set of geometric parameters specific to a surgical task. For each design d of an n -segment instrument there exists a vector of $3n$ real value design parameters which include segment length L_i , segment curvature k_i , and segment orientation θ_i . In this manner, the instrument midline can be defined as a piecewise constant curvature space-curve on the intervals $s \in [0, L_i]$ using the convention of Frenet-Serret. The instrument body can further be represented as a piece-wise cylindrical manifold of radius R_i centered at the space-curve parameterized by s . This design space $D \subset \mathbb{R}^{3n}$ is a bounded set. The design space is defined in this simplified manner to generalize the proposed approach to be applicable to most continuum instruments. This notation has been adopted from [3], [10].

The number of segments are assumed to be known a priori, and designs with nonconstant curvatures are not considered. Workspace goal regions, or surgical target sites, are denoted as a set S of size m , $S = S_1, S_2, \dots, S_m$. These surgical targets are assumed to be represented as cylinders with radius r_j and center point c_j , denoting an acceptable planar region through which the surgical indication can be performed. Further, the cylindrical height δ_j represents a small tolerance offset normal to the target surface. S_j are defined for some design d_j , where acceptable designs correspond to the instrument end-effector occupying a space within S_j while respecting anatomical boundaries A . Fig. 2.1 is a schematic summarizing all notation.

The choice of defining the surgical target sites as cylinders loosens the constraints on optimizing the trajectory by allowing for a larger acceptable surface through which to perform the perforation of the floor of the third ventricle or the biopsy of the tumor. In the scenario of ETV/ETB, the tolerance on tip positioning in the in-plane directions is not as significant as the normal to plane tolerance (penetration depth) because of delicate structures deep to the walls of the ventricles. The cylindrical bound was chosen in-lieu of the standard spherical target (target point with radial tolerance δ) to reflect these clinical conditions. The boundaries of these target regions were defined using surgeon selected points taken from patient preoperative imaging.

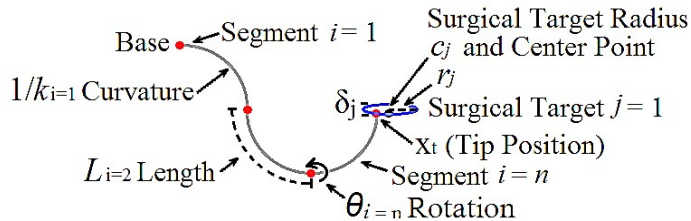


Figure 2.1: Notation used for space curve representing midline of design d_j

2.5 Problem Definition

For the purposes of designing dexterous manual instruments, the number of controlled degrees of freedom must be minimal, and thus independently adjusting instrument tip orientation is assumed to be beyond the scope of this analysis. With regards to surgical robotics design, it is standard convention to

decompose the design problem into instrument body navigation and end-effector manipulation. Since the goal of this work is to produce design specifications generalizable to both manual and robotic continuum instruments, we limit our optimization to the problem of instrument positioning.

The goal of the optimization is to minimize the curvature and length of the segments subject to the following constraints:

- The end-effector of the instrument of design d_j must lie within the surgical boundary S_j .
- Instruments must respect anatomical boundary A .
- The length L_i and segment curvature k_i must be *approximately equal for all $d_{1\dots m}$ initiating from the same surgical incision.

The physical rationale for the optimization objectives and constraints are as follows: The segment lengths are minimized to maximize the effective stiffness of the overall instrument structure since continuum instruments are commonly modelled as cantilever beams. The segment curvatures are minimized to conform to material constraints. As most continuum instruments are constructed in such a way that the instrument body acts as both links and flexural joints, there is an upper limit on the maximum elastic strain that the structure can undergo. Minimizing curvature will aid in abiding these strain limits. Finally, the **soft* constraint allows us to find the intersection of the instrument designs d_j , for all m , such that a single geometry (lengths, curvatures) can reach all targets.

As discussed, the surgical target sites are represented as planar circular regions with some small adjustable thickness tolerance δ . In addition to better representing actual clinical conditions, this convention loosens the optimization constraints and allows for more physically realizable tool configurations to be considered. Another component of the proposed optimization methodology is to consider the surgical incision and orientation as variables. This additional layer to the problem initiated from a clinical motivation in determining the shortest distance to both surgical targets through relocation of the burr hole. Adding this component to the problem has the additional benefit of aiding in convergence to a single solution capable of reaching all surgical targets. Design candidates d_j initiating from the same surgical incision are referred to as a family and this set is denoted Γ_p , for some p^{th} surgical incision.

2.5.1 Method Inputs

The proposed methodology requires three user inputs in addition to the anatomical constraint data: The surgical target sites S_j , and an initial estimate of the surgical incision and instrument base orientation. The surgical incision can be inferred from the burr hole visible on the patients STL data or by the convention of using Kochers point (25 mm lateral to the sagittal suture, 10 mm anterior to the coronal suture). For the case of ETV-ETB, the instrument base orientation is assumed to be represented by a vector from the center of the surgical incision to the center of the foramen of Monro. The foramen of Monro is a narrowed region of the cerebral ventricles through which the instruments must pass to perform an ETV-ETB procedure. The boundaries of this structure and the burr hole can be delineated using the same geometric approximation as the surgical target sites S_j . A GUI (Fig. 2.2) was developed in MATLAB to measure and place the initial surgical incision estimate. Standard measurements can be taken with respect to the skulls surface landmarks, the cranial suture lines, along the convexity of its surface. A mark-up tool, which uses a piece-wise linear Euclidean distance approximation along the surface of the skull, was coded in MATLAB to estimate burr hole placement.

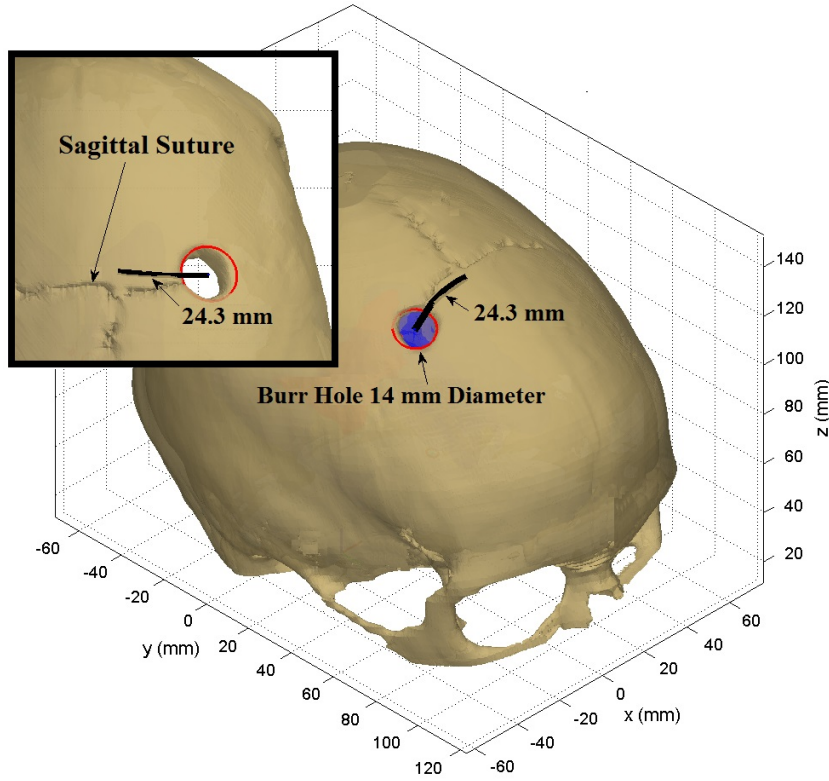


Figure 2.2: Using a mark-up tool written for the GUI, the initial burr holes position is measured along the curved surface of the skull with respect to the cranial sutures. The diameter is approximated by a superimposed circular boundary by selecting three points along the cut edge.

2.5.2 Penalty Functions

The tip position error can be defined using functions f_1 and f_2 which are taken in the local coordinate frame of the surgical target of interest S_j , respectively as:

$$f_1 = (x_t \cdot \bar{n}_j)^2 - \delta_j^2 \quad (2.1)$$

$$f_2 = x_t x_t^T - (x_t \cdot \bar{n}_j)^2 / r_j^2 \quad (2.2)$$

where x_t corresponds to the position of the tip of the final segment of the instrument expressed in a frame centered at c_j and aligned with the normal of the plane n_j containing the circular boundary r_j of S_j . Accordingly, the tip position penalty function becomes:

$$f_3 = \begin{cases} \alpha_1 \cdot f_1 & \text{if } 0 \leq f_2 \leq 1 \\ \alpha_1 \cdot f_1 + \alpha_2 \cdot f_2 & \text{if } f_2 > 1 \end{cases} \quad (2.3)$$

Here, the use of α denotes weighting factors applied to the functions. For the constraint that the instruments must respect the anatomical boundaries, a penalty function f_5 can be defined as follows:

$$f_4 = [x_i(S) - x_A(x_i(S))]^2 / R_i^2 \quad (2.4)$$

$$f_5 = \begin{cases} 0 & \text{if } f_4 > 1 \\ \alpha_3 \cdot f_4 & \text{if } f_4 < 1 \end{cases} \quad (2.5)$$

Function f_5 assumes that the instrument base initiates inside the boundary A . This method is defined for all centerline positions $x_i(s)$ for the i^{th} segment of the j^{th} design initiating from the p^{th} burr hole under consideration. The function x_A computes the nearest neighbor of the instrument point $x_i(s)$ of A . Normalizing to R_i accounts for the physical geometry of the segment under consideration.

Finally, penalty functions f_6 and f_7 can be implemented to impose the soft constraint that a set of designs d_j containing m different constituent configurations within some design family Γ_p will converge to the same set.

$$f_6 = \alpha_4 \cdot \sum_{i=1}^n \sum_{j=1}^m \sum_{g=1}^m (k_{i,j} - k_{i,g})^2 \quad (2.6)$$

$$f_7 = \alpha_5 \cdot \sum_{i=1}^n \sum_{j=1}^m \sum_{g=1}^m (L_{i,j} - L_{i,g})^2 \quad (2.7)$$

where, as stated, the subscript i corresponds to a given segment within a design configuration for a particular surgical target denoted by j . The subscripts j and g both represent the surgical target of interest and are implemented in (6) and (7) for all combinations of g and j , for all m .

2.5.3 Optimizing Surgical Incision and Orientation

With the inputs specified according to section IV-A, subsequent design iterations can relocate the burr hole position by applying incremental rotations to the base frame of a distal segment and subsequently re-computing for proximal segments. In this manner, we consider families Γ_p of designs to reach each S_j . For constant curvature space curves, a starting point, ending point and a starting or ending direction vector is sufficient to fully define a segment.

Section V-A will outline our rationale and implementation of this approach using a curved segment initiating in the neighborhood of the foramen of Monro to select alternative, clinically appropriate burr hole locations on the frontal bone.

2.5.4 Algorithm

The penalty functions can be posed as sets of nested optimization problems.

Algorithm

1. Set a minimal number of sections (n) to use in the optimization, specify surgical targets S_j and the initial burr hole location and orientation.
2. Compute: $d_j = \arg \min (f_3 + f_5)$
3. Store Γ_p and compute: $(f_6 + f_7)$
4. If $(f_6 + f_7) >$ specified tolerance

Generate new burr hole location and go to 2

Else stop

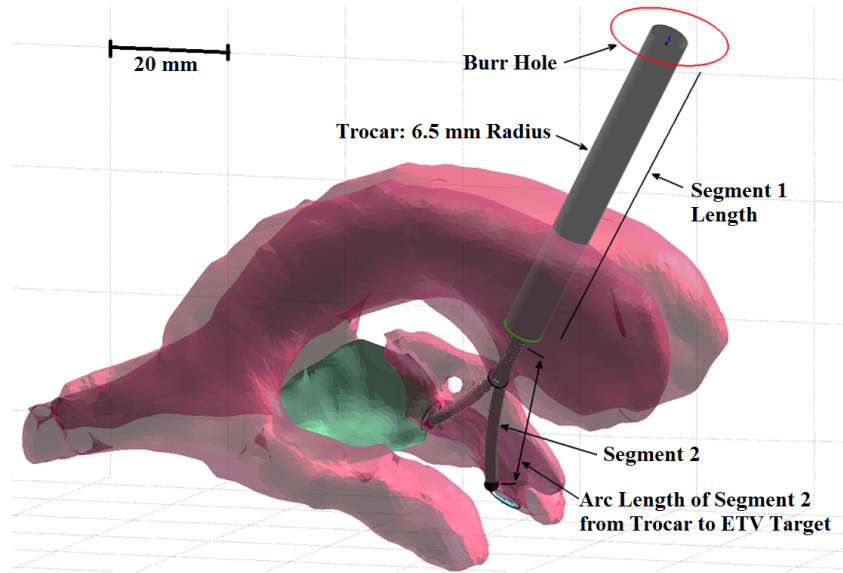


Figure 2.3: Optimal Instrument Configuration Superimposed on ventricles

2.6 Numerical Example

Here, we present a straight-forward clinical example of the proposed framework. Initially, the instrument shaft was assumed to enter the superior-lateral aspect of the frontal horn of the right lateral ventricle and follow a non-linear space curve, through the foramen of Monro, to each surgical target. Based on tool prototypes tested on physical phantom models of this procedure, two segments ($n = 2$) have been sufficient for surgical navigation to the two target sites ($m = 2$) [4]. Early simulations of these conditions yielded instrument designs within feasible material design limits. However, for practical purposes, the instruments must be paired with an endoscope to visualize the targets. Although flexible endoscopes can be utilized for ETV-ETB, many surgeons favor rigid endoscopes for improved image quality [12][16]. Further, in order to adequately view the workspace, the tip of the endoscope must extend just proximal to the foramen of Monro, and thus this work-flow constrains the proximal segment of the instrument to be straight.

Standard neuroendoscopic instruments have radii (R_i) on the order of 0.5-1 mm. In such cases, segment curvatures sharper than $1/40 \text{ mm}^{-1}$ are considered to be outside of the elastic range for concentric tube devices. Since simulations utilizing a single straight segment and two curved segments distal to the trocar elicited final curvatures higher than $1/40 \text{ mm}^{-1}$ [$1/10$ to $1/20 \text{ mm}^{-1}$], a simple single curved, single straight segment design was selected. Fig. 2.3 depicts a MATLAB graphic illustrating the final result of the algorithm.

To reduce the overall length of the instrument, elementary rotations were applied to the base frame of the second segment. These adjustments modified the initial trajectory of the surgical trocar (Table I). To constrain these adjustment to clinically acceptable bounds, the rotations were kept small, and the intersection point between segment one and the skull was enforced to be anterior and lateral to the initial incision. Table II summarizes the design outcomes of the simulation.

From the results, we see a reduction in overall instrument length by 8-10%, while the sharpest radius of curvature to reach both sites is unaffected (40 mm). Since the stiffness of a cantilever beam is inversely

Table 2.1: Burr Hole Positions Relative to Skull Landmarks

Experimental Results	Distance from landmark (mm)	
	Coronal Suture	Sagittal Suture
Surgical Burr hole (reference, a.)	3.24	24.3
Optimal Burr hole (computed, b.)	9.66	25.9

Table 2.2: Section Radii of Curvature and Lengths

Surgical Target Site (S_j)	Experimental Results (mm)			
	$1/k_1$	$1/k_2$	L_1	L_2
Tumor Biopsy ^a .	-	59.2	69.9	27.3
3 rd Ventriculostomy ^a .	-	41.2	69.9	29.7
Tumor Biopsy ^b .	-	40.4	61.3	26.1
3 rd Ventriculostomy ^b .	-	41.8	61.3	30.3

proportional to its length cubed, tip stiffness will increase by a factor of 1.3-1.4 which is significant for the small scales in neurosurgery.

2.7 Conclusion

We have proposed a framework to design continuum based dexterous instruments for ETV/ETB. Future work will include implementing this approach to study a larger sample of patients and to draw more general conclusions about the geometric specifications for this procedure specific design.

2.8 References

- [1] S. M. Barber, L. Rangel-Castilla, and D. Baskin, Neuroendoscopic resection of intraventricular tumors: A systematic outcomes analysis., *Minim. Invasive Surg.*, vol. 1, no. 1, pp. 112, Jan. 2013.
- [2] E. J. Butler, R. Hammond-Oakley, S. Chawarski, A. H. Gosline, P. Codd, T. Anor, J. R. Madsen, P. E. Dupont, and J. Lock, Robotic neuro-endoscope with concentric tube augmentation, in *Intelligent Robots and Systems (IROS)*, 2012, pp. 29412946.
- [3] T. Anor, J. R. Madsen, P. Dupont, R. M. Joseph, and P. Dupont, Algorithms for design of continuum robots using the concentric tubes approach: A neurosurgical example, in *2011 IEEE International Conference on Robotics and Automation (ICRA)*, 2011, pp. 667673.
- [4] V. Bodani, H. Azimian, T. Looi, and J. Drake, Design and Evaluation of a Concentric Tube Robot for Minimally- Invasive Endoscopic Paediatric Neurosurgery, in *The Hamlyn Symposium on Medical Robotics*, 2014, vol. 1, no. 1, pp. 2526.
- [5] C. Bergeles, A. H. Gosline, N. V. Vasilyev, P. J. Codd, P. J. del Nido, and P. E. Dupont, Concentric tube robot design and optimization based on task and anatomical constraints, *IEEE Trans. Robot.*, vol. 31, no. 1, pp. 6784, 2015.
- [6] F. Khan, B. Carrillo, T. Looi, and J. M. Drake, A dexterous instrument for minimally invasive neurosurgery, in *The Hamlyn Symposium on Medical Robotics*, 2013, vol. 1, no. June, pp. 1516.
- [7] A. Morita, S. Sora, M. Mitsuishi, S. Warisawa, K. Suruman, D. Asai, J. Arata, S. Baba, H. Takahashi, R. Mochizuki, and T. Kirino, Microsurgical robotic system for the deep surgical field: Development of a prototype and feasibility studies in animal and cadaveric models, *J. Neurosurg.*, vol. 103, pp. 320327, Aug. 2005.
- [8] M. Mitsuishi, P. Bartolo, Y. Kanada, T. Yoneyama, T. Watanabe, H. Kagawa, N. Sugiyama, K. Tanaka, and T. Hanyu, Force feedback manipulating system for neurosurgery, *First CIRP Conf. BioManufacturing*, vol. 5, no. 1, pp. 133136, 2013.

- [9] M. Ho, A. McMillan, J. M. Simard, R. Gullapalli, and J. P. Desai, Towards a meso-scale SMA-actuated MRI-compatible neurosurgical robot, *IEEE Trans. Robot.*, vol. 28, no. 1, pp. 213222, Oct. 2011.
- [10] L. a. Lyons, R. J. Webster, and R. Alterovitz, Planning active cannula configurations through tubular anatomy, in *IEEE International Conference on Robotics and Automation (ICRA)*, 2010, pp. 20822087.
- [11] C. Bedell, J. Lock, A. Gosline, and P. E. Dupont, Design optimization of concentric tube robots based on task and anatomical constraints, in *IEEE International Conference on Robotics and Automation (ICRA)*, 2011, pp. 398403.
- [12] S. Chibbaro, F. Di Rocco, O. Makiese, A. Reiss, P. Poczos, G. Mirone, and F. Servadei, Neuroendoscopic management of posterior third ventricle and pineal region tumors: Technique, limitation, and possible complication avoidance, *Neurosurg Rev*, vol. 35, no. 3, pp. 331340, 2012.
- [13] X. Lun, R. Gao, G. Kwok, C. Wong, H. Tung, R. Yuen, T. Ng, Y. Yu, R. Kit, M. Wong, and W. Sang, Single burr hole rigid endoscopic third ventriculostomy and endoscopic tumor biopsy: What is the safe displacement range for the foramen of Monro?, *Asian J. Surg.*, vol. 36, no. 2, pp. 7482, 2013.
- [14] P. F. Morgenstern and M. M. Souweidane, Pineal region tumors: Simultaneous endoscopic third ventriculostomy and tumor biopsy, *WNEU*, vol. 79, no. 2, pp. 913, 2013.
- [15] P. F. Morgenstern, N. Osbun, T. H. Schwartz, J. P. Greenfield, A. J. Tsioris, and M. M. Souweidane, Pineal region tumors: An optimal approach for simultaneous endoscopic third ventriculostomy and biopsy, *Neurosurg. Focus*, vol. 30, no. 4, pp. 15, Apr. 2011.
- [16] H. Knaus, S. Matthias, A. Koch, and U.-W. Thomale, Single burr hole endoscopic biopsy with third ventriculostomy-measurements and computer-assisted planning, *Childs Nerv. Syst.*, vol. 27, no. 8, pp. 12331241, Aug. 2011.

Chapter 3

Three-Dimensional Simulation of Collision-Free Paths for Combined Endoscopic Third Ventriculostomy and Pineal Region Tumor Biopsy: Implications for the Design Specifications of Future Flexible Endoscopic Instruments

3.1 Abstract

Background

Recent innovations to expand the scope of intraventricular neuroendoscopy have focused on transitioning multiple-incision procedures into singlecorridor approaches. However, the successful adoption of these combined procedures requires minimizing the unwanted torques applied to surrounding healthy structures.

Objective

To define the geometry of relevant anatomical structures in endoscopic third ventriculostomy (ETV) and pineal region tumor biopsy (ETB). Second, to determine the optimal instrument shaft path required for collision-free single burr hole combined ETV-ETB.

Methods

Magnetic resonance and computed tomography data from 15 pediatric patients who underwent both ETV and ETB procedures between 2006 and 2014 was segmented by using the 3DSlicer software package to create virtual 3-D patient models. Anatomical regions of interest were measured including the foramen of Monro, the massa intermedia, the floor of the third ventricle, and the tumor margin. Utilizing the MATLAB software package, virtual dexterous instruments were inserted into the models and optimal dimensions were calculated.

Results

The diameters of the foramen of Monro, massa intermedia (anterior-posterior, superior-inferior), anterior third ventricle, and tumor margin are 6.85, 4.01, 5.05, 14.2, and 28.5 mm, respectively. The average optimal burr placement was determined to be 22.5 mm anterior to the coronal and 30 mm lateral to the sagittal sutures. Optimal flexible instrument geometries for novel instruments were calculated.

Conclusion

We have established a platform for estimating the shape of novel curved dexterous instruments for collision-free targeting of multiple intraventricular points, which is both patient and tool specific and can be integrated with image guidance. These data will aid in developing novel dexterous instruments.

3.2 Introduction

Endoscopic third ventriculostomy (ETV) has become a standard approach for managing patients with noncommunicating hydrocephalus. A subset of this patient population includes individuals with tumors of the pineal region. In such cases, an endoscopic tumor biopsy (ETB) is performed accompanying an ETV to establish a histological diagnosis and inform further therapy.

Anatomical obstacles and the physical separation of the ETV and ETB targets are the source of much discussion regarding the optimal approach to this combined ETV-ETB procedure; namely, the choice of utilizing multiple incisions to target and perform each subprocedure separately, or performing both maneuvers through a single corridor. Under the appropriate circumstances, consensus has advocated for the latter.

However, much debate still remains surrounding the optimal technique and instrumentation [1-7]. Flexible endoscopes offer increased intraventricular dexterity and the ability to follow a nonlinear, curved tool path. However, these devices often have reduced image quality, smaller working channels, and, therefore, reduced biopsy sample size. Anecdotally, flexible endoscopes have been described as requiring increased experience and training to use effectively. Rigid endoscopes are preferred for combined ETV-ETB procedures by many neurosurgeons[1-4],[7]. However, these tools have the major drawback of requiring a direct line-of-site between the entry point and the surgical targets. Further, the use of rigid tools through a single corridor often requires torques to be applied to healthy structures to reach multiple intraventricular targets [8].

An optimal approach to this combined procedure minimizes the tissue shift applied to the foramen of Monro (FM) while ensuring adequate visualization and access to both surgical targets from a single burr hole [1-2],[4]. To fully realize the benefits of improved visualization from rigid endoscopes, while achieving

true collision-free instrument trajectories, dexterous curved instruments with increased distal ranges of motion must be developed. Such instrument designs have been successfully adopted in laparoscopy to reduce tool collisions and provide triangulation. Considering either current flexible or rigid standard neuroendoscopes, the instruments are aligned nearly coaxially distal to the endoscope tip, increasing the potential for collisions and limiting independent range of motion [9]. The development of dexterous instruments capable of extending distal to the operating sheath with the ability for triangulation, used in conjunction with angled lens endoscopes, may provide a solution.

The first objective of this study is to determine the average optimal burr-hole position for performing a combined ETV-ETB procedure by means of finding an equal instrument trajectory to both surgical targets. These results will be compared with previous recommendations for surgical planning by using standard, straight neuroendoscopic instruments [3-4].

The second objective of this study is to facilitate the innovation of novel neuroendoscopic instruments capable of collision-free manipulation specific to ETV-ETB. In so doing, we aim to describe the surgical work-space volume through the measurement of relevant anatomical structures encountered in ETV-ETB compared with previous literature [3]. Furthermore, we aim to specify design dimensions for novel curved-shaft instruments capable of collision-free ETV-ETB. Both the anatomical measurements and the instrument shape specifications will address a defined gap in knowledge for developing new surgical-planning approaches and future instrument development.

3.3 Methods

3.3.1 Patient Selection

A review of cases between 2006 and 2014 was completed, and 27 patients presenting with pineal region tumors at the Hospital for Sick Children in Toronto, Canada were identified. Of the 27 patients, 4 were excluded because of inadequate computed tomography (CT) data. Five patients were excluded because of inadequate magnetic resonance (MR) data, and 3 patients were excluded because they were not considered to receive ETV as a result of ventricular or tumor size. Fifteen patients (9 male and 6 female) who underwent successful or attempted simultaneous ETV and ETB procedures were included in this study (Table 1). The mean age was 9 years (range, 6 days to 17 years). The use of patient information was approved for this study by the Ethics Review Committee of The Hospital for Sick Children.

3.3.2 Imaging

MR and CT imaging studies were performed using the parameters summarized in Table 2 and Table 3, respectively.

3.3.3 Anatomical Measurements and Analysis

Individual patients postoperative CT and preoperative MRI data were imported into the 3DSlicer software package (<http://www.slicer.org>), a Digital Imaging and Communications in Medicine (DICOM) editing and simulation software [10-11]. Standard thresholding functions, such as the *Simple Region Growing Segmentation* and the *Editor* modules, were implemented to segment the patients skull and to

Table 3.1: Summary of Patient Demographic Data^a.

No.	Age	Sex	Diagnosis	Date(yyyy/mm)	Procedure
1	16 y	M	Germinoma	2005/05	ETV, ETB with EVD
2	3 y 5 mo	M	Pineoblastoma	2006/07	ETV, ETB with EVD
3	19 mo	M	Parapineal Cyst	2006/08	ETV, ETB with EVD
4	9 y 11 mo	M	Mature Teratoma of Pineal Cyst	2006/10	ETV, ETB
5	19 mo	F	Pilocytic Astrocytoma Pineal Region	2008/01	ETV, ETB
6	11 y 9 mo	F	Low-grade Neoplasm	2008/01	ETV, ETB with EVD
7	16 y	M	Germinoma	2008/02	ETV, ETB
8	17 y	F	Pineoblastoma	2008/07	ETV, ETB with EVD
9	3 y 3 mo	F	Pineoblastoma WHO IV	2009/01	ETV, ETB with EVD
10	12 y 7 mo	F	Pineoblastoma	2010/08	ETV, ETB
11	3 y 1 mo	M	Pineoblastoma WHO IV	2010/10	ETV, ETB (aborted) ^b
12	11 y 7 mo	M	Pineoblastoma WHO IV	2012/03	ETV, ETB
13	12 y	M	Germinoma	2012/07	ETV, ETB with EVD
14	15 y	F	Astrocytoma WHO III	2013/11	ETV, ETB with EVD
15	6 d	M	Rhabdoid Tumor WHO IV	2014/10	ETV, ETB with EVD

^a. ETB, endoscopic tumor biopsy; ETV, endoscopic third ventriculostomy; EVD, external ventricular drain; WHO, World Health Organization.

^b. Both ETV and ETB were attempted and navigation to the surgical sites was successful. Anatomical concerns necessitated that the biopsy was converted to a craniotomy and an EVD inserted in lieu of ETV.

Table 3.2: Summary of MR Imaging Data^a.

MR System	Patients	Image Modality	Parameters
1.5-T Genesis Signa (General Electric)	5	T1 SPGR	TR 9 ms, TE 4.2 ms, matrix 128 x 128, and 2-mm slice thickness
1.5-T Achieva (Philips)	7	T1 SPGR	TR 6.8 ms, TE 3.15 ms, matrix 128 x 128, and 2-mm slice thickness
3.0-T Achieva imaging systems (Philips)	3	T1-TFE GR	TR 6.0 ms, TE 2.72, matrix 128 x 128 and 0.9-mm slice thickness

^a. GR, gradient rephrasing; SPGR, spoiled gradient echo; TE, echo time; TFE, turbo field echo; TR, repetition time.

delineate the ventricles and tumor. The models were converted to Standard Template Library (STL) files, a standard file format for 3-dimensional (3-D) simulations. The imaging modalities were registered using the standard *Rigid Registration* module to appropriately align all 3-D model data. The sagittal and coronal skull suture lines and a line formed between the Nasion and the Inion were used to align the data with standard anatomical reference frames.

Anatomical measurements were completed independently by 2 neurosurgeons using the 3DSlicer *Measurements and Markups* module. The anatomical structures assessed include the diameters of the *FM*, the massa intermedia (*MI*) in the anterior-posterior and superior-inferior directions, the anterior third ventricle width, the distance between the tumor and the midbrain, the distance between the anterior aspect of the tumor and the *MI*, and the maximum tumor diameters. Additionally, 3DSlicer was used to denote planar circular regions representing the *FM*, the floor of the third ventricle, and a suitable target region for biopsy of the tumor that were used for surgical planning.

The patient STL models were subsequently imported into the MATLAB software package and displayed in a 3-D virtual environment (Fig. 3.1). For the purposes of our investigation, determining the location of the burr hole for each patients actual surgery and the ability to overlay virtual instruments

Table 3.3: Summary of CT Imaging Data

CT System	Patients	Parameters: Slice Thickness, Exposure Time
Light speed ultra (General Electric)	8	5 mm, 4000 ms
GeminiGXL 16 (Philips)	6	3 mm, 1500 ms
Discovery CT750HD (General Electric)	1	5 mm, 2000 ms

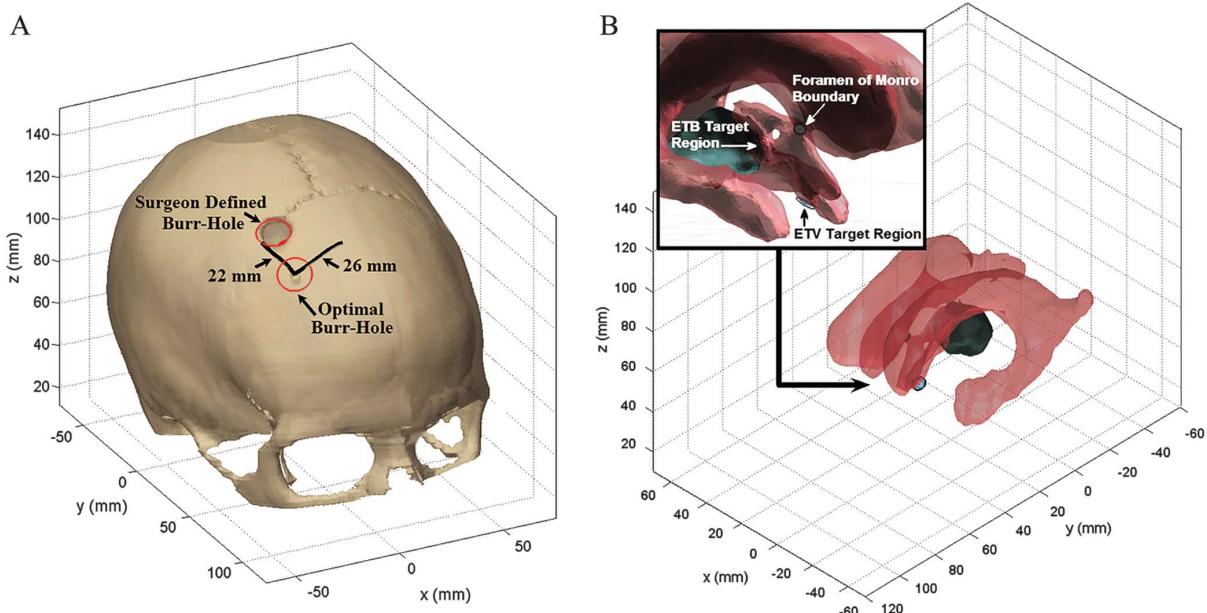


Figure 3.1: Patient models as seen in MATLAB. A, image depicts the measurement tool utilized to locate the burr-hole incisions. B, image depicts the circular target regions denoting the FM and sites for ETB and ETV. ETB, endoscopic tumor biopsy; ETV, endoscopic third ventriculostomy; FM, foramen of Monro.

onto patient models was required. To the best of our knowledge, no current DICOM software packages easily facilitate these requirements, and, thus, these simulations were completed by using MATLAB. To address concerns that the processing and smoothing algorithms implemented to generate the STL files would not significantly impact the geometric validity of the virtual patient models viewed within MATLAB, the anatomical measurements performed in 3-DSlicer were repeated using the scripts within MATLAB described next. The intraclass correlations of the 2 sets of measurements, considering a 2-way mixed absolute agreement test, were determined to compare these approaches.

Within the MATLAB environment, the *Data Cursor* tool was used to select and store the location of points on or within the STL patient models. Further, mark-up lines could be drawn on the models, and straight-line or curved distances were calculated and saved. Using these tools, the surgeons performing the measurements were able to rotate, zoom, and manipulate the patient models to confirm their point selections. The relative position of the burr hole with respect to the sagittal and coronal sutures was measured by using these tools.

3.3.4 Virtual Instrument Measurements and Analysis

An approximate “virtual” trocar and both curved and straight instruments were superimposed on each patient model to simulate current standard surgical approaches to ETV-ETB and to compare these with novel curved collision-free instruments (Fig. 3.2). For the straight tools, the ”tissue shift” at the *FM* was defined as the straightline distance measured between the instrument midline and the edge of the *FM*, a convention used previously [1],[4]. For the curved instruments, we have assumed that they were constructed from only two segments: a proximal linear (straight) segment and a distal curved segment with the capability to vary tip curvature from a straight configuration to some final desired arc and every variation in between. The optimal position, orientation, and size of the instruments were calculated by using an algorithm previously described [12]. In brief, the procedure involves the following:

The diameter of the physical burr hole in the skull model, representing the actual entry point used in the patients surgery, can be determined through selecting a minimum of 3 points (MATLAB *Cursor* tool) around the peripheral edge of the burr, and a circle can be superimposed to define its boundary. With this method, the circles center position and radius, given in units of millimeters, and the plane defining the circles orientation are inferred. This convention was also used to describe the orientation of the *FM*.

Data previously defined using 3DSlicer, describing the *FM*, the floor of the third ventricle, and a suitable target region for biopsy, are imported into MATLAB and demarcated similarly to the burr hole. The burr hole and surgical targets are used as initial inputs for the optimization algorithm. The algorithm will place a trocar and 2 surgical instruments into the ventricles tracing a collision-free path between the entry point and the surgical targets. It has been assumed that the trocar is represented by a standard Karl Storz operating sheath (cylinder with a radius of 6.5 mm).

With the trocar defined, scripts coded within MATLAB were used to numerically optimize a curved trajectory between the trocar tip and each of the surgical targets [12]. The dexterous virtual instruments are assumed to be a maximum 2 mm in diameter, and this size was factored into the optimization when determining contact avoidance with intraventricular structures.

All virtual tool measurements were performed using three approaches. The first approach assumed that the endoscope was inserted through the ”surgeon-defined burr hole” used in the patients actual surgery. The second and third sets of measurements taken assumed that ”virtual” burr holes were created. The ”optimal virtual burr hole” was selected to minimize the length and curvature of the instruments in reaching both surgical targets. This optimization was motivated by our desire to design a single instrument capable of reaching both targets, while minimizing the instruments length and the required degree of flexion at the distal tip. To achieve this objective, the distal tip of the trocar was incrementally rotated such that the proximal end changed its position (burr-hole location) on the skull. Finally, another ”virtual” burr hole was implemented using the method described by Knaus, Matthias, Koch, and Thomale (KMKT) where the trajectory falls along a line connecting the midpoint between the ETV and ETB target sites and a point at the center of the *FM* [4]. We refer to this method as the ”KMKT-trajectory approach” to avoid confusion. All comparisons between the surgeondefined burr-hole data and both the optimal burr-hole and KMKT-trajectory approaches were completed using a Bonferroni-Dunn post hoc analysis implemented with the R v3.2.0 statistical software package.

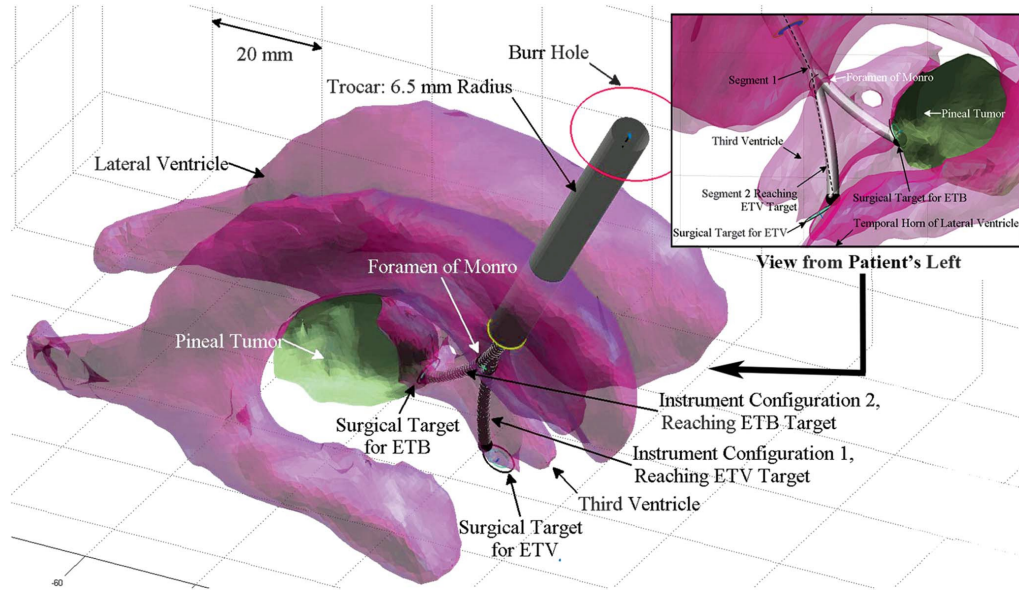


Figure 3.2: Surgical targets and boundaries with virtual curved instrument and trocar superimposed. The curved instruments consist of a linear segment inside the trocar and a curved segment at the distal tip. Note that for visibility purposes, the skull and brain models have been hidden from view in this figure. The image in the upper right represents a closer view of the same instrument configuration, seen from the patients left side and with the view oriented superiorly. ETB, endoscopic tumor biopsy; ETV, endoscopic third ventriculostomy.

3.4 Results

3.4.1 Anatomical Measurements

A summary of the anatomical measurements performed in 3DSlicer and MATLAB are included in Table 4. Similar measurements performed by other groups using standard software packages have also been reproduced [1],[3-4]. Table 5 highlights the orientations of the plane containing the *FM*.

Table 3.4: Comparison of Anatomical Measurements Performed With 3DSlicer and MATLAB to the Literature^{a,,b}.

Anatomical Feature	MATLAB, Mean (Standard Error)	3DSlicer, mm, Mean (Standard Error)	ICC	Previously Reported, mm
FM diameter	7.2 (0.15)	6.9 (0.16)	0.888	6.1-6.9 [4], 5.6-7.8 [1]
MI diameter (AP)	4.4 (0.13)	4.0 (0.14)	0.781	4.3-5.1 [4]
MI diameter (SI)	4.3 (0.13)	5.1 (0.17)	0.868	4.3-5.1 [3]
Anterior 3 rd ventricle diameter	12.6 (0.26)	14.2 (0.33)	0.858	12.1-14.3 [3]
Maximum tumor diameter	28.9 (0.66)	28.5 (0.54)	0.835	24.9-25.6 [3]
TumorMI	8.1 (0.37)	7.3 (0.33)	0.848	8.1-9.0 [3]

^a. AP, anterior-posterior; FM, foramen of Monro; ICC, intraclass correlations; MI, massa intermedia; SI, superior-inferior.

^b. The Midbrain was not segmented and modeled as an STL for this analysis and therefore no measurement was taken in MATLAB. Units in mm.

Table 6 outlines the relative locations of the burr holes for all methods assessed. Significant differences between measurements comparing surgeon-defined with the optimal burr hole(s) are indicated by P values

Table 3.5: Angular Orientation of the Foramen of Monro With Respect to Coronal and Sagittal Planes^a.

Rotations (Degrees) ^a	Mean (Standard Error)
Counterclockwise about posterior-anterior axis (Beta)	43.3 (0.78)
Counterclockwise about inferior-superior axis (Alpha)	57.2 (0.63)

^a. The fixed rotation Beta represents the angle between the plane containing the foramen of Monro and the sagittal plane. The fixed rotation Alpha represents the angle between the plane containing the foramen of Monro and the coronal plane.

less than 0.05. Assuming the use of standard straight instruments, Table 7 summarizes the virtual tissue shift at the *FM*.

Table 3.6: Comparison of Surgical Incision Locations With Respect to Skull Sutures^{a,b}.

	Mean (Standard Error)	Compared With Optimal Burr Hole, P	Compared With KMKT -Trajectory Approach Burr Hole,[4],P	Compared with Zhu <i>et al.</i> [1] Literature Burr Hole, P
Surgeon burr hole				
Coronal suture	14.3(0.85)	.04 ^c	.01 ^c	.99
Sagittal suture	26.8 (0.53)	0.88	0.58	.72
Optimal burr hole				
Coronal suture	22.5 (1.5)	-	.99	.26
Sagittal suture	30.1 (2.3)	-	.05	.99
KMKT-trajectory approach burr hole [4]				
Coronal suture	26.3 (2.5)	-	-	.04 ^c
Sagittal suture	23.4 (1.7)	-	-	.05
Zhu <i>et al.</i> , [1] literature burr hole				
Coronal suture	17 (0.62)	-	-	-
Sagittal suture	30 (0.62)	-	-	-

^a. KMKT, Knaus, Matthias, Koch, and Thomale.

^b. Units in mm.

^c. Bold values are statistically significant.

3.4.2 Virtual Instrument Measurements

The instrument lengths and curvatures required for collisionfree ETV-ETB surgical targeting are summarized in Table 8.

3.5 Discussion

The motivation for this study was to investigate different trajectories for performing a single-incision ETV-ETB, to measure the relevant anatomy for these procedures, and to estimate the required shape of nonlinear (flexible/curved) dexterous instruments for collision-free targeting of multiple surgical sites. This analysis was performed with pediatric data but could be extended to adults. Both 3DSlicer and MATLAB were utilized to select points of interest within the ventricles and to interpolate arced paths between these points. The location of the optimal burr hole was assumed to be at a point on the surface of the skull that provides a corridor with the endoscope tip equidistant from both surgical targets. To

Table 3.7: Virtual Tissue Shift Considering Straight Instruments Compared by Burr-Hole Location^{a.,b.}

	Measurement Means and (Standard Error) by Burr Hole			Comparisons Between Listed Means (P Values)		
	Surgeon Burr Hole	Optimal Burr Hole	KMKT-Trajectory Burr Hole [4]	Surgeon Compared With Optimal, P	Surgeon Compared With KMKT-Trajectory [4], P	Optimal Compared With KMKT-Trajectory [4], P
Anterior	5.6 (1.30)	5.6 (0.73)	5.1 (0.59)	.99	.99	.70
Posterior	7.0 (0.95)	6.0 (0.94)	5.0 (0.52)	.52	.17	.78

^{a.} KMKT, Knaus, Matthias, Koch, and Thomale.^{b.} Units in mm.Table 3.8: Estimated Geometry of Virtual Dexterous Collision-Free Instruments Compared by Burr-Hole Location^{a.,b.}

	Measurement Means and (Standard Error) by Burr Hole			Comparisons Between Listed Means (P Values)		
	Surgeon Burr Hole	Optimal Burr Hole	KMKT-Trajectory Burr Hole [4],	Surgeon Compared With Optimal, P	Surgeon Compared With KMKT-Trajectory [4], P	Optimal Compared With KMKT-Trajectory [4], P
Total instrument length to TM	100.2 (2.0)	90.0 (2.5)	92.2 (0.61)	.002^c	.01^c	.83
Total instrument length to floor of 3rd ventricle	99.1 (2.0)	89.6 (2.4)	91.8 (0.58)	.003^c	.03^c	.74
Length of linear segment	66.3 (0.47)	56.8 (2.3)	58.6 (0.54)	.001^c	.003^c	.93
Arc length from Trocar to TM	33.9 (1.2)	33.2 (1.2)	33.6 (0.31)	.97	.99	.99
Radius of curvature from trocar to TM	49.9 (8.1)	47.7 (3.0)	55.5 (0.77)	.52	.03^c	.26
Arc length from trocar to floor of 3rd ventricle	32.7 (0.77)	32.8 (0.85)	33.2 (0.21)	.99	.98	.83
Curvature from trocar to floor of 3rd ventricle	121.3 (31.0)	47.5 (2.79)	53.3 (1.20)	.01^c	.001^c	.78

^{a.} KMKT, Knaus, Matthias, Koch, and Thomale; TM, tumor.^{b.} Units in mm.^{c.} Bold values are statistically significant.

use the historical patient information available for this study intuitively within the MATLAB software environment, 3-D models of the patients' anatomy were generated. Further, anatomical measurements were performed directly on the original DICOM files in 3DSlicer and compared with repeated measurements using MATLAB. This analysis was performed to assess the 3-D geometric model fit and investigate any limitations that may exist in using the 3-D models after the multiple computations performed to segment and generate the STLs. The intraclass correlation between measurements performed directly on the DICOM files and repeated measurements performed on the 3-D STL data is consistently greater than 0.7. This result supports our assumption that the subsequent measurements taken exclusively in MATLAB regarding the burr-hole placements and virtual instruments are reliable.

Regarding the first objective of this study, the authors have found that the average optimal burr-hole position is located 22.5 mm anterior to the coronal suture and 30 mm lateral to the sagittal suture. These values were determined by calculating an equidistance trajectory to both surgical targets and minimizing the total length of the trajectory to reach these sites. This approach was selected for reasons described in the following paragraphs regarding the design of new collision-free instruments. The optimal and KMKT-trajectory burr holes were found to differ statistically from the original surgeon-defined location. However, there was no statistical difference between the optimal and KMKT-trajectory burr-hole locations. Despite this finding, the average tissue shift at the *FM* for all of the surgical corridors

was similar. All of these findings are, however, statistically different than the average *FM* displacements previously reported with different ETV-ETB patient samples [1],[4]. This observation suggests that the patients in these previous studies may have differed with regard to tumor location.

To identify the patient population within this study, the anatomical measurements completed here can be compared with previous reports. The anatomical dimensions included in the Weill Cornell Medical College study are displayed in Table 4 and the mean values of our measurements are in agreement with the expected ranges based on this study's results. However, standard deviations for the mean values tabulated were not provided, and, therefore, we were unable to statistically compare our results. Only *FM* diameter and tumor size can be directly compared with other studies and do not differ statistically [1],[4].

The second objective of this work was to outline pertinent design measurements for the development of neurosurgical instruments using a patient/procedure-specific approach. Several simplifying assumptions were made in modeling the virtual instruments. The assumed straight segment-curved segment instrument design configuration has been successfully implemented in many laparoscopic devices, such as the SILS Hand Instrument line produced by Covidien, Medtronic Plc (Dublin, Ireland) or the articulation of the ENDOEYE FLEX from Olympus Corporation (Shinjuku, Tokyo, Japan). A limitation of this simple shape assumption is, first, that surgeons cannot control the position and orientation of the tip simultaneously. A higher number of segments would be required to achieve this goal. Nevertheless, based on observation, this instrument structure was sufficient for reaching the targets, despite having the simplest form of increased dexterity.

Second, we assume that the optimal curvatures required to reach the surgical targets are the trajectories that produce the largest radius of curvature while ensuring the instrument remains within the ventricles. Designing large radii instruments minimizes the number of sharp bends the devices must make, easing manufacturability and improving robustness of design. For a surgical task with 2 target sites, the optimal curvature will be such that the radii to reach both targets will be equal and as large as possible. In this manner, a single instrument design is capable of reaching both targets.

A third assumption was that the optimal design configuration will minimize the lengths of each instrument segment. The shorter the length of the overall tool, the greater the stiffness, or tip forces, that can be realized at the distal end. However, because minimizing the instruments overall length and maximizing the radius of curvature are both important for design, we have defined optimal such that our solutions will aim to achieve both goals while respecting the limits of the other. This rationale was used in selecting the optimal burr-hole location discussed previously, and the approach has been previously reported [12]. It should be noted that this algorithm accounts for the geometry of intraventricular structures such as the *FM* and the *MI* by preventing the instruments from coming into contact with the boundaries of these structures.

As seen from the results of Table 8, the burr-hole location directly impacts the instrument length and curvatures. The total instrument length was significantly reduced by relocating the burr hole for both the optimal and KMKT-trajectory approaches. This change will impact the instrument stiffness and thus the maximum achievable tip forces. In addition, the distal instrument curvatures are very sensitive to variations in burr-hole placement. In some cases, the surgeon-defined burr holes tended to require a sharper radius of curvature to reach one of the surgical sites, whereas the other was attainable through a relatively straight trajectory, as seen with the larger standard errors for these values. The optimal configuration requires a radius of curvature approximately equal to 48 mm to reach both surgical

targets. Thus, a single instrument design with a less aggressive bending radius can target both sites. Before performing this analysis, the authors were unsure if the KMKT-trajectory approach was an optimal burr-hole location for curved instrument designs or if this location allowed for the shortest or least aggressive curve. The optimal burr-hole position and KMKT-trajectory instrument designs did not differ significantly, although the optimal location had a tendency for slightly shorter instruments. We conclude that the instrument design specifications for either burr-hole placements are sufficient to design dexterous tools and that the KMKT-trajectory approach is a simple and adequate method for trajectory planning with both standard straight and future dexterous instruments. It is the authors opinion that, although the definition of an optimal trajectory is valuable for initial planning and developing design specifications for procedure-specific instrumentation, in practice, burr-hole placement must be considered on an individual patient basis. Furthermore, we acknowledge that future testing of instruments developed utilizing this approach will need to be completed.

3.6 Conclusion

This work utilizes a simulation-based approach to estimating the average optimal burr-hole location for combined ETV-ETB. In addition, a protocol was established for estimating the shape of curved tools capable of collision-free targeting for a single-corridor ETV-ETB procedure. The burr-hole positioning data and the instrument specifications are intended to address an essential knowledge gap for the development of future surgical instrumentation. In the future, we will describe the prototype curved dexterous tools we have developed using this analysis, which is generalizable for other curved instruments.

3.7 References

- [1] Zhu XL, Gao R, Wong GKC, et al. Single burr hole rigid endoscopic third ventriculostomy and endoscopic tumor biopsy: what is the safe displacement range for the foramen of Monro? *Asian J Surg.* 2013;36(2):74-82.
- [2] Chibbaro S, Di Rocco F, Makiese O, et al. Neuroendoscopic management of posterior third ventricle and pineal region tumors: technique, limitation, and possible complication avoidance. *Neurosurg Rev.* 2012;35(3):331-340.
- [3] Morgenstern PF, Osbun N, Schwartz TH, Greenfield JP, Tsioris AJ, Souweidane MM. Pineal region tumors: an optimal approach for simultaneous endoscopic third ventriculostomy and biopsy. *Neurosurg Focus.* 2011;30(4):1-5.
- [4] Knaus H, Matthias S, Koch A, Thomale UW. Single burr hole endoscopic biopsy with third ventriculostomy-measurements and computer-assisted planning. *Childs Nerv Syst.* 2011;27(8):1233-1241.
- [5] Roth J, Constantini S. Combined rigid and flexible endoscopy for tumors in the posterior third ventricle. *J Neurosurg.* 2015;122(6):1341-1346.
- [6] Pettorini BL, Al-Mahfoud R, Jenkinson MD, Avula S, Pizer B, Mallucci C. Surgical pathway and management of pineal region tumours in children. *Childs Nerv Syst.* 2013;29(3):433-439.
- [7] Ahmed AI, Zaben MJ, Mathad NV, Sparrow OCE. Endoscopic biopsy and third ventriculostomy for the management of pineal region tumors. *World Neurosurg.* 2015;83(4):543-547.
- [8] Morgenstern PF, Souweidane MM. Pineal region tumors: simultaneous endoscopic third ventriculostomy and tumor biopsy. *World Neurosurg.* 2013; 79(2 suppl):9-13.
- [9] Chowdhry SA, Cohen AR. Intraventricular neuroendoscopy: complication avoidance and management. *World Neurosurg.* 2013;79(2 suppl):S15.e1-S15.e10.
- [10] Kikinis R, Pieper S. 3D slicer as a tool for Interactive brain tumor segmentation. In: The Annual International Conference of the IEEE Engineering in Medicine and Biology Society (EMBC 2011); August 30-September 3, 2011; Boston, MA: Institute of Electrical and Electronics Engineers; 2011.

[11] Fedorov A, Beichel R, Kalpathy-Cramer J, et al. 3D slicer as an image computing platform for the Quantitative imaging Network. *Magn Reson Imaging*. 2012;30(9): 1323-1341.

[12] Eastwood KW, Looi T, Naguib HE, Drake JM. Design optimization of neuroendoscopic continuum instruments for third ventriculostomy and tumor biopsy. In: The Annual International Conference of the IEEE Engineering in Medicine and Biology Society (EMBC 2015). Milan, Italy: Institute of Electrical and Electronics Engineers; 2015.

Chapter 4

Kinetostatic Design of Asymmetric Notch Joints for Surgical Robots

4.1 Abstract

We present a kinetostatic model for a needle-sized notched tube continuum joint design, and examine the impact that the design parameters have on both stiffness and joint kinematics. The joint is fabricated by removing a series of asymmetric notches from a metal tube. By fixing a cable to the distal end of the tube, and routing this tendon through the tube's lumen, the joint can be actuated in bending. This simple cutting pattern allows for impressive performance compared to other mechanisms of similar size. However, selecting the cutting geometry using kinematics alone results in many redundant solutions. Since the notches significantly affect the overall structure's stiffness, and limit the maximum forces that it can transmit, a stiffness model can be used to constrain the designspace. Further, because the notch geometry represents a nonprismatic beam configuration, modelling the force-deflection behavior is non-trivial. We have approached this problem using a variation of Castigliano's 2nd Theorem, experimentally validated its performance with several test specimens, and analyzed the behavior of the model over a design space specific to neurosurgical applications. The outcomes of this study aim to aid in the design of joints given task-specific constraints, particularly within the field of surgical robotics.

4.2 Introduction

There is a defined need for miniaturized wristed instruments to better perform surgery in confined and tortuous body spaces, such as the cerebral ventricles [1-3]. However, manufacturing such mechanisms robustly at the millimeter scale is challenging. While there are many well developed jointed-wrist mechanisms in existence, scaling such designs down is limited by costly post-processing and challenging manual assembly, often requiring skilled labor. Continuum robots, specifically designs using super-elastic nitinol tubes, are a well-known solution for addressing this problem. A significant body of work has recently focused on improving nitinol tube continuum mechanisms through cutting and patterning to modify tube topology and macro-scale mechanical performance [4-15]. Historically, similar analyses have been conducted to design stents, clips and coils.

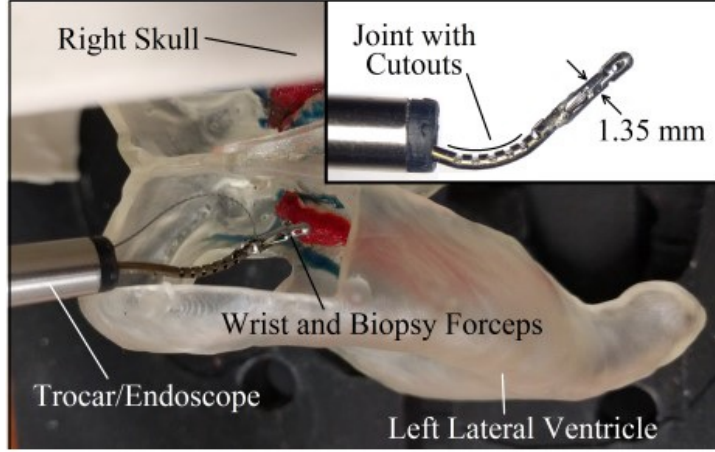


Figure 4.1: Prototype of joint used as a surgical instrument wrist for neuroendoscopic biopsy forceps, shown within the left lateral ventricle of a 3D printed brain model. The left half of the skull is removed for ease of view.

A simple joint design with asymmetric notches was recently presented by York *et al.*, along with kinematic and dynamic models describing its actuation [14]. However, a trade-off analysis considering the impact of these notches on the overall device stiffness, or force-deflection, has yet to be determined. Understanding this relationship is particularly important for applications in neurosurgery, where designing compact and dexterous instruments with adequate stiffness to manipulate tissue has been a challenge. Fig. 4.1 depicts a prototype biopsy instrument, used inside of a synthetic brain model, that demonstrates the tight workspace constraints.

At the intended scale of these designs (< 2 mm diameters), small changes in geometry to achieve greater bending have significant implications for robustness and stiffness performance. An optimal design for such a mechanism will likely require a compromise between both the range of motion and the overall device rigidity. In particular, considering the trade-offs between the range of forces that the mechanism can apply to tissues during surgery and the sharpness of curvature the mechanism can attain.

This work aims to study the impact that the geometric design parameters of the joint have on its kinematic performance (range-of-motion) and on its overall stiffness. To accomplish this assessment, a model of device stiffness, based upon force-deflection, was developed using Castigliano's 2nd Theorem. Further, a sensitivity analysis was conducted to identify which design parameters most significantly impact both range-of-motion and stiffness. Finally, we demonstrate the design of a wrist for neuroendoscopy using these results.

4.3 Review of Prior Modelling

This section will briefly outline the kinematics model proposed by York *et al.* For complete details, we refer the reader to [14]. The joint mechanism consists of a hollow tube with several asymmetric rectangular notches cut into the structure as seen in Fig. 4.2-B. To actuate the joint, a bending moment is applied to its tip by means of a cable (tendon) routed within the lumen of the tube. The asymmetric geometry allows a sharp bend to occur locally at the notches. The tendon displacement represents the actuator space, which can be directly mapped to a configuration space of constant curvature arc

parameters rendered as:

$$\kappa \approx \frac{\Delta l}{h(r_i + \bar{y}) - \Delta l \bar{y}} \quad (4.1)$$

$$s = \frac{h}{1 + \bar{y}\kappa} \quad (4.2)$$

where κ is the curvature of a single notch in deflection and s is the arc length of this segment (Fig. 4.3). The neutral bending plane, or axis in 2D, is the material line that experiences no deformation during bending. The neutral axis's location \bar{y} , with respect to the central axis of the tube, will shift depending on the tube notches as shown in Fig. 4.2-A. The value of \bar{y} can be directly calculated from the geometry of the tube as detailed in [14]. Finally, Δl is the actuating tendon displacement, which is defined for a single notch. These arc parameters can be reconstructed into transformation matrices $T \in \text{SE}(3)$ to describe the shape of the joint:

$$T_{z,a} = e^{\hat{\zeta}a} \quad (4.3)$$

$$\zeta = [0, 0, 1, 0, 0, 0]^T \quad (4.4)$$

$$T_j^{j+1} = e^{\hat{\zeta}_j \kappa s} \quad (4.5)$$

$$\zeta_j = [0, 0, 1/\kappa, 1, 0, 0]^T \quad (4.6)$$

$$T_{z,c} = e^{\hat{\zeta}c} \quad (4.7)$$

$$T_{z,b-c} = e^{\hat{\zeta}(b-c)} \quad (4.8)$$

where j represents the total number of notches, a represents the length of the solid tube before the joint, c represents the cut spacing and b represents the length of solid tube after the joint. The subscript z indicates that the transformations occur in a direction along the central axis of the tube. These transformations are superimposed on a joint in Fig. 4.3. Additional geometric parameters include the cut width h , the cut depth g , the tube's inner radius r_i and outer radius r_o , and L is the total length of the joint as shown in Fig. 4.2-B.

Finally, York *et al.* include an approximation for both the strain ε and the maximum material strain $\max \varepsilon_{\max}$ that is observed in the joint:

$$\varepsilon(y, \kappa) = \frac{\kappa(y - \bar{y})}{1 + \bar{y}\kappa} \quad (4.9)$$

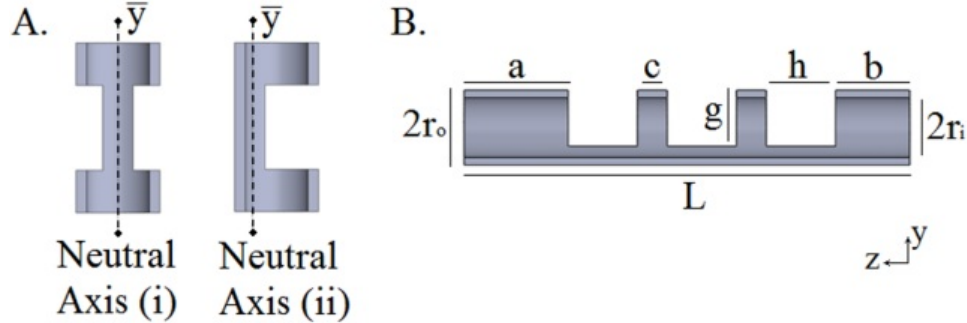


Figure 4.2: The resulting shift of the neutral axis of the joint caused by the notches. (A) The cutting parameters of the joint expressed in units of (mm) (B).

$$\varepsilon_{max} = \frac{r_o - \bar{y}}{r_o + \bar{y}} \quad (4.10)$$

where y represents the distance from the midline of the tube, in a radial direction, to some material point of interest.

4.4 Problem Definition

The aim of this study is to investigate how the joint's performance is impacted by the geometric design parameters outlined in Fig. 4.2-B. To facilitate this investigation, the kinematics model must be recast into a form that produces some output that provides a useful and intuitive representation of range of motion. In Section IV., we describe how we represent this information as a *composite radius of curvature*, $r_{composite}$. Similarly, the *effective stiffness* performance must be modelled and formulated to have an intuitive outcome measure. In Section IV., we also describe a simple model for a loading condition to which the actuation of the joint cannot oppose the applied force. This loading condition represents the limit of performance of the mechanism because the load is opposed purely by the joint's stiffness. Using these two models, in Section V. we first experimentally validate the stiffness model and then implement a sensitivity analysis. We conclude with an example design application to demonstrate how the stiffness model can be implemented for a robotic wrist design in Section VI.

4.5 Model Development

In order to assess the impact that varying the design parameters has on the range of motion of the joint, (9) and (10) can be used to calculate the *maximum allowable curvature* given an assumed ε_{max} , based on the material properties of the joint. With this κ defined for some set of parameters, the transformations of (3) through (8) can be implemented to describe approximately where the body of the joint lies. Considering only the transformation from the base of the first notch T_z, a to the tip of the last notch T_o^t , as labelled in Fig. 4.3, we can superimpose a circular arc onto the joint model and compute $r_{composite}$. The inverse of $r_{composite}$ will be less sharp than the local curvature κ defined at each

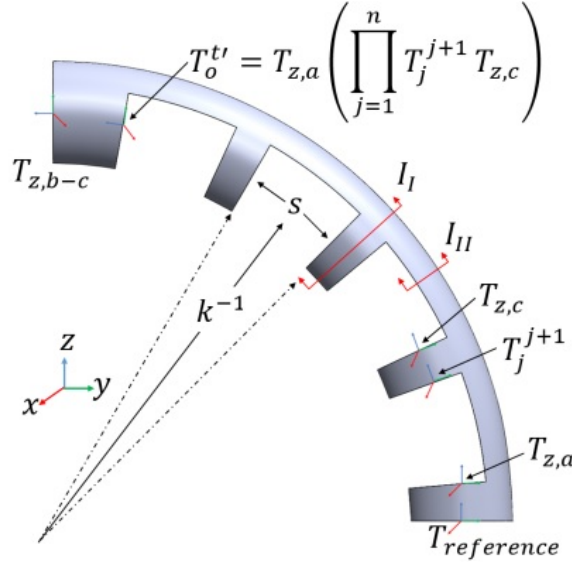


Figure 4.3: Asymmetrically cut joint in bent configuration with transformations superimposed. This design was modelled in [14].

notch. This effect occurs because $r_{\text{composite}}$ will vary depending on c , the cut spacing. In this manner, a reasonable approximation for the shape and reach of the joint is described using two physically intuitive parameters, joint length and radius.

4.5.1 Development of Force-Deflection Model

To analyze the bending stiffness of the joint, we have modelled the weakest loading condition for an externally applied force. For example, to simulate the joint interacting with tissue during surgery. This loading configuration is shown in Fig. 4.4. Where the load is applied such that the second moment of area will be minimal for a given notch profile, and also such that it is acting in a direction that cannot be opposed by the joint's cable actuation. We define this *stiffness model* for the joint as the maximum load that can be applied such that the joint remains below an acceptably defined deflection. Describing the stiffness as a force-deflection is convenient because constraints on maximum allowable deflection and required tip loads are more easily obtained, interpreted and understood than some effective stiffness value. The major challenge in modelling this simple definition pertains to the fact that the stiffness of the joint is significantly impacted by the geometry of the notches removed from the beam's tubular structure. This type of beam is considered non-prismatic, as the cross-sectional area and second moment of area are discontinuous functions of the space curve representing the joint's central axis. In the following sections, we describe a manner of accurately modelling the geometric properties of the beam, and adopting Castigliano's 2nd Theorem, a simple and efficient means of predicting the deflection [16].

4.5.2 Modelling Non-Prismatic Second Moment of Area

The second moment of area $I(z)$, in the joint's direction of bending, is modelled as a discontinuous function of its length:

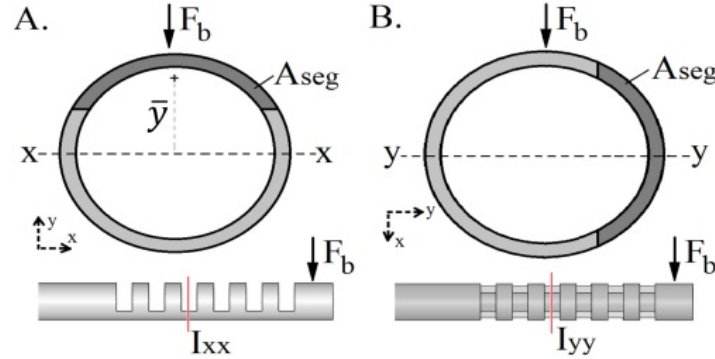


Figure 4.4: Cross section of joint in 'weakest' loading condition where the effective stiffness (EI_{xx}) is lowest and the applied force cannot be opposed by the actuation tendon (A). Cross section of same joint rotated 90° in a configuration with a higher effective stiffness (EI_{yy}) (B).

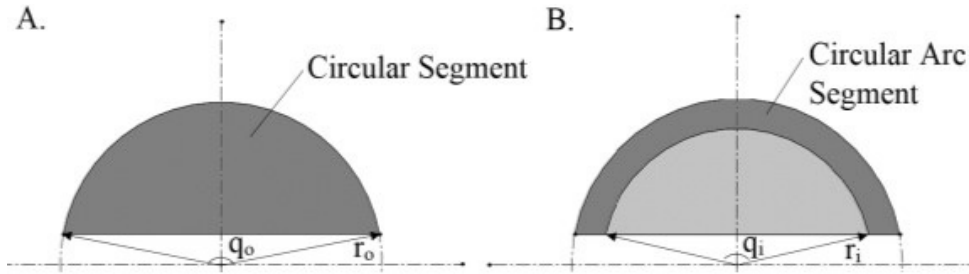


Figure 4.5: Single circular segment for which the second moment (I_s) is calculated using (12) and the area (A_s) using (13) (A). The difference between two circular segments is used to define the notch geometry (B).

$$I(z) = \begin{cases} \pi(r_o^4 - r_i^4)/4 & \text{if } 0 < z \leq a \\ I_{II} & \text{if } a < z < L - b \\ \pi(r_o^4 - r_i^4)/4 & \text{if } L - b \leq z < L \end{cases} \quad (4.11)$$

where the position along the beam's length is described by $z \in [0, L]$. For the un-cut regions of the tube denoted a , b or c in Fig. 4.2-B, the moment is calculated using the standard formulation for a hollow tube given in (11). However, for the notch regions, $I(z)$ is represented as \tilde{I}_{II} which is calculated using superposition and the following relationship which is the 2nd moment of area of a single circular segment:

$$I_s(r, q) = \frac{\pi r^4}{8} (q - 2\sin(q)\sin^2(q/2)) \quad (4.12)$$

A circular segment is defined by a radius (r) and an angle (q) as shown in Fig. 4.5-A. The area A_s of a circular segment is calculated as follows:

$$A_s(r, q) = r^2(q - \sin(q))/2 \quad (4.13)$$

For our joint application, the area of a notch (A_{seg}), which we will refer to as a circular arc segment, has boundaries defined by the tube's r_i and r_o , as well as two angles q_i and q_o which define the height of the circular arc segment based on the depth of the cut g . The relationship between q , r and g is:

$$q_i = \pi - 2\sin^{-1}(g - r_o/r_i) \quad (4.14)$$

$$q_o = \pi - 2\sin^{-1}(g - r_o/r_o) \quad (4.15)$$

The second moment of the circular arc segment is determined by taking the difference between an inner circular segment and an outer circular segment:

$$\tilde{I}_{II} = I_s(r_o, q_o) - I_s(r_i, q_i) \quad (4.16)$$

Here, the second moment of area of the notch region is expressed with respect to the axis of symmetry of the tube (axis x-x in Fig. 4.4). We must next transform \tilde{I}_{II} to account for the shift in the neutral axis \bar{y} (as seen in Fig. 4.2-A) using the parallel axis theorem. The neutral axis of a circular arc segment is calculated by determining the weighted difference of the neutral axis (\bar{y}_s) of individual circular segments:

$$\bar{y}_s(r, q) = \frac{4r\sin^3(q/2)}{3(q - \sin(q))} \quad (4.17)$$

Therefore, the neutral axis of the circular arc segment is:

$$\bar{y} = \frac{\bar{y}_s(r_o, q_o)A_s(r_o, q_o) - \bar{y}_s(r_i, q_i)A_s(r_i, q_i)}{A_s(r_o, q_o) - A_s(r_i, q_i)} \quad (4.18)$$

Finally, applying the parallel axis theorem, the second moment of area of the joint is computed by combining (16) with the product of (18) and (13):

$$I_{II} = \begin{cases} \pi(r_o^4 - r_i^4)/4 & \text{if } z \cdot bMod(h+c) < c \\ \tilde{I}_{II} - \bar{y}^2(A_s(r_o, q_o) - A_s(r_i, q_i)) & \text{otherwise} \end{cases} \quad (4.19)$$

where the conditional statement is used to determine when either the notch or the spacing occurs along the joint's length.

4.5.3 Beam Deflection Using Castiglianatos Second Theorem

Castigiano's 2nd Theorem is commonly implemented to calculate the deflection of a point on a beam were a load is applied. This method involves integrating the internal energy along the length of the beam, and for this reason, it can be used to evaluate non-prismatic structures [16]. With a tip load F_b applied perpendicular to the beams's central axis, as in Fig. 4.6, the deflection of the tip can be determined. To calculate the deflection of any point along the beam's length, a *dummy load* Q can be applied at some point of interest ξ to determine the deflection at that location. To implment this method, we define the bending moment applied to the beam as:

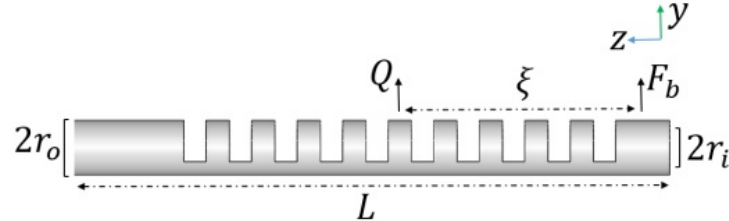


Figure 4.6: Joint with loading notation for Castigliano Model.

$$M(z, \xi) = \begin{cases} -F_b \cdot z & \text{if } 0 < z < \xi \\ -F_b \cdot z - Q(z - \xi) & \text{if } \xi < z < L \end{cases} \quad (4.20)$$

Here, $M(z)$ represents the bending moment variation along the joint's length. For all points z between the tip and the point of interest ξ , $M(z)$ is equal to the blocking force F_b at the joint's tip multiplied its distance to some point z along the beam's central axis. For all points at or between ξ and the joint's base, the dummy load's contribution to the bending moment is added to $M(z)$. In order to implement Castigliano's 2nd Theorem, we begin with the internal energy of the beam:

$$U(z) = \int_0^L \frac{M^2}{2EI} dz \quad (4.21)$$

We then substitute for $M(z, \xi)$ and $I(z)$, splitting the integration between the limits of $[z, \xi]$ and $[\xi, L]$.

$$U(z) = \frac{1}{2E} \left(\int_0^\xi \frac{F_b^2 z^2}{I(z)} dz + \int_\xi^L \frac{(-F_b^2 \cdot z - Q(z - \xi))^2}{I(z)} dz \right) \quad (4.22)$$

The y-displacement ($\Delta y|_{Q=0}$) of the point of interest along the beam can be determined by taking the derivative of U with respect to Q , and then substituting zero for Q 's value:

$$\Delta y = \frac{\partial U(z)}{\partial Q} = \frac{1}{E} \left(\int_\xi^L \frac{(F_b + Q(z - \xi))(z - \xi)}{I(z)} dz \right) \quad (4.23)$$

$$\Delta y|_{Q=0} = \frac{\partial U(z)}{\partial Q} \Big|_{Q=0} = \frac{1}{E} \left(\int_\xi^L \frac{(F_b \cdot z)(z - \xi)}{I(z)} dz \right) \quad (4.24)$$

Equation (24) can be computed for all points of interest (ξ) on the interval $[0, L]$ to predict the shape of the deflected joint, or solely evaluated at zero to predict the tip deflection. Fig. 4.7 illustrates how this model can be simulated in MATLAB to graphically confirm the variation of shape and the deflection of the joint design of interest.

4.6 Model Validation

4.6.1 Validation of Force-Deflection Model

In order to examine the validity of the force-deflection model under small deflections, ten test specimens were evaluated. Using a similar method to [14], the joint samples were cut using a standard two-flute end-

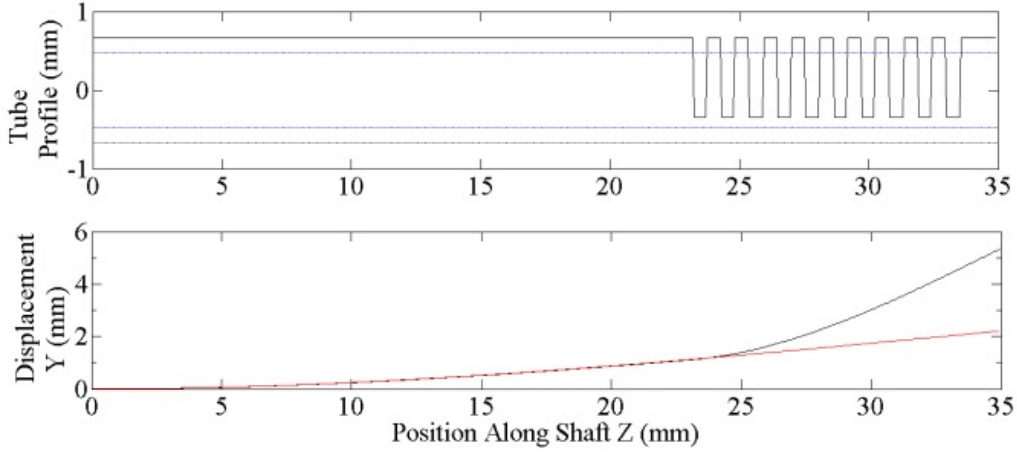


Figure 4.7: MATLAB simulation of joint midline deflection using Castigliano’s 2nd Theorem. This geometry corresponds to specimen 1 in Table I under a 1 N load. The top panel depicts the tube profile, and the bottom shows the joint deflection (black) compared to a soild tube (red).

mill (1/32 in or 0.02 in diameter) on a Minitech Mini-Mill (Minitech Machinery, USA). The specimens were stabilized using a 3D-printed fixation clamp as shown in Fig. 4.8.

The test setup for this validation, and the results of section VI., were assembled on a ThorLabs optical breadboard fit with manual linear translation stages (Newport NewFocus, USA) with 20 μm resolution for fine alignment of the samples, force and displacement sensors. An OptoNCDT 1607 time-of-flight laser displacement sensor (Micro-Epsilon, USA) was used to detect tip displacement and either an FSH00091 or FSH00095 JR S-Beam Load Cell (FUTEK, USA) was used for force measurements. This set-up is also shown in shown in Fig. 4.8.

The samples were randomly selected using a Latin-Hypercube sampling algorithm developed for MATLAB. The tube size (r_o) and number of cuts were modelled using discrete uniform probability distribution functions. The tube sizes were selected based upon available materials (NDC, Confluent Medical Technologies, USA) with Young’s modulus in the range of 50-60 GPa. Further, to more simply describe the entire design space and implement the sampling method, the cutting parameters were recast as dimensionless variables. Specifically, the cut spacing and cut width are now described as a cutting duty cycle D and *Arc Length* which is a multiple of r_o . Similarly, the tube thickness (T) and the linear offsets before and after the joint (A and B) are also multiples of r_o . Additionally, cut depth g is now described as a percentage of the outer diameter ($2r_o$), expressed as G . These changes are summarized here:

$$Duty(D\%) = h/(h + c) \times 100\% \quad (4.25)$$

$$ArcLength = j \times (h + c)/r_o \quad (4.26)$$

$$CutDepth(G\%) = g/2r_o \times 100\% \quad (4.27)$$

$$Thickness(T\%) = (r_o - r_i)/r_o \times 100\% \quad (4.28)$$

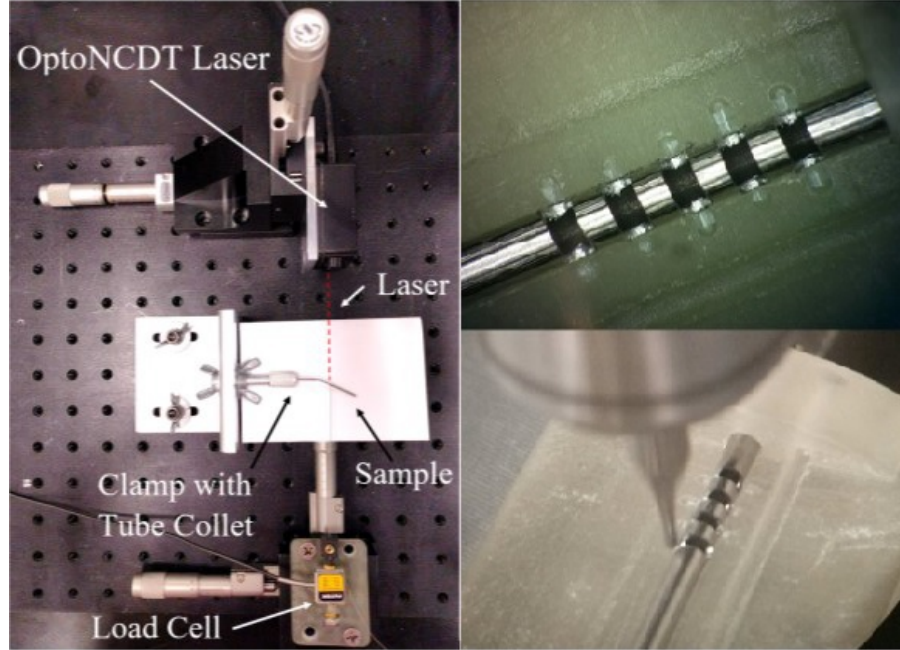


Figure 4.8: Testing and fabrication of test sample (1.3 mm Diameter)

$$\text{OffsetBeforeJoint}(A) = a/r_o \quad (4.29)$$

$$\text{OffsetAfterJoint}(B) = b/r_o \quad (4.30)$$

For the samples, the cut depth G , duty cycle D , and offsets A and B were modelled as uniform probability distribution functions. The geometry, and the ranges used to select the cutting parameters, are summarized in Table I. The parameter ranges used to randomly select the experimental samples were chosen by recursively simulating the force-deflection and kinematics models. With this method, we have aimed to identify parameter ranges that demonstrate the best trade-off between stiffness and range-of-motion. These guidelines will be further verified in future work.

Table 4.1: Summary of Test Sample Geometry

Cutting Parameters	Sample Range	Samples									
		1	2	3	4	5	6	7	8	9	10
Outer Radius (r_o)	-	0.6858	0.6858	0.5842	0.6223	0.6223	0.5842	0.660	0.660	0.775	0.660
Thickness (%T)	-	31.5	31.5	34.8	17.4	17.3	34.8	18.5	18.5	17.5	18.0
Number of Cuts (n)	2-10	5	4	3	6	8	5	10	6	6	6
Cut Depth (%G)	50-80	52.0	66.9	60.7	57.0	63.2	65.9	75.8	75.8	64.5	77.3
Duty (%D)	50-85	73.4	83.4	81.7	65.0	75.1	78.5	49.1	50.0	50.0	50.0
A (r_o)	9-55	44.7	45.2	53.9	10.9	41.1	9.5	34.9	36.8	27.5	33.0
B (r_o)	0.25-4	1.15	0.50	0.86	1.49	1.17	1.11	1.12	0.30	3.50	1.33
Arc Length (r_o)	-	7.88	5.55	4.99	11.77	13.60	8.66	16.61	14.24	12.63	14.88
Standard Error of Experimental Results (mm)	-	0.005-	0.015-	0.007-	0.012-	0.008-	0.03-	0.001-	0.007-	0.016-	0.046-
		0.03	0.03	0.02	0.037	0.045	0.078	0.1	0.06	0.2	0.76

The results of the force deflection experiments are summarized in Fig. 4.9. For each specimen, ten loads in the range of 0-1 N were applied, in increments of 0.1 N. Each of these loading/unloading series of measurements were repeated five times for each joint. The mean deflection of the specimens at each

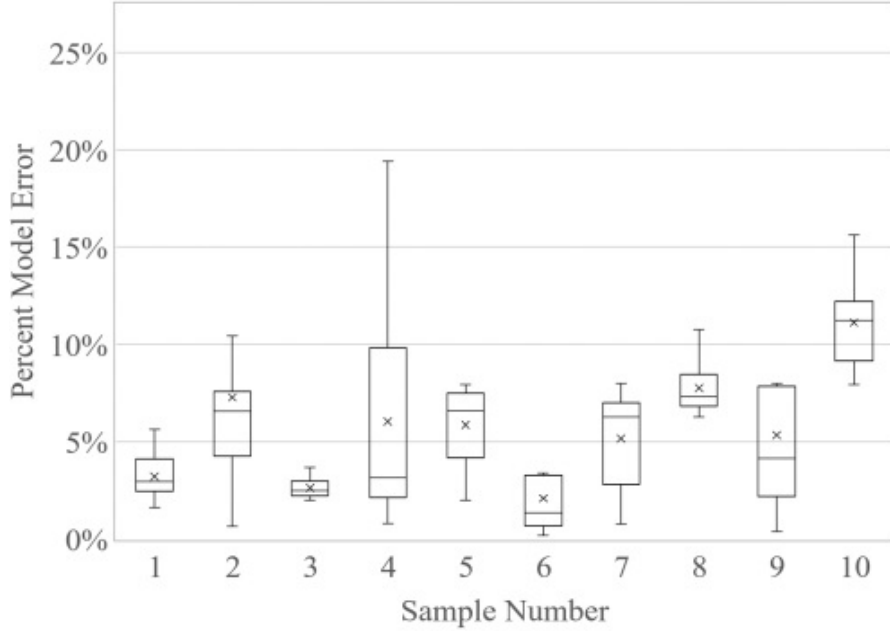


Figure 4.9: Plot of % Error between Model and Experimental Results

load was compared to the predicted displacement using the force-deflection model. These comparison values, expressed as *Percent Model Error*, were calculated by comparing the tip displacement of the model (Δy_{mod}) and experimental results (Δy_{exp}), as follows:

$$\text{PercentModelError} = \|\Delta y_{exp} - \Delta y_{mod}\| / \Delta y_{exp} \times 100\% \quad (4.31)$$

The range of values computed for the *Percent Model Error* for each load are shown, grouped by specimen, in the box plot of Fig. 4.9. From these results, we observe that the model varies by approximately 5% from the actual tip deflections for all loads, across the specimen. We conclude that the force-deflection model provides a reasonable estimate for how the notching affects the overall joint stiffness. Note that several un-cut *control* specimens tubes were tested in force-deflection to verify the Young's modulus of the material.

4.6.2 Sensitivity Analysis

A preliminary sensitivity analysis was conducted to determine the behavior of the joint over a range of design parameters suitable for designs less than 2 mm in diameter. The parameters were sampled using a Monte Carlo based random uniform sampling technique, with 100,000 simulations. The parameters were modelled with uniform probability distribution functions between the bounds summarized in Table II. For simplicity of analysis, the parameter ranges were chosen to be independent.

For the stiffness model, the measured output was the tip deflection, given an assumed blocking force of 0.25 N. This load is based on studies that decomposed the average tip forces encountered in a variety of neurosurgical procedures [17], [18]. For the kinematics model, the composite radius of curvature was the measured output. Scatter plots (Fig. 4.10 and Fig. 4.11) were generated to visually analyze the relationship between the individual parameters and the desired outputs. Considering the results of Fig.

Table 4.2: Bounds for Simulation Parameters

Simulation Parameters ^a	Lower Bound	Upper Bound
Segment length 'a' (mm)	1	3
Tip length 'b' (mm)	1	3
Arc Segment length (mm)	10	30
Duty Cycle (%)	30%	95%
Number of Notches 'j'	2	25
Cut Depth (% of $2r_o$)	51%	90%
Inner Radius ' r_i ' (mm)	0.25	0.4
Outer Radius ' r_o ' (mm)	0.6	0.85

^a. These parameters vary slightly from the design parameters described in the modelling section.

4.10 and Fig. 4.11, we can draw the following observations. First, the joints stiffness is significantly affected by its *arc-length*, r_i and r_o . These findings are expected as beam deflections scale by the 2nd or 3rd order of their length, depending on loading, and inversely by the 4th order of their radii. More interestingly, if we normalize the joint's deflection compared to a solid beam of equivalent size (not shown), the duty cycle and cut depth are the most significant factors affecting both the stiffness model and deflection. Achieving a given joint's desired radius of curvature while maintaining stiffness appears to ultimately require a compromise between these two design parameters. Finally, for small deflections, the models appear to be insensitive to the number of notches n .

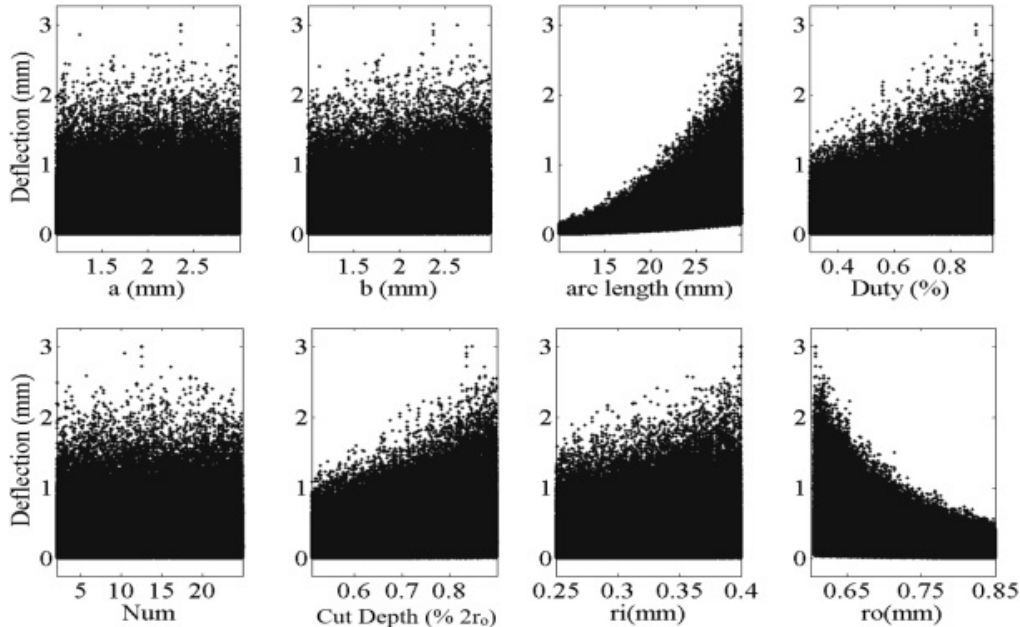


Figure 4.10: Scatter Plot of Parameters for Force-Displacement Model

A major limitation of the proposed stiffness model is that this technique is limited to small deflections. However, the model can nevertheless provide intuition about how relative variations in cutting parameters affect the composite stiffness. Considering the kinematics model alone, the design space to achieve a designated joint radius of curvature and bending angle is very broad. The stiffness model can be used to constrain the design to achieve the maximum stiffness for a given set of parameters while simultaneously achieving the kinematic design goals. Although the small deflection model will not

accurately predict a beam's stiffness when we consider large deflections because of load-stiffening and elastokinematic effects, we expect the results to correlate. The following section will demonstrate how this procedure can be used to aid in constraining the design problem.

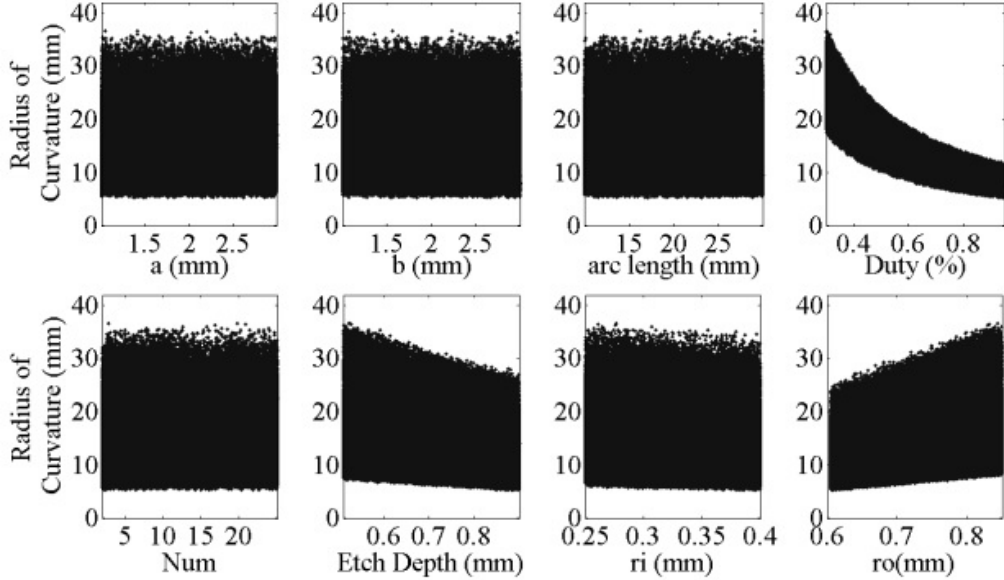


Figure 4.11: Scatter Plot of Parameters for Kinematics Model

4.7 Experimental Implementation

4.7.1 Problem Definition

In order to maximize joint rigidity, designers may intuitively prefer to use solid-tube active cannulas when designing miniature continuum robot wrists. However, in many cases, the material's elastic strain limit can preclude the design of small form-factor wrists with sharp radii of curvature. Consider the well-developed design guidelines for concentric tube robots, from [18] and [19], expressed below:

$$r_{min} = d_o(1 + \varepsilon_{max})/2\varepsilon_{max} \quad (4.32)$$

Here, the sharpest achievable radius of curvature (r_{min}) of an active cannula is shown to be proportional to the tube material's elastic strain limit ($\varepsilon_{max} = 6\text{-}8\%$ for Nitinol) and the tube's outer diameter d_o . For example, to achieve a radii of curvature of approximately 5 mm, the outer diameter of the inner tube approaches 0.8 mm or less. For applications that require a specific inner-tube lumen diameter this size constraint can pose problems. For example, very commonly, the inner diameter must be large enough to allow for space to route end-effector actuation cables. Using the asymmetric notch joint design, both the outer and inner tube diameter can be increased, while enabling designers to achieve less than 5 mm wrist radii of curvature without surpassing the elastic strain limit. These results can be confirmed by implementing (9) and (10) as constraints into the kinematics presented in [14], as already discussed in Section IV. Ultimately, the tradeoff occurs between maintaining a large enough inner-tube lumen diameter for routing distal components and maintaining a large enough composite stiffness for manipulation tasks while achieving the desired compact joint articulation. The model proposed in this

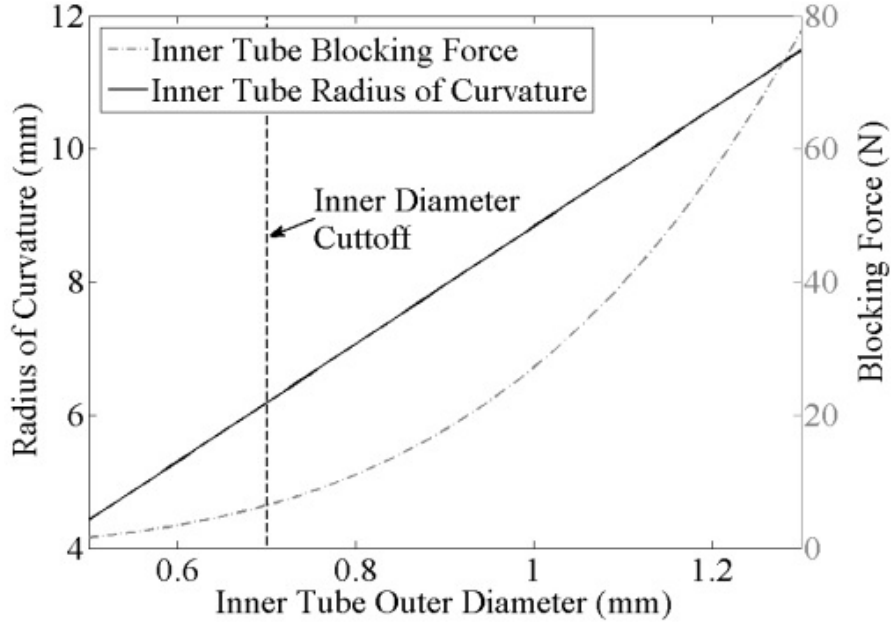


Figure 4.12: Two-tube active cannula design space depicting inner tube radius of curvature versus inner tube outer diameter and blocking force, assuming 0.1 mm wall thickness.

work serves as a design guideline to understand how variations in cutting topology can be utilized to mitigate stiffness loss while attaining the desired motion.

4.7.2 Development of a Task-Specific Surgical Wrist

For a surgical application in the cerebral ventricles of the brain, we desire a wrist mechanism that is less than 2 mm in outer diameter, in order to be compatible with standard equipment. Further, the wrist should achieve a bending angle of 90°, with a radius of curvature less than 5 mm, an arc length less than 10 mm, and should be able to accommodate the routing of two actuation cables, each 0.25 mm in diameter, to operate a push-pull end-effector within its lumen. Additionally, the wrist should be able to support end-effector tip forces greater than 1 N in all directions.

Fig. 4.12 illustrates equation (32) for a concentric-tube un-notched tube wrist. As shown, designing a wrist with a radius of curvature less than 5 mm is not attainable given the requirements for the inner tube outer diameter of 0.7 mm, assuming a minimum tube wall thickness of 0.1 mm, which corresponds to commercially available nitinol tubes (NDC, Confluent Medical Technologies, USA). However, these requirements are possible with the asymmetric-notch design.

Based upon the results of Fig. 4.10 and Fig. 4.11, we select an asymmetric-notch wrist design that maximizes the tube outer radius and minimizes the inner radius, subject to the design constraints, in a similar manner to that of designing an active cannula. The cut depth and cutting duty cycle are optimized to maximize the stiffness to support the required tip loading forces while also allowing for the required range of motion. Since both models are insensitive to the number of cuts, this parameter can be varied based upon the end-mill diameter available for cutting and the total arc length of the joint to achieve the desired cutting duty-cycle. Implementing the desired constraints into the MATLAB optimization toolbox, a suitable solution can be found. This result does not necessarily represent the global optimal

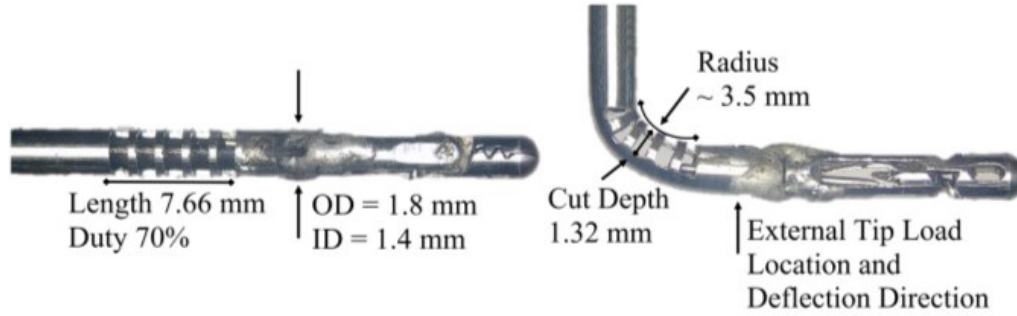


Figure 4.13: Wrist design meeting task specifications. The left configuration is with a 0 N tendon tension and the right with a 40 N tendon tension.

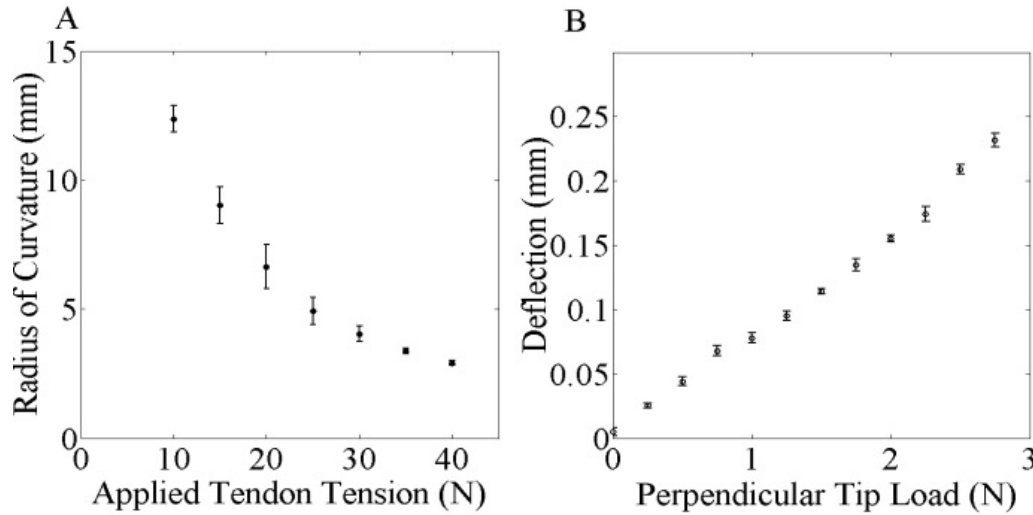


Figure 4.14: Tendon tension vs wrist radius of curvature (A). Forcedeflection behavior of the fully articulated wrist (Tendon Tension 40 N) with an externally applied load at the wrist's tip (B).

solution, but it satisfies the design requirements. The resulting wrist geometry is summarized in Fig. 4.13.

The performance of this wrist was assessed experimentally using a similar experimental set-up to Section V.-A. The joints shape was acquired using two Flea3 1.3 MP cameras (Point Grey, Vancouver Canada) and analyzed using the MATLAB Camera Calibration Toolbox.

The cable tension and composite radius of curvature relationship for the wrist shown in Fig. 4.13 is depicted in Fig. 4.14-A, where the data was averaged over five loading and unloading measurements. Further, with the wrist actuated to a 90° bent configuration, an external tip load was applied in the 'weakest' loading configuration to the position denoted in Fig. 4.13. This load-deflection data is shown in Fig. 4.14-B and was acquired using the same OptoNCDT 1607 laser sensor and Futek load cell as in Section V-A. From these results, we conclude that the wrist design meets the surgical task specifications. The radius of curvature for a 90° bend is below 5 mm and the outer diameter of the wrist is below 2 mm with a large lumen for cable routing. Under an applied tip load of 2 N in the bent configuration, the maximum deflection is approximately 0.25 mm. This deflection is assumed to be acceptable based on the published data that most neurosurgeons have a stationary hold accuracy of 0.4-0.6 mm when completing a manual instrument positioning task [21].

4.8 Conclusion

We have demonstrated the implementation of a simple force-deflection model to predict the composite stiffness of a continuum joint design with asymmetric-notches. This model aids in constraining the design problem for developing these joints by predicting the relative impact that the cutting parameters have on the overall joint stiffness. Our future work will focus on extending this model for use in large deflection configurations when the joint is fully articulated.

4.9 References

- [1] S. A. Chowdhry and A. R. Cohen, Intraventricular Neuroendoscopy: Complication Avoidance and Management, *World Neurosurg.*, vol. 79, no. 2 Suppl, pp. S15.e110, Feb. 2013.
- [2] H. J. Marcus et. al, Robotics in Keyhole Transcranial Endoscopeassisted Microsurgery: A Critical Review of Existing Systems and Proposed Specifications for New Robotic Platforms., *Neurosurgery*, vol. 10, no. 1, pp. 8496, Mar. 2013.
- [3] S. M. Barber, L. Rangel-Castilla, and D. Baskin, Neuroendoscopic Resection of Intraventricular Tumors: A Systematic Outcomes Analysis, *Minim. Invasive Surg.*, vol. 1, no. 1, pp. 112, Jan. 2013.
- [4] H. Fischer, B. Vogel, W. Pfleging, and H. Besser, Flexible distal tip made of nitinol (NiTi) for a steerable endoscopic camera system, *Mater. Sci. Eng. A*, vol. 273275, pp. 780783, 1999.
- [5] J. Peirs, H. Van Brussel, D. Reynaerts, and G. De Gerssem, A Flexible Distal Tip with Two Degrees of Freedom for Enhanced Dexterity in Endoscopic Robot Surgery, in *The 13th Micromechanics Europe Workshop*, 2002, pp. 271274.
- [6] M. D. M. Kutzer et. al, Design of a New Cable-Driven Manipulator with a Large Open Lumen: Preliminary Applications in the Minimally- Invasive Removal of Osteolysis, in *IEEE International Conference on Robotics and Automation*, 2011, pp. 29132920.
- [7] S. C. Ryu et. al, Feasibility Study of an Optically Actuated MR compatible Active Needle, in *IEEE International Conference on Intelligent Robots and Systems*, 2011, pp. 25642569.
- [8] Y. Haga, Y. Muyari, S. Goto, T. Matsunaga, and M. Esashi, Development of Minimally Invasive Medical Tools Using Laser Processing on Cylindrical Substrates, *Electr. Eng. Japan*, vol. 176, no. 1, pp. 6574, 2011.
- [9] J. A. Bell et al., A Deflectable Guiding Catheter for Real-Time MRIGuided Interventions, *J. Magn. Reson. Imaging*, vol. 35, no. 4, pp. 908915, 2012.
- [10] D. Wei, Y. Wenlong, H. Dawei, and D. Zhijiang, Modeling of Flexible Arm with Triangular Notches for Applications in Single Port Access Abdominal Surgery, in *IEEE International Conference on Robotics and Biomimetics*, 2012, pp. 588593.
- [11] J. Liu, B. Hall, M. Frecker, and E. W. Reutzel, Compliant articulation structure using superelastic NiTiNOL, *Smart Mater. Struct.*, vol. 22, no. 9, 2013.
- [12] H. Azimian, P. Francis, T. Looi, and J. Drake, Structurally-Redesigned Concentric-Tube Manipulators with Improved Stability, in *IEEE International Conference on Intelligent Robots and Systems*, 2014, vol. 2, pp. 20302035.
- [13] J.-S. Kim et. al, Toward a Solution to the Snapping Problem in a Concentric-Tube Continuum Robot : Grooved Tubes with Anisotropy, in *IEEE International Conference on Robotics and Automation*, 2014, pp. 58715876.
- [14] P. A. York, P. J. Swaney, H. B. Gilbert, and R. J. Webster III, A Wrist for Needle-Sized Surgical Robots, in *Proc. IEEE Conference on Robotics and Automation*, 2015, pp. 17761781.
- [15] D.-Y. Lee et. a, Anisotropic Patterning to Reduce Instability of Concentric-Tube Robots, *IEEE Trans. Robot.*, vol. 31, no. 6, pp. 1311 1323, 2015.
- [16] E. M. Odom, Teaching Deflection of Stepped Shafts: Castiglianios Theorem, Dummy Loads, Heaviside Step Functions and Numerical Integration, in *41st ASEE/IEEE Frontiers in Education Conference*, 2011, no. 1, pp. 16.
- [17] H. J. Marcus et. al, Forces exerted during microneurosurgery: a cadaver study, *Int. J. Med. Robot.*

Comput. Assist. Surg., 2014.

[18] J. R. Bekeny, P. J. Swaney, R. J. Webster, P. T. Russell, and K. D. Weaver, Forces Applied at the Skull Base during Transnasal Endoscopic Transsphenoidal Pituitary Tumor Excision, *J. Neurol. Surg. - Part B*, vol. 74, no. 6, pp. 33741, Dec. 2013.

[19] D. C. Rucker, R. J. Webster III, G. S. Chirikjian, and N. J. Cowan, Equilibrium Conformations of Concentric-tube Continuum Robots, *Int. J. Rob. Res.*, vol. 29, no. 10, pp. 12631280, 2010.

[20] P. E. Dupont, J. Lock, B. Itkowitz, and E. Butler, Design and Control of Concentric-Tube Robots., *IEEE Trans. Robot.*, vol. 26, no. 2, pp. 209225, Apr. 2010.

[21] R. Sandoval, R. A. MacLachlan, M. Y. Oh, and C. N. Riviere, Positioning Accuracy of Neurosurgeons, in *The 29th Annual International Conference of the IEEE Engineering in Medicine and Biology Society*, 2007, pp. 2069.

Chapter 5

Design of a Contact-Aided Compliant Notched-Tube Joint for Surgical Manipulation in Confined Workspaces

5.1 Abstract

This work presents a novel miniature contact-aided compliant joint mechanism that can be integrated into millimeter-sized manual or robotic surgical instruments. The design aims to address the trade-off between notched-tube compliant joints range-of-motion and stiffness, while also ensuring a compact form-factor. The mechanism is constructed from a nitinol tube with asymmetric cutouts and is actuated in bending by a cable. The innovative feature of this design is the incorporation of a contact-aid into the notched-tube topology which acts to both increase the stiffness of the joint and change the shape that it undertakes during bending. Using finite element modelling (FEM) techniques, we present a sensitivity analysis investigating how the performance of this contact-aided compliant mechanism (CCM) is affected by its geometry, and derive a kinematics and statics model for the joint. The FEM simulations and the kinematic and static models are compared to experimental results. The design and modelling presented in this study can be used to develop new miniature dexterous instruments, with a particular emphasis on applications in minimally invasive neurosurgery.

5.2 Introduction

Notched-tube compliant joint mechanisms have increasingly been used to construct miniature dexterous medical instruments, such as articulated fiber-optic endoscopic cameras, articulated lasers, suction and irrigation probes, as well as wristed forceps, scissors and drills [116]. More recently, a particular focus on adopting this technology for endoscope-guided neurosurgery (neuroendoscopy), to create dexterous wristed instruments, has emerged [1-7],[17]. For these applications, the instruments are typically 1-2 millimeters in diameter and are used to operate within confined workspaces whose dimensions vary

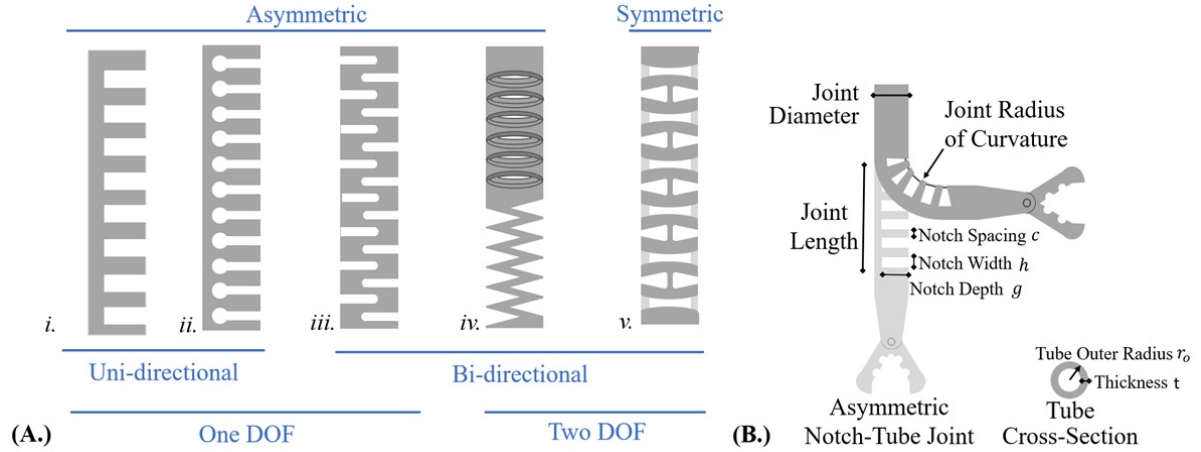


Figure 5.1: Notched-tube topologies previously reported for medical devices [1-16] (A). Example of notch topology incorporated into surgical forceps with notation used to define joint geometry (B).

in the 5-20 mm range [17]. Notched-tube joints are constructed by cutting macro-scale patterns into metal tubes, and can be fabricated in a single process from a single material. In their simplest form, these monolithic geometries can be articulated in bending using an actuation cable, requiring minimal assembly and few additional components. These features allow for this type of joint to be manufactured at millimeter sizes, and for these reasons, they are frequently favored over pin-jointed mechanisms when constructing tools for working in confined body cavities. However, when designing these devices for operating in millimeter-sized workspaces, there is a major design trade-off between joint range-of-motion, joint stiffness and joint compactness.

Some existing notched-tube topologies are depicted in Fig. 5.1-A, and Fig. 5.1-B illustrates an example of how these notch joints can be incorporated into a surgical manipulator. Notched-tube joint designs can be classified as either asymmetric or symmetric, and different combinations of notches create different degrees-of-freedom (DOF) and directions of bending. Asymmetric notch topologies have been found to achieve more compact bending compared to symmetric designs because they fold into themselves during articulation. The simplest notch topology that has been reported is rectangular in shape as shown in design *i* [1-3],[6-10],[13-15]. Over time, additional features have been proposed to modify this basic topology to improve its performance. One such feature includes changing the notch shape to prevent the joint from reaching the materials elastic strain limit by tapering the notches, shown in designs *ii* and *v* [4],[11-12]. A second common feature includes adding fillets to the corners of the notch, or rounding the notch, to reduce strain concentrations at these locations, as seen in *ii*, *iii* and *v* [4],[6-7],[11-15],[18]. As well, the concept of tip-first-closure was recently explored which involves varying the depth of cut of the notches so that the most distal end of the joint articulates closed before the more proximal notches [2]. These modifications have improved the strain profile within the joint and have also helped to ensure the mechanism bends in a compact and space-efficient shape. However, as this type of mechanism is scaled below the 1-2 mm diameter range, the joints stiffness is significantly reduced. Achieving a joint that is both compact and simultaneously stiff enough to manipulate tissue is a major challenge.

Fig. 5.2 depicts different external forces that could be applied to an asymmetric notched-tube joint by manipulating tissue. Loads applied along the x-axis (F_{x+} and F_{x-}) result in significantly lower "error-motions" (undesired deflections) compared to loads applied along the y-axis because of the second-

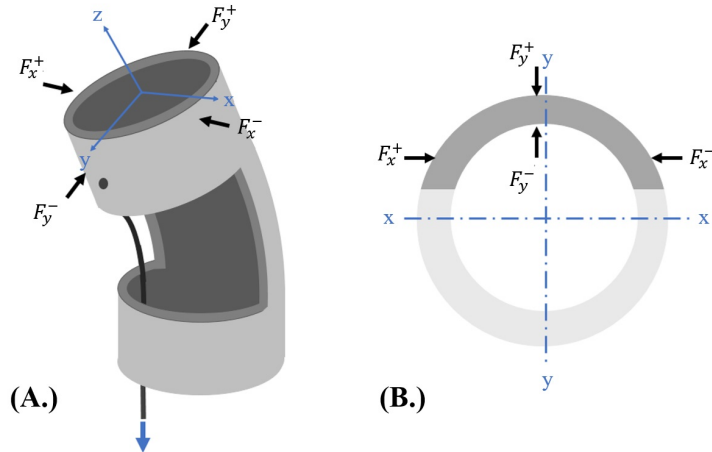


Figure 5.2: Notched-tube segment with externally applied loads (A). Cross-section of tube notch (B).

moment of area of the joint in this orientation. Along the y-axis, where the second-moment and stiffness of the joint is much lower, loads such as F_{y-} can be opposed by tensioning the actuation cable, however, significant error-motions occur when loads are applied in the F_{y+} direction. The current strategies used to address this problem focus on increasing the joint's overall stiffness, and unfortunately tend to oppose the strategies used to achieve compact bending. According to [2] and [3], decreasing the joint's tube diameter and increasing the notch depth appear to have the most significant impact on the compact bending of individual notches, but these strategies also significantly reduce stiffness. This work aims to address the trade-off between compactness and stiffness for conventional topologies by introducing the use of "contact-aids" into the design of asymmetric notched-tube compliant mechanisms.

Contact-aided compliant mechanisms (CCMs) are a category of joint designs in which parts of the compliant members contact or interfere with one another to improve the mechanisms performance [19]. These joint designs have been studied extensively and have shown promise in aerospace, medical and biomimetic inspired robotics applications [20-22]. In particular, CCMs have been used to affect the shape that the compliant mechanism undertakes during actuation, and separately, CCMs have been employed to increase the directional stiffness of a compliant joint [19],[21]. This work presents a new CCM notched-tube cutting geometry that was developed to increase the compact bending of asymmetric notch designs by changing their shape while articulating, and simultaneously, increasing the tip loads that the joint can support, without excessive deflection, during articulation. To the best of our knowledge, this work presents the first example of a CCM incorporated into a notched-tube compliant mechanism. We begin by presenting an overview of the joint topology and the performance benefits of the design. Then, we describe the development of a CCM notch joint for neurosurgical tool applications. Here, finite-element modelling (FEM) techniques have been used to study the impact that the contact-aid geometry has on the joints performance, and to inform the development of a physical prototype. Next, we propose kinematics and statics models to predict the behavior of the joint and guide future prototype optimization and development. Following the modelling, we outline the methods used to fabricate the prototype joints, and describe the experimental techniques used to quantify their performance. Finally, the experimental results are discussed and compared to the FEM, kinematic and statics models.

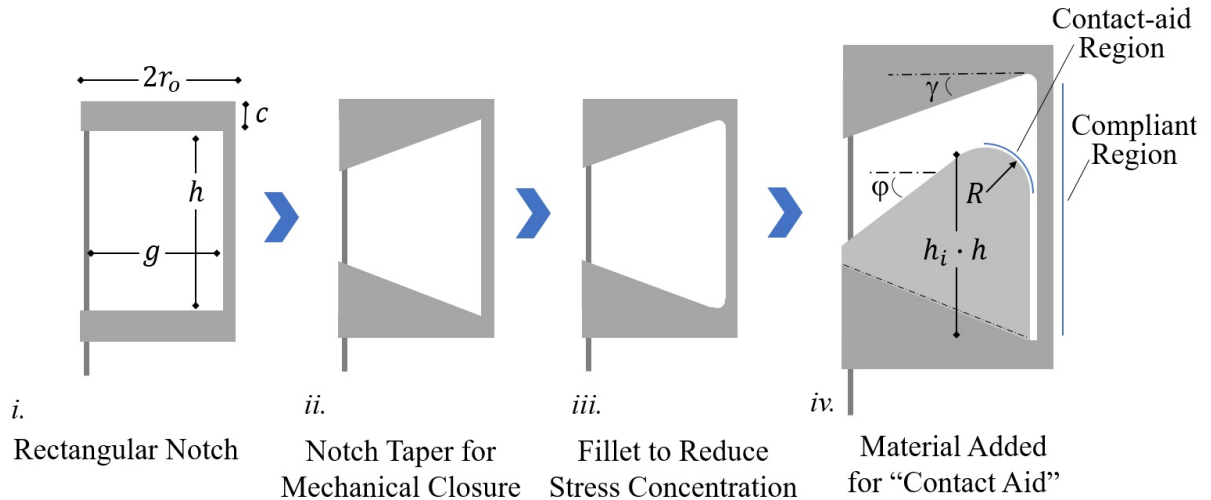


Figure 5.3: Panel depicting how additional design features are added to a rectangular notch to improve performance. Variables used to define the geometry are noted.

5.3 Proposed Design of CCM Notched-Tube Joint

The proposed CCM notched-tube joint is an evolution from previous topology features intended to improve upon the basic rectangular notch topology. Where the other features aimed to avoid exceeding strain limits and avoid strain concentrations, this evolution focuses on improving both the stiffness and the compactness of a notched-tube joint. Fig. 5.3 depicts a design progression showing how the design features were added onto a rectangular notch topology to arrive at the finalized notch prototype.

Here, the CCM notch topology is configured such that the region of the joint undergoing elastic deformation (compliant joint region) comes into point contact with a rigid region (contact-aid region) as it articulates. The shape of the notch is designed such that in the presence of an external tip loading force (F_B), as depicted in Fig. 5.4-A, the joint is stiffened or self-reinforced, and yet bending of the joint is still permitted when a moment is applied by the actuation cable. For rectangular asymmetric notches, external forces applied in the direction shown in Fig. 5.4-A result in the largest displacements. This result occurs because the second-moment of area of the compliant region is the smallest in this orientation and because the applied load cannot be opposed by the actuation cable. The CCM topology aims to address this vulnerability for asymmetric notches by reinforcing the compliant region, as seen in Fig. 5.4-A. Incorporating the contact-aid also influences the shape of the notches compliant region when actuated. The joints compliant region takes on an elliptical shape, as opposed to a circular arc, while bending which allows the joint to bend in a more compact form-factor with less lateral movement. These benefits of improved stiffness and bending compactness are illustrated in Fig. 5.4 which was generated using FEM and is included here for illustrative purposes. Fig. 5.4-A depicts how the stiffness increases when the compliant region touches the contact-aid, and the slope of the force-deflection curve changes from K_1 to K_2 . Fig. 5.4-B depicts the percent reduction in lateral motion of the top edge of the joint for different contact-aid geometries (h_i) when the notch is fully articulated to 30° .

The trade-offs introduced with this design, which include an increase in cable tension and increased strain around the contact-aid, will be considered as part of the sensitivity study for this topology in section 5.4.2.

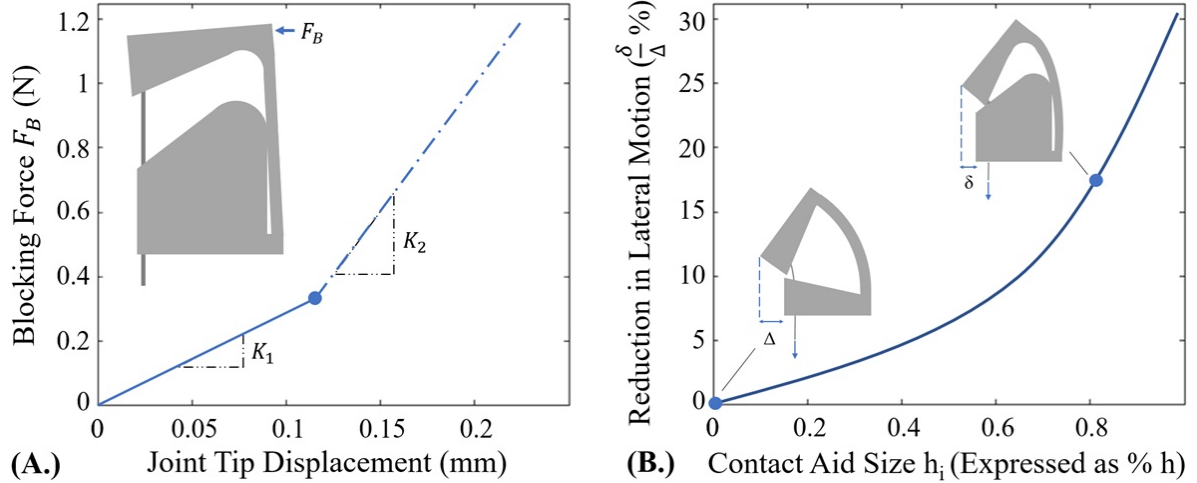


Figure 5.4: Illustrative example demonstrating the behavior of a theoretical contact-aided notched-tube compliant joint compared to a rectangular notched-tube that does not have the contact-aid added

5.4 Prototype Development with a Focus on Neuroendoscopic Instrument Design

To demonstrate an application of the CCM notched-tube joint, it has been incorporated into a neuro-surgical instrument shaft to add wrist-like motion for operating within the ventricles of the brain. With the benefits provided by the CCM notch, the capabilities of the joint are expected to provide sufficient stiffness for tissue manipulation beyond what was previously possible. To construct a neuroendoscopic instrument joint that is compatible with commercial ventriculoscopes, the outer-diameter of the tube should be less than 1.5 mm. For all the joints analyzed in the present work, a tube with an outer-diameter of 1.25 mm and thickness of 0.1 mm was selected to account for any additional covering or sheathing that may be added to the outside of the tube to enclose the notches during surgical use. The physical joints manufactured for this study were constructed from commercially available nickel-titanium (nitinol) tubes (Confluent Medical Technologies Inc., Fremont, CA/USA). Previous work that focused on optimizing the design of a rectangular notched-tube topology for a neuroendoscopic instrument was presented in [3], and this modelling technique was used as a starting point for selecting the geometry and layout of a multi-segment notched-tube joint for this paper. Previous studies have indicated that selecting the minimum length of spacing (c) between the notches will help to achieve the most compact radius of curvature of the joint [1]. Further, using the fewest possible number of deeply cut notches, and maximizing the width of each notch, will also ensure the most compact joint design that can achieve a desired bending angle [2-3]. These design guidelines were incorporated into the selection of the notched-tube geometry. The contact-aid feature was then subsequently added onto this rectangular geometry. The number of notches n , the notch cut depth g , the notch width h and the notch spacing c for a basic asymmetric rectangular topology (Fig. 5.3), onto which the contact-aid is eventually added, are summarized in Table 5.1. The number of notches were chosen to achieve a desired bending angle of approximately 80°. The geometry specific to the contact-aid design is analyzed using FEM and discussed in section 5.4.1.

Table 5.1: Rectangular Notch Joint Geometry Used as Starting Point for Design

Joint Parameters	Value
Tube Outer Radius r_o	0.62 mm
Tube Inner Radius r_i	0.52 mm
Notch Cut Depth g	1.00 mm
Notch Width h	1.60 mm
Notch Spacing c	0.62 mm
Notch Fillet Radius	0.2 mm
Number of Notches n	3
Desired Bending Angle	80 Degrees

5.4.1 Finite Element Modelling for Contact-Aid Sizing

A sensitivity study was conducted using the FEM package ANSYS 15.0 Research Version (ANSYS Inc., Canonsburg, PA, USA) to inform the sizing of the contact-aid geometry shown in Fig. 5.3. The study explores the impact of varying contact-aid geometry on joint stiffness, bending compactness and maximum equivalent strain. To simulate these effects in the case of typical actuation of the joint, an actuation cable was modelled, fixed to the joint and displaced to reproduce the true behavior of the notch when actuated. The material constitutive model for the joint was implemented as a custom shape memory alloy of super-elasticity type, which is included in the ANSYS engineering data section. The model parameters are outlined in Table 5.2, and are based on the properties of nitinol provided by the material manufacturer. The constitutive model for the actuation cable, based on stainless steel, is summarized in Table 5.3.

Table 5.2: Constitutive Model of Nitinol

ANSYS Model Parameters	Value
Youngs modulus of the Austenite phase (E)	55.0 GPa
Poissons Ratio (ν)	0.3
Material response ratio between tension and compression (α)	0
Maximum residual strain (ϵ_l)	0.045
Starting stress value for the forward phase transformation (σ_{SAS})	420 MPa
Final stress value for the forward phase transformation (σ_{FAS})	430 MPa
Starting stress value for the reverse phase transformation (σ_{SSA})	220 MPa
Final stress value for the reverse phase transformation (σ_{FSA})	217 MPa

Table 5.3: Constitutive Model of Steel

ANSYS Model Parameters	Value
Youngs Modulus (E)	200 GPa
Poissons Ratio (ν)	0.3
Yield Stress (σ_{yield})	250 MPa

The model mesh consists of elements of type Solid186, and the mesh size varied in the range of 0.05 mm to 0.15 mm between simulations; this variation was necessary to ensure convergence of a solution. To simulate the attachment between the joint and the actuation cable, a spot weld contact was used, and a frictional contact was specified with a coefficient of friction of 0.3 between the joints inner surface and the outer surface of the cable. A rigid constraint was implemented to fix the joints base, and symmetry conditions were applied along the tubes plane of symmetry so that only half of the model joint was

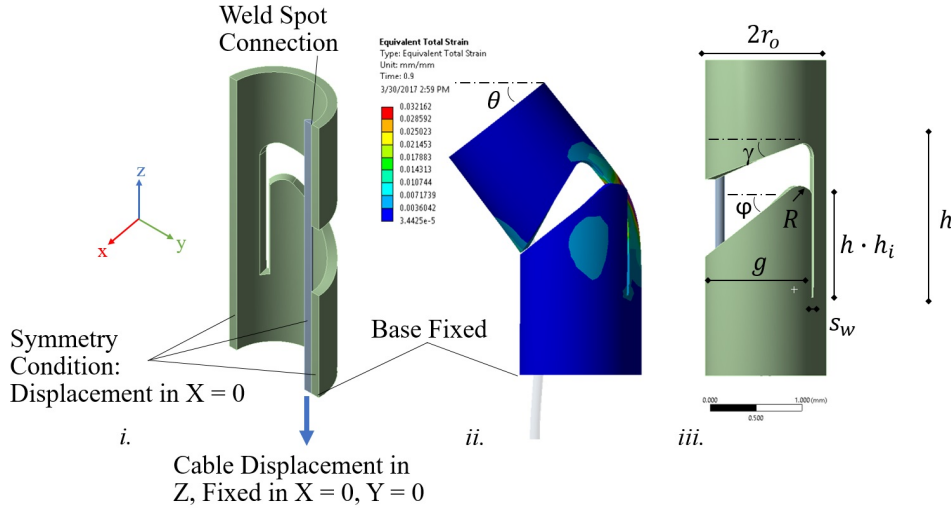


Figure 5.5: Outline of finite element model (FEM) constraints and boundary conditions applied to simulate the notch prototype

simulated. These constraints are annotated in Fig. 5.5. The parameters defining the geometry of the contact-aid topology are also included.

The joint was actuated by defining the inferior surface of the cable to displace a predefined amount in a direction parallel to the long axis of the tube. The displacement set-point for a given simulation was estimated to be equal to the notch length h . However, in many cases, the maximum principle strain of the tube body reached the elastic strain limit or mechanical closure of the tapered edges occurred before this displacement was reached. Therefore, the articulation angle, the joint's radius of curvature, and the cable-displacement were recorded for all sub-steps. To avoid capturing the stretching of the cable in the input, the cable-displacement was measured as the change in Euclidian distance between the interior edges of the notches, similar to the approach used in the kinematics model in section 5.5.1.

Both a single notch and a multi-notch joint design were modelled. A frictional contact was also added between cut surfaces on the tube model to simulate the contact-aid. As well, a second static structural simulation was added to the ANSYS workspace to simulate an applied joint-tip blocking force. This simulation was configured to capture the force-deflection characteristics of the joint to estimate the impact of the contact-aid on the joints blocking-force/stiffness. The loading direction for the force-deflection was along the positive Y-axis in Fig. 5.5.

5.4.2 Simulation Results of Contact Aid Sizing

A simulation of one version of the proposed tube topology is depicted in Fig. 5.6-A. The results of a blocking force experiment shown in Fig. 5.6-B demonstrate how the force-deflection is affected by the introduction of the contact-aid. The effective stiffness, denoted K , of this notch increased by a factor of approximately 2.2 as indicated by the ratio of the slopes of the force-deflection curve K_2 to K_1 . The tip displacement that occurs prior to the shift from K_1 to K_2 is denoted d_c . An optimal design aims to minimize d_c and maximize K_2 .

As outlined in Fig. 5.5, five parameters define the geometry added to the joint to achieve the contact-aid; the contact aid length h_i expressed as a fraction of the notch width h , the top and bottom edge

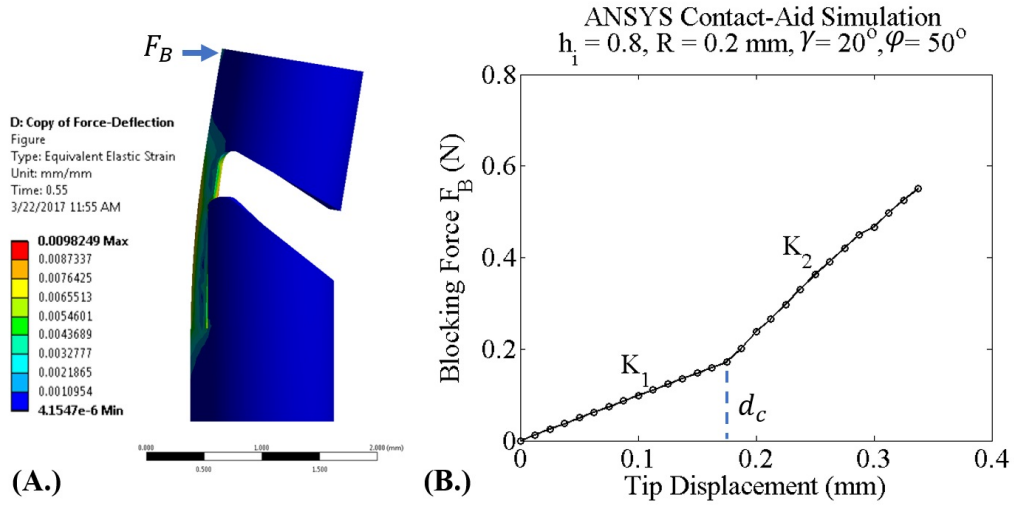


Figure 5.6: Finite Element Model (FEM) of modified joint showing the effect of mechanical interference on blocking force

taper angles γ and φ , the notch spacing c , the slit width s_w , as well as the contact aid radius R . The contact aid length h_i is anticipated to be the most significant topology parameter, and is the focus of the sensitivity study.

To investigate how varying h_i impacts the notch stiffness and notch shape during bending, several ANSYS simulations were conducted (Fig. 5.7). These simulations considered both the force-deflection performance and the maximum strain occurring in the joint when articulated to a 30° bending angle. The two taper angles, γ and φ , were held constant at 20 and 50 degrees, respectively, for this study. These angles provide a maximum bending angle of 30° when the joint is fully closed. From early examination, the taper angles do not appear to have a significant effect on the joint's compactness or stiffness characteristics. The slit width s_w theoretically should be set as small as possible, and is therefore determined by fabrication limits as 0.05 mm, this value will be described in Section 5.7. The contact radius R impacts strain concentrations but appears to have minimal impact on stiffness changes of the joint. Its value was held constant at 0.2 mm for this study.

Fig. 5.7 attempts to capture the four most significant effects that this new notch design has on the joint's behavior, and how these effects vary with h_i . Increasing h_i results in the compliant region coming into contact with the contact-aid earlier and generally having a more significant impact on the joint's stiffness. For example, topologies where h_i is less than 0.5 experience significantly more tip displacement for a 0.4 N tip load because the joint material begins to undergo a phase transformation from Austenite to Martensite before the contact-aid takes effect and the joint's stiffness increases. Ultimately, higher h_i result in lower values of d_c and higher stiffness for a larger range of applied tip forces. However, introducing the contact-aid also increases the strain of the joint by as much as 2% with this geometry. The 6% strain value is marked as this is the elastic strain limit suggested by the manufacturer. The contact-aid also provides a shape change during actuation which reduces the space that the joint takes up laterally. The reduction of this lateral motion is plotted and shows that it can be reduced up to 25% with the selected geometry. Finally, an increase in the maximum cable actuation tension required to fully articulate the notch is observed as h_i increases.

Based on the simulations, a contact-aid design with h_i of 0.8 was chosen because it gave the best

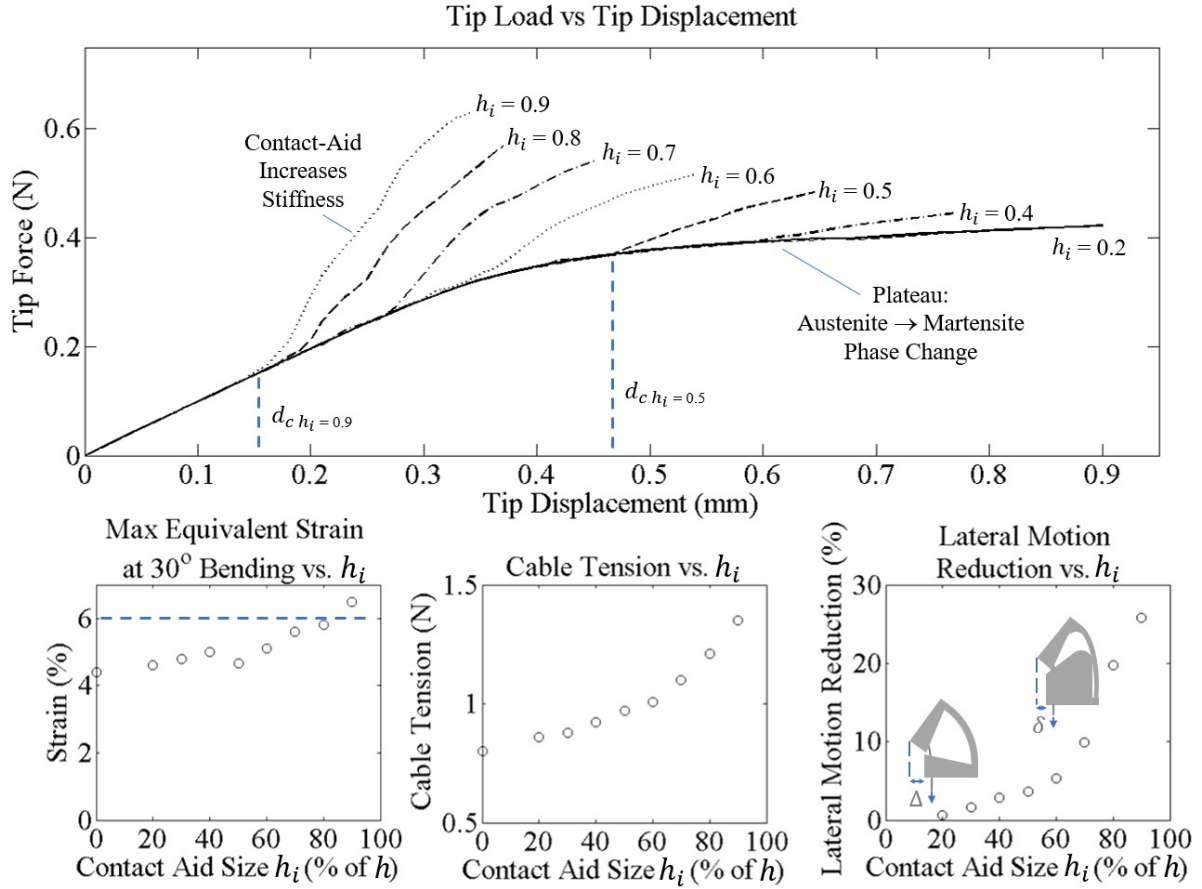


Figure 5.7: Sensitivity of stiffness, max-strain and joint bending compactness to contact-aid joint geometry h_i

performance in terms of increasing the stiffness and reducing the lateral motion without exceeding 6% strain, which was taken to be the elastic limit. The geometry of the test specimen that were fabricated based on this study are summarized in Table 5.4.

Table 5.4: Selected Contact-Aided Joint Parameters (Labelled in Fig. 5.5)

Joint Parameters	Value
Contact Aid Length h_i (% h)	0.8
Top Taper Angle (γ)	20
Bottom Taper Angle (φ)	50
Slit Width s_w	0.05 mm
Contact Aid Radius R	0.2 mm

5.5 Modelling Joint Behavior

5.5.1 Kinematics Modelling

In order to predict the relationship between cable displacement and bending angle for this type of joint, an approximate kinematics model was developed based on the geometry of an individual notch. The

kinematics model approximates the behavior of the joint by assuming that the majority of bending occurs near the contact-aided region, and that the compliant component of the joint wraps around the filleted edge of the contact-aided region, as shown in Fig. 5.8.

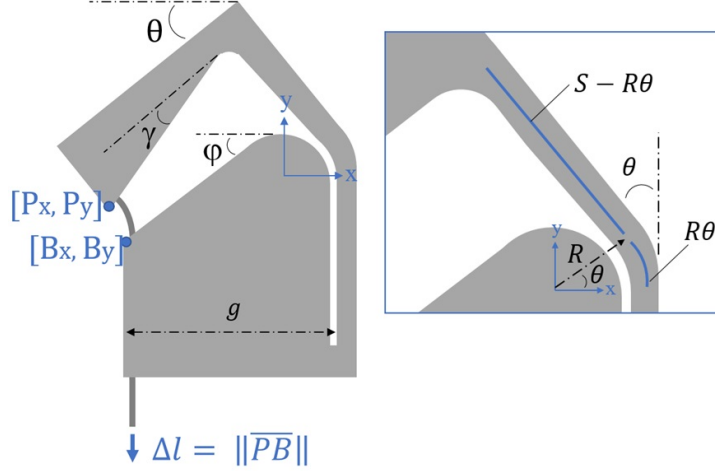


Figure 5.8: Schematic of joint indicating notation used in kinematics model. For kinematics a simplified bending shape is assumed where bending occurs only at contact-aid region.

The kinematics mapping is determined by approximating the locations of the top corner of the notch with coordinates $[Px, Py]$ with respect to the bottom corner of the notch with coordinates $[Bx, By]$, as follows:

$$P_x - B_x = \bar{PB}_x = g - R\cos(\theta) - (S - R\theta)\sin(\theta) - \left(\frac{g - R}{\cos(\gamma)}\right)\cos(\theta + \gamma) \quad (5.1)$$

$$P_y - B_y = \bar{PB}_y = R\sin(\theta) + (S - R\theta)\cos(\theta) - \left(\frac{g - R}{\cos(\gamma)}\right)\sin(\theta + \gamma) - R + (g - R)\tan(\varphi) \quad (5.2)$$

$$\Delta l \approx \left(\bar{PB}_x^2 + \bar{PB}_y^2 \right)^{1/2} \quad (5.3)$$

where Δl is the input cable displacement for a single notch, θ is the joint tip bending angle, g is the cut depth of the notch, γ is the angle of the top taper, φ is the angle of the bottom taper and $S = (1 - h_i)h$, as shown in Fig. 5.8.

5.5.2 Statics Modelling

The cable actuation force required to achieve a desired bending angle can be computed using Castigliano's first theorem:

$$\frac{\delta U(\epsilon)}{\delta \theta} = M = FL \quad (5.4)$$

where $U(\epsilon)$ is the total strain energy stored in the compliant joint, as a function of strain ϵ , θ is the tip bending angle of the joint and M is the bending moment applied to the joint by the actuation cable.

This bending moment can be decomposed into the applied cable tension F and the moment arm L , which is a function of the joint's geometry, expressed as:

$$L = r_i + \bar{y} \quad (5.5)$$

where r_i is the inner radius of the tube and \bar{y} is the location of the neutral bending plane of the compliant joint. This notation is detailed in Fig. 5.9, and the methods used to compute \bar{y} using the geometry of circular segments is discussed in detail in [3].

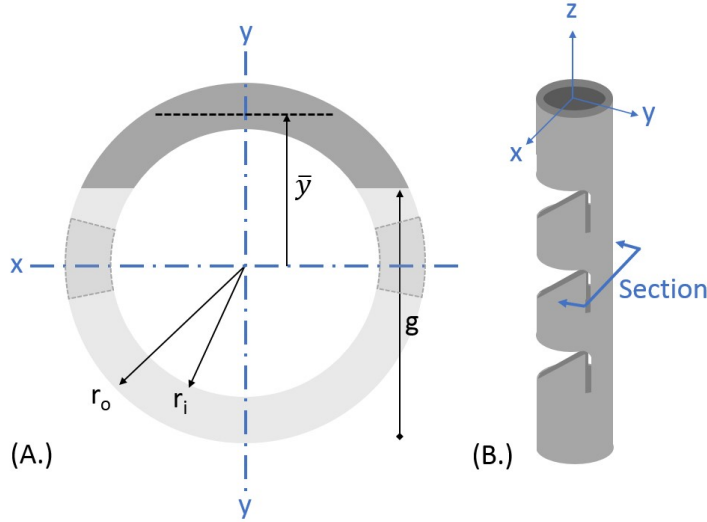


Figure 5.9: Notation for the cross-sectional geometry of a notched-tube compliant joint (A). The dark section in (A.) is the compliant joint region of the joint shown in (B.).

The total strain energy of the joint is computed from the strain energy density $W(\epsilon) = \int \sigma(\epsilon)d\epsilon$, where $\sigma(\epsilon)$ represents the constitutive relationship that maps the stress σ and strain ϵ . For nitinol, a piecewise linear stress-strain curve provides a simplified material model that accurately captures the loading of the joint. This model is expressed as:

$$\sigma(\epsilon) = \begin{cases} \sigma_{lp} & \text{if } \epsilon < \sigma_{lp}/E \\ E\epsilon & \text{if } \sigma_{lp}/E \leq \epsilon \leq \sigma_{up}/E \\ \sigma_{up} & \text{if } \epsilon > \sigma_{up}/E \end{cases} \quad (5.6)$$

To complete this model, a representation of the strain profile within the joint is needed. Assuming that the strain is linearly distributed about the neutral bending plane of the joint \bar{y} , the strain profile through a cross-section of the compliant joint is approximated as:

$$\epsilon(t, y) = \frac{k(t)'(\bar{y} - y)}{1 + \bar{y} \cot k(t)'} \quad (5.7)$$

where $k(t)'$ is the bending curvature of the joint at the location $t \in [0, h]$ along the joints arc-length. Up to this point, the procedure for computing the statics model follows the method used in [1] and [2] which

was applied to a rectangular shaped notched-tube compliant joint that assumed the notch to take-on a constant curvature bending profile while articulating. For the contact-aided compliant joint presented in this work, the shape of the compliant bending region of the joint is assumed to take-on an elliptical arc shape. The tip coordinates of an elliptical arc is defined as follows:

$$P'_y = B \cdot \sin(\tau) \quad (5.8)$$

$$A - P'_x = A \cdot \cos(\tau) \quad (5.9)$$

where the parameters A and B define the width and height of the ellipse and the parameter τ defines the sweep of the arc. The tip coordinates of the end of the arc are $P'_x(\tau)$ and $P'_y(\tau)$ (Fig. 5.10) which are approximated using the kinematics model as:

$$P'_x = (R \cdot \cos(\theta) - R) + (R \cdot \theta - S) \cdot \sin(\theta) \quad (5.10)$$

$$P'_y = R \cdot \sin(\theta) + (S - R \cdot \theta) \cdot \cos(\theta) + h - S \quad (5.11)$$

All of these variables are annotated on Fig. 5.10. The tip orientation of the ellipse is computed as:

$$\theta = \text{atan}\left(\frac{-B}{A} \cdot \cot(\tau)\right) - \frac{\pi}{2} \quad (5.12)$$

Assuming that the coordinates for the arc base at $\tau = 0$ is fixed, the equations can be solved subject to the following equality constraint:

$$h = B \cdot \text{Ellipse}\left(\tau, \left(1 - \frac{A^2}{B^2}\right)^{1/2}\right) \quad (5.13)$$

where the function *Ellipse* is an incomplete elliptic integral of the second kind. This relationship specifies that the arc length of the ellipse segment must equal the initial notch width h , which implies that the neutral axis does not undergo any deformation during bending.

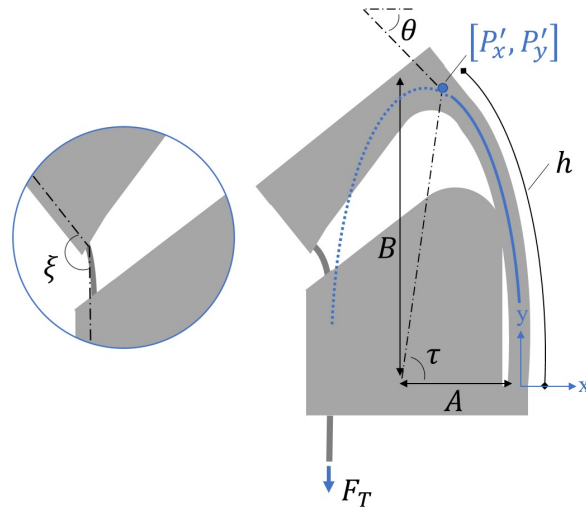


Figure 5.10: Ellipse segment shape fit

With the shape of the ellipse known, the variation of curvature along its length is computed as:

$$k(t) = \frac{AB}{(A^2\cos(\tau)^2 + B^2\sin(\tau)^2)^{3/2}} \quad (5.14)$$

where $k(t)$ is the curvature of the neutral axis \bar{y} . The curvature of the midline of the tube $k(t)'$ is computed as:

$$k(t)' = \frac{k(t)}{1 - k(t) \cdot \bar{y}} \quad (5.15)$$

With the curvature known, the force required to articulate the notch to a desired bending angle can be computed by integrating equation (5.4). However, friction losses from the cable navigating around the corner of a notch must be accounted for. A simple model for this friction loss has been presented in [1-2] and [13]. The actuation force applied on the cable F_T is therefore:

$$F_{cable} = \left(\frac{\sin(\xi/2) - \mu_s \cos(\xi/2)}{\sin(\xi/2) + \mu_s \cos(\xi/2)} \right)^{-2n} F \quad (5.16)$$

where ξ is the angle between the notch edge and tendon, μ_2 is the friction coefficient and n is the number of notches making up the overall joint.

5.6 Fabrication of Notched-Tube Joint Prototypes

A total of five prototype CCM notched-tube joint specimen were fabricated through laser cutting (Pulse Systems, Concord, CA, USA). The performance of this topology was compared to a rectangular notch joint design of equivalent tube radii as well as notch cut depth g , notch height h and notch spacing c , as shown in Fig. 5.11-A. The intent of this comparison is to demonstrate how the behavior of a CCM notch augments the basic notch shape once the contact-aid topology is added to its geometry, effectively comparing $h_i = 0.8$ with $h_i = 0$. The width of the slit feature in the CCM design was limited by the performance of the laser; the smallest width that can be cut is 0.05 mm. Further, because of fabrication constraints, the slits were cut off-axis to the tube at an angle of 15° as shown in Fig. 5.11-B.

5.7 Experimental Methods

The range-of-motion of the test specimen were assessed by measuring the tip bending angle as a function of the cable actuation force. Additionally, the stiffness of the joints were assessed by measuring their tip displacements under an applied tip load. The test setup for these experiments were assembled on a ThorLabs optical breadboard fit with manual linear translation stages (Newport NewFocus, Irvine, CA, USA) that have 20 μm resolution. These stages were used for the fine alignment of the samples with the force and displacement sensors used to collect the data.

5.7.1 Force-Deflection Testing

For the tip displacement versus tip-force experiments, an OptoNCDT 1607 time-of-flight laser displacement sensor (Micro-Epsilon, Ortenburg, Germany) was used to detect the tip's movement and

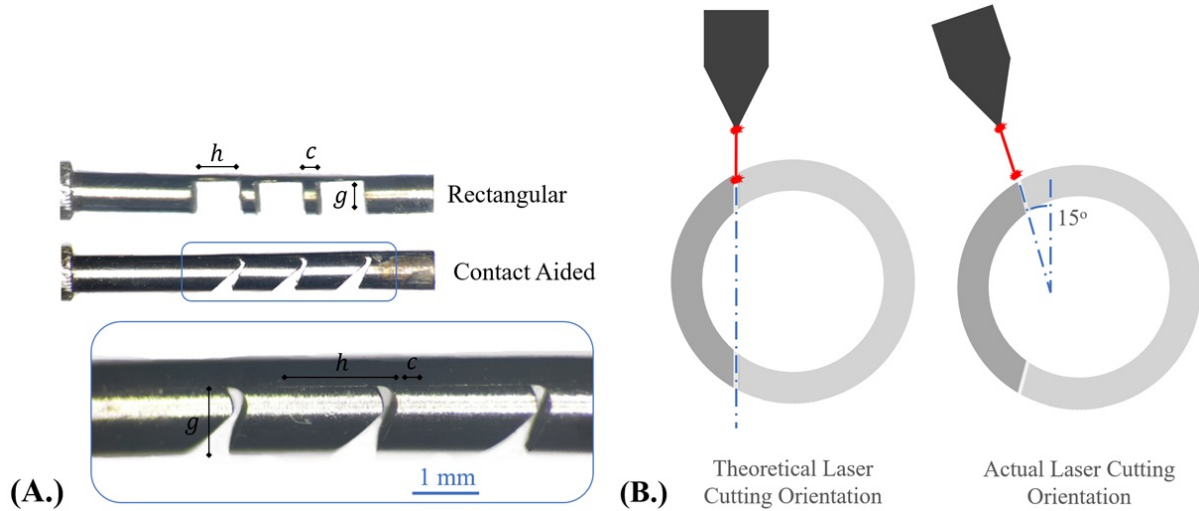


Figure 5.11: Comparison of fabricated rectangular notch joint and joint with contact-aid (A). Schematic of laser cutting orientation used to construct test specimen (B).

an FSH00091 JR S-Beam Load Cell (FUTEK, Irvine, CA, USA) was used to measure the blocking force. This experimental set-up is shown in Fig. 5.12-A.

5.7.2 Range-of-Motion Testing

For the tip bending-angle versus cable-actuation-force experiments, a pair of Flea3 1.3 MP cameras (Point Grey, Vancouver, BC, Canada) were arranged in a stereo-configuration and calibrated using the MATLAB Camera Calibration Toolbox. These cameras were used to track the shape, radius of curvature and bending angle of the joints while an FSH00095 JR S-Beam Load Cell (FUTEK, Irvine, CA, USA) was used to collect cable tension measurements. The error of the measurement system was found to be $\pm [0.01-0.1]$ mm in measuring known radii of curvatures in the range of [3-15] mm. This set-up is shown in Fig. 5.12-B.

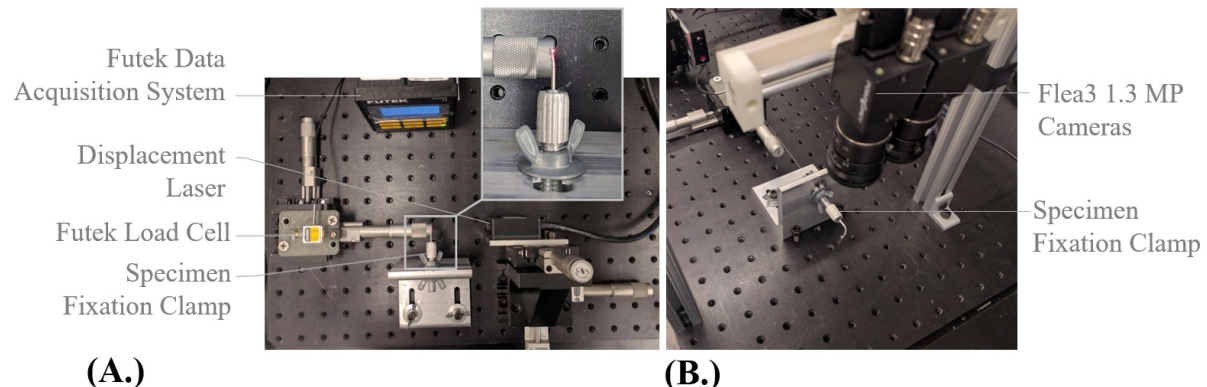


Figure 5.12: Experimental set-up for measuring blocking force and joint range-of-motion

5.8 Experimental Analysis and Model Validation

To verify the anticipated effects of the CCM notches from the sensitivity study in Section 5.4.2, the physical prototypes were compared against an equivalent rectangular notch design with the same cut depth, g and width, h . This comparison can effectively be considered as $h_i = 0.8$ vs. $h_i = 0$. Fig. 5.13 shows a side-by-side comparison of both simulated and physical versions of the CCM notches alongside a rectangular notch joint. By inspecting these images, it can be seen that the CCM notch takes on a more compact bending shape with less lateral motion. It can also be seen that the ANSYS simulations of these different joints agree well with the true shape of the joints. Note the differences in closure between the distal and proximal joints being accurately represented in the simulations. This validates the cable actuated approach used to simulate the actuation of these joints.

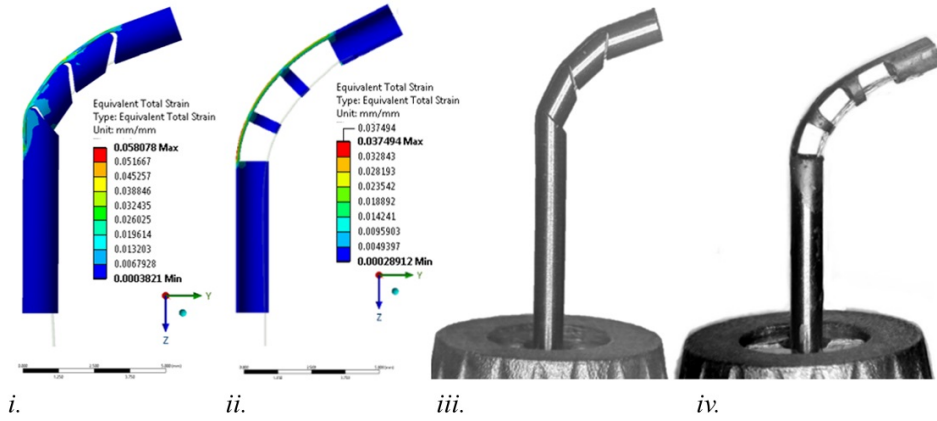


Figure 5.13: Finite element and physical specimen of contact-aided joint and rectangular joint

Next, the blocking-force characteristics of the two joints are compared in Fig. 5.14, where the physical experiments were repeated five times for each data point, and the mean and standard error of the measurements are shown. Both the FEM and experimental data indicate that for a specified "allowable" tip deflection, the CCM design supports blocking forces 1.58 times the magnitude of those applied to the rectangular notch joint.

The kinematics of the contact-aided joint were also simulated using ANSYS and compared to the analytical model presented in Section 5.5.1. These results are compared to experimental data collected from the fabricated specimen in Fig. 5.15.

Fig. 5.16 compares the experimental cable-actuation-force vs bending angle with the ANSYS simulations and the statics model implemented in MATLAB. Note that the statics model only predicts the forward loading of the joint and does not consider joint unloading. The material parameters used in the statics model are summarized in Table 5.5. Additionally, the statics model presented in this work was not applied to the rectangular joint geometry in Fig. 5.16-B. The cable actuation vs bending angle results for the equivalent rectangular notch is included for comparison purposes. Note that the cable tension of the CCM notch joint is increased for the same range of motion.

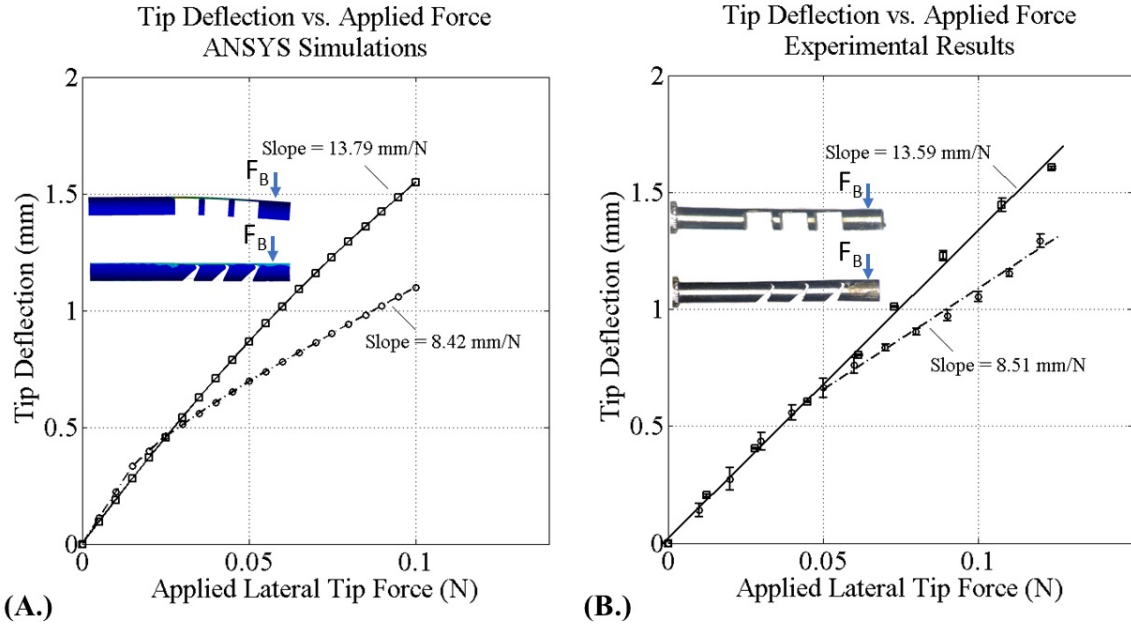


Figure 5.14: Blocking force of rectangular joint and contact-aided joint for ANSYS simulations and physical experiments

Table 5.5: Constitutive Model Used with MATLAB Simulation

MATLAB Parameters	Value
Youngs Modulus E	55 GPa
Upper Plateau Stress σ_{up}	420 MPa
Lower Plateau Stress σ_{lp}	-420 MPa
Coefficient of Friction μ_s	0.3

5.9 Discussion

Previous work on the design of notch tube compliant joint topologies have proposed the addition of different features into a rectangular notch profile in order to improve its performance. These features include adding mechanical stops to limit the notches range-of-motion, filleting the corners of notches to relieve stress concentrations, and progressively increasing the depth to which the notches are cut, from proximal to distal, to create tip-first-closure. All of these augmentations improve the utility of notched-tube joint mechanisms for miniature manipulation tasks, however, there still remains a significant trade-off between achieving joint compactness and maintaining joint stiffness. In this work, we propose the design of a CCM to aid in increasing the joints bending stiffness while providing control over the bending shape of the notch. To the best of our knowledge, this design is the first example of a CCM incorporated into a notched-tube compliant joint. We have presented both simulation and experimental results to demonstrate the effect of this modification, and derive a kinematic and statics model to aid with the future incorporation of this mechanism into robotic manipulators. These models have been validated with experimental data.

The CCM notch design was compared to a joint of equivalent size and initial K_1 stiffness, constructed from rectangular notches following the dimensions outlined in Table 5.1. The purpose of this comparison

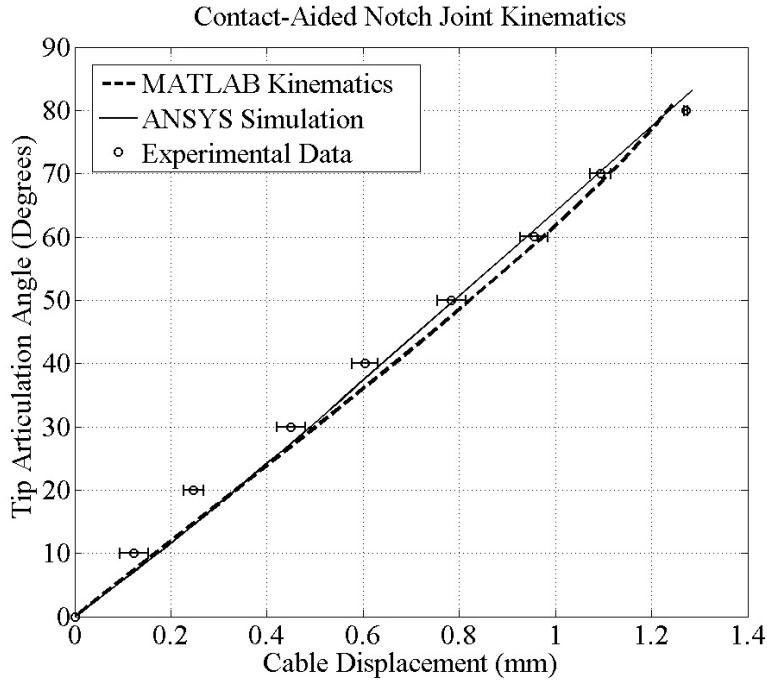


Figure 5.15: Comparison of kinematics model and ANSYS simulation of contact-aided notch joint with experimental results

is to highlight the impact that adding a contact-aid has on the behavior of this equivalently sized notch. This analysis does not consider how the contact-aided topology compares to a rectangular notch that is specifically optimized for stiffness or range-of-motion. The FEM sensitivity study highlights two important benefits of the CCM design. First, the contact-aid increases the bending stiffness of the compliant joint in the loading orientation that is the most susceptible to large, undesirable deflections from external loads. These large deflections result both from the geometry of asymmetric notches and their material behavior. Nitinol is commonly used for these mechanisms because it has a relatively high elastic strain limit, however, the plateau that occurs in its constitutive model results in a significant loss in stiffness for applied tip loads above a certain threshold, as seen in Fig. 5.7. For the particular scales required for neuroendoscopy, the expected lateral tip forces needed for tissue manipulation are in the 0.1-0.5 N range, which is the same range of tip forces where the plateau effect is seen in the simulations [23-24]. The CCM geometry can compensate for the stiffness changes brought about by the phase transition from Austenite to Martensite by reinforcing the notch. The second benefit of the CCM design is to change the shape that the compliant region undergoes during bending. For this particular CCM design, the compliant region undertakes an elliptical shape instead of a constant curvature arc which rectangular notches tend toward. This shape change reduces the lateral motion that the joint undergoes when bending which results in a more compact shape which is critical when working in tight spaces. Previous work on designing notches for compact bending focused on tip-first closure, where the depth of cut of each notch could be varied within a set of notches that make up a joint. This concept of varying cut depth could be used to create new cutting patterns that could provide a shape change without a contact aid. However, this approach alone does not address the loss of stiffness of the joint resulting from the cut-outs in the same manner as the CCM notched-tube design. Ultimately, the sensitivity

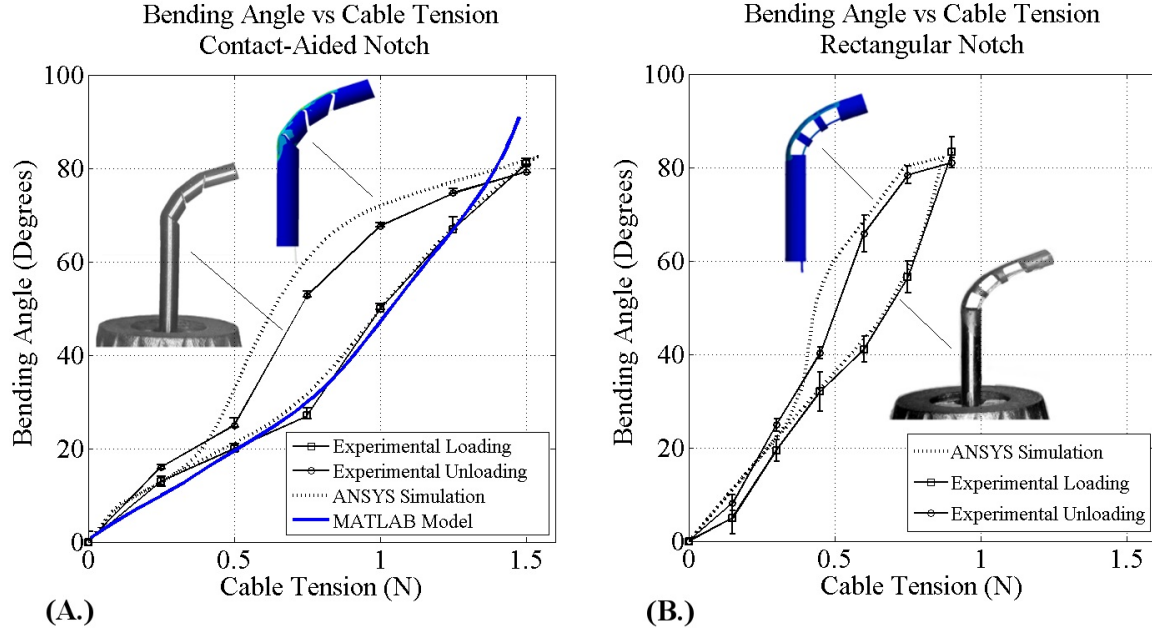


Figure 5.16: Bending angle versus cable tension for notched-tube prototypes

analysis illustrates that the stiffness increase and compactness gained by the CCM design results in strain concentrations around the contact-aid region. This side-effect must be further investigated in future studies.

One of the designs investigated in the sensitivity study was selected and fabricated to validate the FEM results and the models developed in this paper. By inspection, the shape of the joints in Fig. 5.13 show that the CCM notch's overall shape has less lateral motion when compared to its rectangular counterpart, confirming the predictions of the FEM. Further, from Fig. 5.15 we see that both the FEM simulations and the experimental results show an increase in joint stiffness by a factor of approximately 1.6. The results depict an initial region where the force-deflection characteristics of the rectangular joint and the augmented joint coincide. This initial deflection occurs before the compliant region makes contact with the contact-aid. Once the self-reinforcement occurs, the slopes of the plots diverge, and the ratio of these new slopes correlate with an increased resistance to externally applied blocking-forces. Differences between the FEM and experimental figures can be attributed to small alignment errors in clamping the physical prototype and also the shape of the physical specimen under no-loading. The laser cut CCM notches experienced some thermal effects during their manufacturing which resulted in some plastic deformation of the notches. These deformations will affect the amount of displacement (d_c) that it undergoes before touching the contact-aid. Overall, the CCM design improves the effective stiffness K of the joint throughout nearly its full range of motion as desired. This effect is distinct from tapering the notch edges to create mechanical closure in that the joints stiffness only increases when the notch closes at maximum bending.

The results comparing the cable tension vs. bending angle presented in Fig. 5.16 indicate that both the rectangular and contact-aided joint are capable of articulating through the same range-of-motion, which is a bending angle of approximately 80°. The primary difference between the two loading-unloading curves is the cable tension required to articulate the joints. The tensions required for the augmented

joint are approximately double those required for the rectangular joint. Ideally, the contact-aid would only impact the stiffness of the joint against externally applied loads and would have negligible effects on the required cable actuation forces. However, the actuation cables used to articulate joints of this size are capable of supporting loads an order of magnitude higher than these values, and therefore, we expect the increase in cable tension to be manageable for many design variations. Fig. 5.16 also highlights the agreement between the statics model, FEM model and experimental results. In both cases, the constitutive model and coefficient of friction used were the same. The FEM simulation and experimental data for the rectangular asymmetric notch joint in Fig. 5.16-B also aligns very well. Both of these cases provide support that the FEM simulations are an effective predictive design tool for the future development of these mechanisms.

The experimental set-ups depicted in Fig. 5.12 which were used to measure the joint's stiffness and range-of-motion had the following limitations. First, alignment of the samples within the specimen fixation clamp was done manually and therefore the samples were not aligned perfectly orthogonal to the plane of the optical breadboard. To address this limitation, a stereo-camera measurement system was used instead of a single planar camera to capture out-of-plane bending. The measurement errors for radius of curvature, joint arc length and joint angle were quantified by conducting control measurements of twenty sample arcs machined into an aluminum plate. Each arc measurement was repeated five times, and the error ranged from $\pm [0.01-0.1]$ mm in measuring known radii of curvatures in the range of [3-15] mm.

Considering the kinematics model, one of its limitations is the assumption that the majority of bending occurs at the contact region. Based on the results of Fig. 5.15, this assumption holds for the present contact-aid geometry, however agreement with the model may decline as the maximum articulation angle increases above the set-point of 30° . The model also assumes that the compliant region wraps around the fillet radius of the contact region, and as this radius is reduced below the current design of 0.2 mm, this behavior may change.

The most significant limitation of the statics model is that in its present form, it does not incorporate the hysteresis present in nitinol. Therefore, it only models loading of the joint and not unloading. Further, the shape estimation of the notch elliptical arc is contingent on the accuracy of the kinematics model. In the future, developing a kinetostatic model for the joints behavior using the pseud-rigid body model (PRBM) approach may provide a more idealized solution that does not necessitate solving the kinematics and statics models separately.

This study has presented a new design strategy for developing stiff and compact notched-tube joints. Future work on this subject will focus on applying topological optimization techniques such as evolutionary or genetic algorithms to the design of these CCM [20-22]. These tools can be used to critically assess the chosen shape, and consider the impact of the design parameters that were held fixed in this study, such as the edge taper angles. A more global topology optimization may also be able to answer whether a multi-point contact-aid may provide additional performance benefits compared to the single-point contact-aid presented here.

5.10 Conclusion

Here we present an overview of the design of a novel notched-tube contact-aided compliant joint, with a particular emphasis on applications in small workspaces, specifically minimally invasive neurosurgery.

This contact-aided design prototype increases the joints blocking-forces and allows for more compact designs to be developed. The improvements in compactness are achieved by reducing the lateral displacement of the joint when bending and allowing for the use of fewer, longer notch joints which will achieve a desired bending angle while the joint itself occupies a smaller footprint. Future work will focus on the topological optimization of the joint for an application specific task.

5.11 References

- [1] York, P. A., Swaney, P. J., Gilbert, H. B., and Webster III, R. J., 2015, A Wrist for Needle-Sized Surgical Robots, Proc. IEEE International Conference on Robotics and Automation, Seattle, Washington, pp. 17761781.
- [2] Swaney, P. J., York, P. A., Gilbert, H. B., Burgner-Kahrs, J., and Webster III, R. J., 2016, Design, Fabrication, and Testing of a Needle-sized Wrist for Surgical Instruments, ASME Journal of Medical Devices, 11(1), pp. 014501.
- [3] Eastwood, K. W., Azimian, H., Carrillo, B., Looi, T., Naguib, H. E. and Drake, J. M., 2016, Kinetostatic Design of Asymmetric Notch Joints for Surgical Tools, Proc. IEEE/RSJ International Conference on Intelligent Robots and Systems, Deajeon, Hoseo, pp. 2381-2387.
- [4] Kato, T., Okumura, I., Kose, H., Takagi, K., and Hata, N., 2014, Extended Kinematic Mapping of Tendon-Driven Continuum Robot for Neuroendoscopy, Proc. IEEE/RSJ International Conference on Intelligent Robots and Systems, Chicago, Illinois, pp. 19972002.
- [5] Dewaele, F., Kalmar, A. F., De Ryck, F., Lumen, N., Williams, L., Baert, E., Vereecke, H., Okito, J. P. K., Mabilde, C., Blanckaert, B., Keereman, V., Leybaert, L., Van Nieuwenhove, Y., Caemaert, J. and Van Roost, D., 2014, A Novel Design for Steerable Instruments Based on Laser-Cut Nitinol, Journal of Surgical Innovation, 21(3), pp. 303311.
- [6] Mitsuishi, M., Bartolo, P., Kanada, Y., Yoneyama, T., Watanabe, T., Kagawa, H., Sugiyama, N., Tanaka, K. and Hanyu, T., 2013, Force feedback manipulating system for neurosurgery, Proc. First CIRP Conference on BioManufacturing, 5(1), pp. 133136.
- [7] Yoneyama, T., Watanabe, T., Kagawa, H., Hamada, J., Hayashi, Y. and Nakada, M., 2011, Force detecting gripper and flexible micro manipulator for neurosurgery, Proc. Annual International Conference of the IEEE Engineering in Medicine and Biology Society, Boston, Massachusetts, pp. 66956699.
- [8] Bell, J. A., Saikus, C. E., Ratnayaka, K., Wu, V., Sonmez, M., Faranesh, A. Z., Colyer, J. H., Lederman, R. J., and Kocaturk, O., 2012, A Deflectable Guiding Catheter for Real-Time MRI-Guided Interventions, Journal of Magnetic Resonant Imaging, 35(4), pp. 908915.
- [9] Fischer, H., Vogel, B., Pfleging, W., and Besser, H., 1999, Flexible distal tip made of nitinol (NiTi) for a steerable endoscopic camera system, Journal of Materials Science and Engineering: A, 273, pp. 780783.
- [10] Haga, Y., Muyari, Y., Goto, S., Matsunaga, T. and Esashi, M., 2011, Development of Minimally Invasive Medical Tools Using Laser Processing on Cylindrical Substrates, Electrical Engineering in Japan, 176(1), pp. 6574.
- [11] Peirs, J., Van Brussel, H., Reynaerts, D. and De Gersem, G., 2002, A Flexible Distal Tip with Two Degrees of Freedom for Enhanced Dexterity in Endoscopic Robot Surgery, Proc. 13th Micromechanics Europe Workshop, Sinaia, pp. 271274.
- [12] Ryu, S. C., Renaud, P., Black, R. J., Daniel, B. L. and Cutkosky, M. R., 2011, Feasibility Study of an Optically Actuated MR-compatible Active Needle, Proc. IEEE/RSJ International Conference on Intelligent Robots and Systems, San Francisco, California, pp. 25642569.
- [13] Gao, A., Murphy, R., Liu, H., Iordachita, I. and Armand, M., 2016, Mechanical Model of Dexterous Continuum Manipulators with Compliant Joints and Tendon/External Force Interactions, IEEE/ASME Transactions on Mechatronics, 22(1), pp. 465-475.
- [14] Kutzer, M. D. M., Segreti, S. M., Brown, C. Y., Taylor, R. H., Mears, S. C. and Armand, M., 2011, Design of a New Cable-Driven Manipulator with a Large Open Lumen: Preliminary Applications in the Minimally-Invasive Removal of Osteolysis, Proc. IEEE International Conference on Robotics and Automation, Shanghai, pp. 29132920.
- [15] Liu, J., Hall, B., Frecker, M. and Reutzel, E. W., 2013, Compliant articulation structure using superelastic nitinol, Smart Materials and Structures, 22(9), 094018.

- [16] Wei, D., Wenlong, Y., Dawei, H. and Zhijiang, D., 2012, Modeling of Flexible Arm with Triangular Notches for Applications in Single Port Access Abdominal Surgery, Proc. IEEE International Conference on Robotics and Biomimetics, Guangzhou, pp. 588593.
- [17] Eastwood, K. W., Bodani, V. P. and Drake, J. M., 2015, Three-Dimensional Simulation of Collision Free Paths for Combined Endoscopic Third Ventriculostomy and Pineal Region Tumor Biopsy: Implications for the Design Specifications of Future Flexible Endoscopic Instruments, Journal of Operative Neurosurgery, 12(3), pp. 231-238.
- [18] Lobontiu, N., Cullin, M., Petersen, T., Alcazar, J. A. and Member, S., 2014, Planar Compliances of Symmetric Notch Flexure Hinges: The Right Circularly Corner-Filletted Parabolic Design, IEEE Transactions on Automation Science and Engineering, 11(1), pp. 169176.
- [19] Cannon, J. R. and Howell, L. L., 2005, A compliant contact-aided revolute joint, Mechanism and Machine Theory, 40(11), pp. 12731293.
- [20] Halverson, P. A. and Bowden, A. E., 2008, A flexure-based bi-axial contact-aided compliant mechanism for spinal arthroplasty, ASME Paper No. DETC2008-50121.
- [21] Tummala, Y., Wissa, A., Frecker, M. and Hubbard, J. E., 2014, Design and Optimization of a Contact-Aided Compliant Mechanism for Passive Bending, Journal of Mechanisms and Robotics, 6(2), pp. 031013.
- [22] Frecker, M. and Lesieutre, G. A., 2009, Topology optimization of contact-aided compliant cellular mechanisms, Proc. ASME Conference on Smart Materials, Adaptive Structures and Intelligent Systems, New York, New York, pp. 305-315.
- [23] Marcus, H. J., Zareinia, K., Gan, L. S., Yang, F. W., Lama, S., Yang, G.-Z. and Sutherland, G. R., 2014, Forces exerted during microneurosurgery: a cadaver study, The International Journal of Medical Robotics and Computer Assisted Surgery, 10(2), pp. 251-256.
- [24] Bekeny, J. R., Swaney, P. J., Webster, R. J., Russell, P. T. and Weaver, K. D., 2013, Forces Applied at the Skull Base during Transnasal Endoscopic Transsphenoidal Pituitary Tumor Excision, Journal of Neurological Surgery Part B: Skull Base, 74(6), pp. 33741.

Chapter 6

Developing A Dexterous Neuroendoscopic Instrument Using Contact-Aided Compliant Joints

6.1 Abstract

This work presents the development of a new neurosurgical instrument using a patient specific, data-driven approach. The articulate neuroendoscopic instrument (ANI) was designed and built based on specifications set-out by a prior study focusing on tool optimization for endoscopic third ventriculostomy (ETV) and tumor biopsy (ETB). This combined ETV-ETB procedure is a minimally invasive approach to the treatment of hydrocephalus, a dangerous swelling of the brain. Here, we describe the fabrication of the ANI and discuss the design of its major components, including the instrument handle and the dexterous wristed end-effector. Following this section, a kinematics model describing the reachable workspace of the ANI is presented and experimentally validated. Using this model, and the physical prototype, the ANIs function is directly compared to the design specifications set-out in the prior ETV-ETB design optimization study. First, the ANIs wrist shape is measured and the bending radius and joint length is compared to predicted values. Next, the reachable workspace, derived using the kinematics, is superimposed over a set of fifteen 3D-patient models, and the percentage coverage of the surgical targets are measured. The ANI was found to have 100% coverage of the ETV targets and 56% coverage of the tumors. Finally, the ANI tool prototype is assessed in a physical ETV-ETB simulator during a simulated procedure. Overall, the ANI demonstrates a significant improvement in the achievable instrument reach compared to standard tools.

6.2 Introduction

Neuroendoscopy is a form of minimally invasive brain surgery that is typically performed through a single, centimeter-sized incision called a burr-hole. This technique utilizes miniature cameras and long, thin instruments, inserted through a protective sheath called a trocar, to visualize and reach structures deep within the brain [1], [2].

One common indication for neuroendoscopy is in the treatment of hydrocephalus, which is a swelling of the cerebral ventricles. This condition can present under a variety of circumstances, such as in the presence of an intra- or para-ventricular tumor. Here, swelling can occur when the normal circulation of cerebrospinal fluid (CSF) is disrupted. In this situation, an endoscopic third ventriculostomy (ETV) and endoscopic tumor biopsy (ETB) procedure is performed [3][6]. A combined ETV-ETB is completed in two steps, with two separate surgical targets. An ETV is performed to restore the normal circulation of the CSF and reduce the swelling, while an ETB is performed to establish a histological diagnosis of the tumor and inform future treatments for the patient. The ultimate goal of this procedure is to access both targets from a single burr-hole while safely avoiding anatomical obstacles in the cerebral ventricles and minimizing any damage to healthy brain tissue [4].

Despite the success of neuroendoscopy, two recent surveys of neurosurgeons have indicated that the present performance of manual neuroendoscopic tools is hindered by a lack of dexterity in their design [7], [8]. These instruments have semi-rigid and straight shafts, which require surgeons to operate in a straight-line direction from the burr-hole. Although this straight-line operating constraint is an accepted standard, it poses ergonomic problems for surgeons and make even geometrically simple tasks very challenging and time consuming. Improving the reach and dexterity of instruments will allow surgeons to apply neuroendoscopy in new and innovative ways.

Since current instruments require surgeons to operate in a straight-line from the burr-hole, there are many situations where it is not possible to reach both the ETV and ETB targets without significantly displacing the brain and risking further damage. In a previous simulation-based study, we have proposed the use of wristed instruments to access both surgical targets in a collision-free manner from a single burr-hole [9]. This approach enables the instruments to articulate off-axis to reach multiple targets within view of the camera without repositioning the trocar. Holding the trocar in a fixed position reduces the risk of damage to healthy tissue, and is possible when reaching multiple targets with current tools.

In this work, we build on the simulation results of [9], which presents patient-specific design guidelines for new ETV-ETB neurosurgical instruments. Here, we use this data to develop a novel articulate neuroendoscopic instrument (ANI) with a steerable tip. The instrument is constructed by cutting notches into the tool's tube-shaft, to create compliant joints, and it is actuated by-hand using a wire-driven mechanism. This instrument is based on the design of other notched-tube wire-driven joints, which include wristed endoscopes, lasers, suction and irrigation tools, scissor and forceps [10][18]. The topology of the notched-tube shaft presented here is based on the mechanism described in [19].

The paper is organized as follows: Section 2 presents the design and prototyping of the ANI; Section 3 outlines the kinematics of the ANI; Section 4 analyses the reach of the ANI, comparing it to the patient specific ETV-ETB procedure data in [9]; Section 5 presents a surgical simulation of the ANI using a phantom model and the results are discussed; and finally, Section 6 outlines future work.

6.3 Design and Prototyping of Articulate Neuroendoscopic Instrument

The articulate neuroendoscopic instrument (ANI) is presented in three sub-sections: The overall instrument design, the design of the steerable tip and the design of the handle controls. The methods used to prototype the tool are discussed at the end of the section.

6.3.1 Overall Instrument Design

The ANI is a hand-held tool compatible with any standard neurosurgical trocar. The instrument consists of two major components: The tube-shaft with steerable tip and the instrument control handle. Fig. 6.1 demonstrates the tools design and highlights important design features. The tool is operated using a single hand and provides the user control over four degrees-of-freedom (DOF). Assuming the instrument is inserted into the working channel of a trocar, and constrained from moving laterally, the surgeon can control the stroke of the tool into and out of the working channel, the roll of the instruments shaft, the pitch of the instruments tip and actuation of the instruments end-effector.

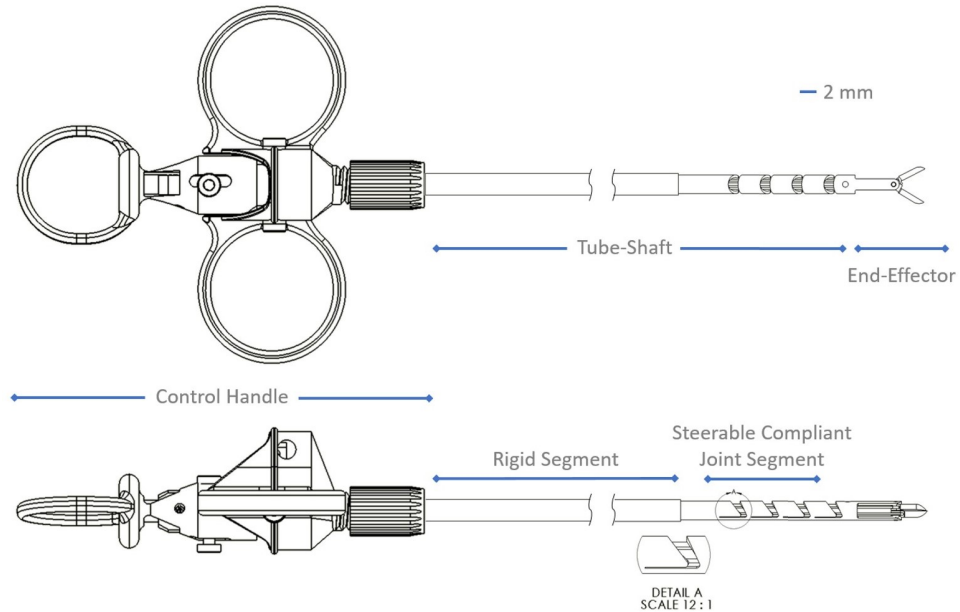


Figure 6.1: Features and design of the ANI

6.3.2 Design of Instrument Tube-Shaft and Steerable Tip

The instrument tube-shaft consists of a rigid segment, a compliant joint segment and an end-effector, as shown in Fig. 6.1. The proximal end of the instrument tube-shaft is rigid and is attached to the instrument handle by means of a collet. This section is 2.25 mm in diameter and approximately 300 mm in length.

The compliant joint segment of the instrument tube-shaft is attached concentrically to the distal end of the rigid segment. The compliant joint segment is constructed by removing a series asymmetric notches from the tube-shaft. An actuation tendon is rigidly attached distal to the notches and routed inside both the compliant and rigid tube-shaft segments. To articulate the compliant joint, tension is applied to the actuation tendon causing the asymmetric notches to fold into themselves and elastically deform the compliant segment to steer the instruments tip. The asymmetric notches are designed with a unique contact-aid feature that causes the notch to interfere with itself during its deformation. This feature increases the load bearing capability of the joint and also changes its bent shape to reduce the foot-print of the joint. The development of the contact-aided notched-tube joint mechanism is described in [19].

The distal end of the compliant joint region includes a pin-joint attachment where either forceps or scissor end-effectors can be added to the tool. Scissor end-effectors are shown in Fig. 6.1. These instrument tips are actuated with two wires that are also routed through the tube-shaft to the control handle.

6.3.3 Design of Control Handle

The instrument control handle is designed to fit in a single hand and provide control of two DOF: One DOF to articulate the end-effector and a second DOF to control the pitch of the tool tip, by means of the compliant joint incorporated into the tube-shaft. Fig. 6.2 includes a panel of images demonstrating how a surgeon-operator controls the instruments DOF. The control handle consists of three primary components: The handle-base, the thumb-gimbal and the thumb-trigger which are outlined in Fig. 6.3.



Figure 6.2: Panel depicting mapping of control motions of handle to steerable tip

The handle-base is the largest component of the handle assembly, and includes two ring loops that the surgeon-operator uses to hold the tool in their hand with their index and ring fingers. The handle-base is further stabilized by placing the middle-finger on the threaded collet mechanism at the distal tip of the handle-base. The tube-shaft is attached to the control handle by means of the threaded collet mechanism. Here, the actuation tendons exit the tube-shaft and follow separate routing paths within the handle based on their function. The actuation wires for the end-effector attach to the thumb trigger and are actuated in a push-pull motion, while the tendon controlling pitch is rigidly attached to the thumb gimbal.

The thumb-gimbal attaches to the handle-base at a pin-joint that allows the thumb-gimbal to articulate 60 degrees. A cable fixture point is eccentrically located from the axis of revolution of the

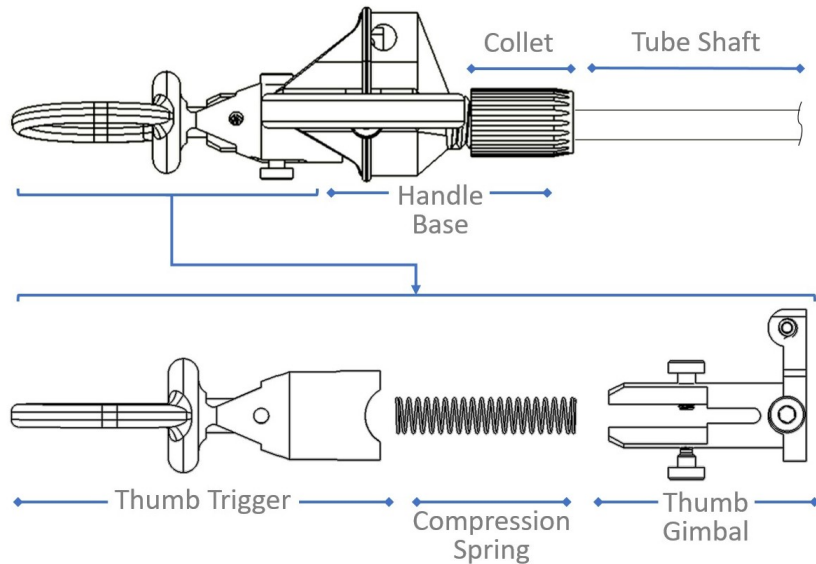


Figure 6.3: Instrument control handle exploded assembly view

thumb-gimbal and is comprised of a set-screw clamp used to anchor the actuation tendon that articulates the compliant joint of the tube-shaft. The compliant joint tendon exits the tube-shaft at the collet mechanism in the handle-base and is routed over a guide pulley before anchoring to the thumb-gimbal cable fixture. The guide pulley is sized such that the ratio of the tendon diameter and the pulley diameter d/D is greater than 20, to minimize the cable fatigue. The eccentric location of the cable fixture creates a moment arm of 11.75 mm from the axis of revolution such that the compliant joint tendon is contracted as the thumb-gimbal is rotated as shown in Fig. 6.2.

The thumb-trigger is assembled concentrically onto the thumb-gimbal, and is held in position using a compression spring and two locking pins, creating a prismatic joint. The compression spring acts to elongate the thumb-trigger and thumb-gimbal assembly, while the locking pins limit their maximum separation and constrain their relative motion along their long axis. The thumb-trigger also includes a cable fixture point comprised of a set-screw clamp which is used to anchor the actuation tendon controlling the end-effector. While stabilizing the control handle assembly in their hand, using their index middle and ring fingers, the surgeon operator places their thumb onto the thumb-trigger. Depressing the thumb trigger activates opening the end-effector, while flexing and extending their thumb pivots the thumb-gimbal to pitch the instrument tip, as shown in Fig. 6.2.

6.3.4 Instrument Prototyping

An ANI prototype was fabricated using a combination of 3D-printing, laser welding and laser cutting. Fig. 6.4 outlines the major components of the instrument assembly and Fig. 6.2 depicts the assembled prototype. In this version, the rigid segment of the tube-shaft is stainless-steel which is laser welded using a iWeld 990 industrial micro-laser-welder (LaserStar Technologies, USA) to the compliant region. The compliant tube-shaft segment is constructed from a nickel-titanium alloy Nitinol (NDC, Confluent Medical Technologies, USA). The contact-aided notched-tube joint profiles, the anchor points for the actuation tendons and the profile for the attachment region for the end-effector at the tube-shafts tip were laser cut (Pulse Systems, USA). The actuation tendons routed within the tube-shaft consist

of braided stainless-steel (Sava Inc., USA) and are laser welded distal to the compliant joint region. The end-effector in the prototype was recycled from disposable medical instruments, and the pin-joint mechanism fastening these tips to the tube-shaft were assembled by laser welding.

The instrument shaft diameter, length and the cutting pattern for the steerable tip were selected based on the design requirements outlined in [9], which proposes design specifications for steerable instruments specific to the ETV-ETB procedure. These features are summarized in Table 6.1 and the specific geometry features unique to the notch profile are summarized in Fig. 6.5-A. Specifically, the notch profile is described using the geometry variables S , w , h , G , R , ξ and η which are detailed in section 6.4.1. Further, section 6.5 compares the performance of the selected geometry to the requirements outlined in [9].



Figure 6.4: Primary components used to assemble the instrument control handle

The threaded collect mechanism, handle-base, handle-gimbal and handle-trigger were fabricated using stereolithography with a Form2 3D-printer (Form Labs Inc., USA). These components were assembled using stainless-steel fasteners (McMaster-Carr, USA).

Table 6.1: Summary of Instrument Shaft Geometry

Feature	Geometry
Instrument Shaft Outer Radius (r_o)	0.62 mm
Instrument Shaft Inner Radius (r_i)	
Notch Variable S	0.6 mm
Contact-Aid Radius R	0.2 mm
Notch Spacing w	0.5 mm
Notch Height h	1.65 mm
Notch Depth G	1.11 mm
Number of Notches	4
Notch Lower Taper Angle γ	20
Notch Upper Taper Angle φ	50

6.4 Kinematic Analysis

A kinematic model for the notched-tube compliant joint was developed in [19]. In this paper, the model is combined with the three additional DOF and the geometry of the articulate neuroendoscopic instrument prototype to predict the tools reachable workspace. The reachable workspace is then compared to the results of [10] that predicts the shape and size requirements for steerable neuroendoscopic instruments in combined ETV-ETB procedures for a range of patients.

6.4.1 Kinematic Model and Frame Convention

The ANI is capable of achieving four degrees-of-freedom. Assuming the tool is constrained from moving laterally because of a trocar, the surgeon can control the roll of the instruments shaft (θ_1), the stroke of the tool into and out of the working channel (l_2), the pitch of the instrument's tip (θ_3), which includes a small joint offset described by the variables h , S and w , and actuation of the instruments end-effector (l_4).

The reachable workspace of the instrument is expressed with respect to the coordinate system of the tip of the neurosurgical trocar C_0 , where the z-axis is aligned longitudinally with the trocar and the y-axis is aligned with the bending axis of the notches. The notation used to describe the kinematics of the tool tip is depicted in Fig. 6.5-A.

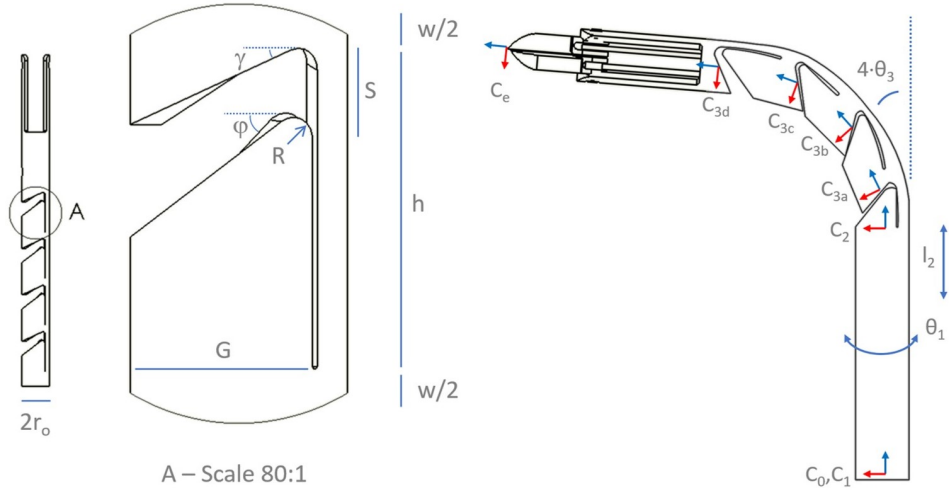


Figure 6.5: A Contact-Aided Compliant Joint Design (A); Steerable Instrument Tip with Kinematics Frames (B)

To implement the kinematics model, the stroke and instrument roll DOF controlled by the user are expressed by the following combined transformation matrix:

$$T_2^0 = \begin{bmatrix} c(\theta_1) & -s(\theta_1) & 0 & 0 \\ s(\theta_1) & c(\theta_1) & 0 & 0 \\ 0 & 0 & 1 & l_2 \\ 0 & 0 & 0 & 1 \end{bmatrix} \quad (6.1)$$

where the transformation T_2^0 represents a mapping from the origin coordinate system C_0 to the coordi-

nate system attached to the base of the first compliant notch C_2 . The roll of the instrument is described using the joint variable θ_1 and the stroke joint variable is l_2 . The functions $c()$ and $s()$ represent the functions cosine and sine, respectively.

The compliant joint segment of the tube-shaft represents a combined rotation and translation motion, which is approximated based on the geometry of the notched-tube cutting pattern as shown in Fig. 6.5-A. The motion of an individual notch is expressed by the following combined transformation matrix:

$$T_3 = \begin{bmatrix} c(\theta_3) & 0 & s(\theta_3) & (R - G + r_o) \cdot (c(\theta_3) - 2c^2(\theta_3) + 1) + 2c(\theta_3)s(\theta_3)(S - R\theta_3) \\ 0 & 1 & 0 & 0 \\ -s(\theta_3) & 0 & c(\theta_3) & w - S - R + h + (R - G + r_o) \cdot (s(2\theta_3) - s(\theta_3)) + c(2\theta_3) \cdot (S - R\theta_3) \\ 0 & 0 & 0 & 1 \end{bmatrix} \quad (6.2)$$

where T_3 is a mapping from the base of the notch to the tip of the notch, for example from coordinate system C_2 to coordinate system C_{3a} . Here, the joint variable θ_3 represents the bending angle of a single notch, and R , G , S , h , w , and r_o are constants representing the geometry of the notch.

The offset between the last notch and the tip of the end-effector is described using:

$$T_e = \begin{bmatrix} 1 & 0 & 0 & 0 \\ 0 & 1 & 0 & 0 \\ 0 & 0 & 1 & e \\ 0 & 0 & 0 & 1 \end{bmatrix} \quad (6.3)$$

where T_e is a linear translation along the z-axis of the instrument by e , which is a constant value that depends on the geometry of the tool and end-effector. These transformations can be combined to describe the mapping from the trocar tip to the instrument tip as:

$$T_e^0 = T_2^0(T_3)^n T_e \quad (6.4)$$

where the superscript n represents the number of notches used in the compliant joint region of the tube-shaft. The coordinate frames generated using this kinematics model are superimposed on the schematic in Fig. 6.5-B.

6.4.2 Validation of Kinematics Model

The accuracy of the kinematics model was assessed with two Flea3 1.3 MP cameras (Point Grey, Vancouver Canada) arranged in a stereo-configuration and calibrated using the MATLAB Camera Calibration Toolbox. The shape, bending angle and tip position of the steerable instrument was tracked with the cameras while an OptoNCDT 1607 time-of-flight laser displacement sensor (Micro-Epsilon, USA) was used to track the actuation tendon. The error of the camera measurement system is in the range of [0.01-0.1] mm. The experimental set-up is shown in Fig. 6.6-A.

The position of the instrument tip has been directly compared to the kinematics model in Fig. ??-B. Here, nine discrete tendon displacements ($\delta l = \{0, 0.25, 0.5, 0.75, 1, 1.25, 1.5, 1.75, 2\}$ mm) were assessed and the resulting X-Y coordinates of the physical joint specimen and the predicted kinematics positions

are shown. The root-mean-square-error, represented as a Euclidean Norm of the expected and actual tip position, for the trajectory values was found to be ± 1 mm.

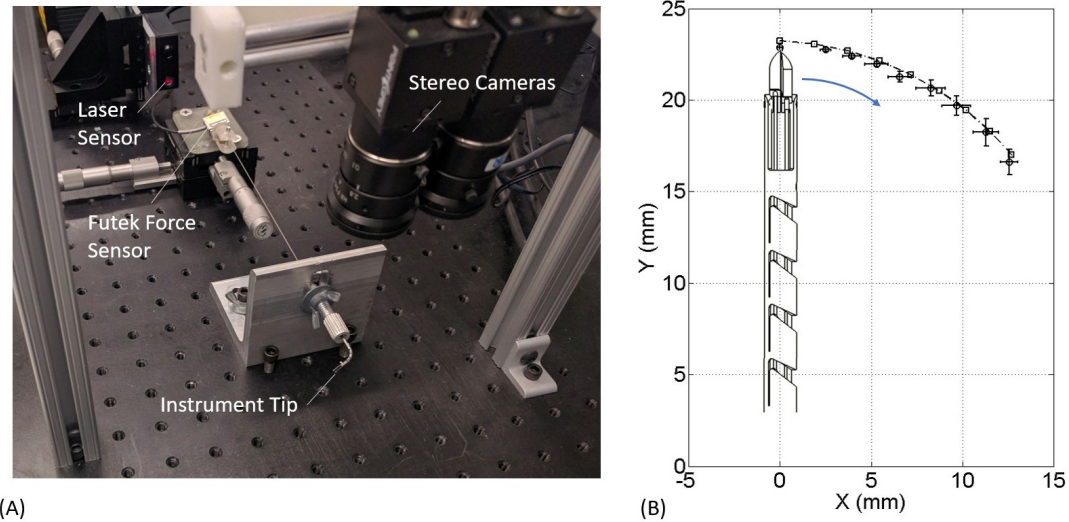


Figure 6.6: Place Holder for Kinematics Experiments

6.5 Task Specific Analysis of ANI Performance

Following the validation of the kinematics model, the performance of the ANI prototype was compared to the design requirements developed from the patient specific ETV-ETB surgery data in [9]. The ANI was assessed using two methods: First, the ANIs joint length and radius of curvature was compared to the values predicted in [9]. Second, the reachable workspace of the ANI, generated using the kinematics model, was superimposed onto the 3D models of the patient anatomy from [9]. With this approach, the percentage of reachable workspace was measured for both the ETV and ETB surgical tasks, over a range of representative patient anatomies.

6.5.1 Patient Data

As discussed in [9], a review of surgical cases performed at the Hospital for Sick Children in Toronto, Canada between 2006 and 2014 was completed. This review identified fifteen patients (9 male and 6 female) with suitable computed tomography (CT) and magnetic resonance (MR) data who underwent successful or attempted simultaneous ETV and ETB procedures. The imaging data was converted from DICOM format into STL models of the surgical workspace using MIMICS and 3-Matics (Materialise, Ghent, Belgium), and two neurosurgeons selected target points identifying the ETV site and the tumor. The use of patient information was approved for this study by the Ethics Review Committee of The Hospital for Sick Children.

The analysis outlined in [9] was used to predict the shape and size requirements of a simulated hypothetical steerable neuroendoscopic instrument as well as optimal trocar trajectories.

6.5.2 Comparison of ANI Geometry to Design Requirements

The patient specific simulations of ETV and ETB procedures described in [9] were used to establish estimates of the shape of a hypothetical dexterous neuroendoscopic instrument. This hypothetical instrument was approximated as a constant curvature arc described using a predicted arc-length S_p and predicted radius of curvature R_p . Considering all fifteen patients in the dataset, the mean and range values found for the predicted shape are summarized in Table 6.2. For comparison, the shape parameters for the ANI tool are also summarized. Since the ANI tool includes additional features, such as an end-effector, there is not a one-to-one correspondence between predicted geometry and ANI geometry. For clarification, Fig. 6.7 illustrates the values being compared in Table 6.2.

Table 6.2: Comparison of Design Specifications to ANI Geometry

Units in (mm)	Predicted Values ($_p$) [9] Mean [Range]	Values for ANI ($_{ANI}$) [Range]
Arc Length S	33.2 [26.1 41]	18 + 10 (end-effector)
Radius of Curvature R	47.5 [26.3 66.3]	[8.8]

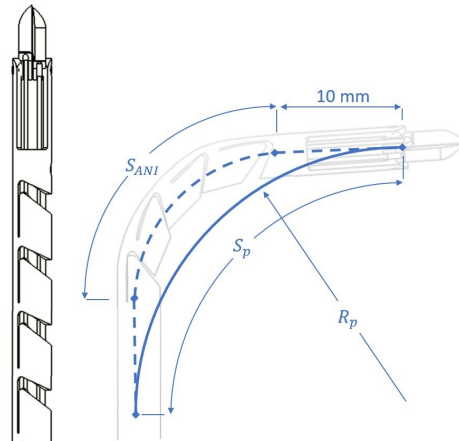


Figure 6.7: Predicted vs ANI Geometry

To summarize, the ANI instrument can achieve a range of bending radii that encompass the predicted values. Further, the joint length of the ANI, including the end-effector, lies within the range of predicted arclengths found in [9].

6.5.3 ANI Reachability Assessment

To further assess the ANI with respect the patient data in [9], the reachable workspace was superimposed onto the patients 3D anatomy models. Using the kinematics presented in section 6.4.1, the reachable workspace of the ANI was generated in MATLAB based on the joint values summarized in Table 6.3. This volume data was imported into 3-Matics (Materialise, Ghent, Belgium) in the form of an STL. Similarly, STL files representing a neurosurgical trocar, the patients skull, cerebral ventricles and tumor were also imported. The trajectory and position of the neurosurgical trocar and the ANI workspace model were positioned according to the optimal trajectories determined in [9]. The trocar used in this simulation is assumed to have a neuroendoscope with a 30° viewing angle.

Table 6.3: Simulated Joint Value Ranges

Joint Value	Range
Stroke	0 mm - 20 mm
Roll	180°
Pitch	0° – 90°
End-Effector	Open/Close

The Boolean Intersection tool and the Markup tools in 3-Matics were used to measure the volumetric overlap of the instruments reachable workspace compared to the floor of the third ventricle and the tumor. These measurements are used to provide a relevant approximation of the reach of the tools inside of a clinical work environment. Fig. 6.8 demonstrates an example measurement taken with the patient data.

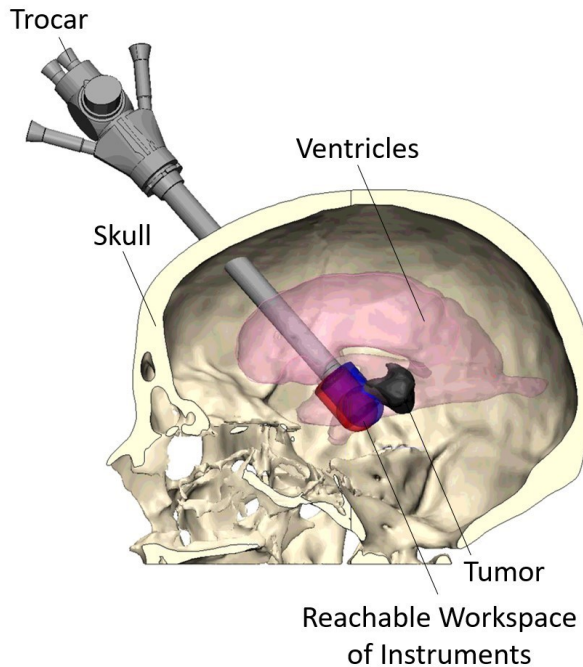


Figure 6.8: Simulation of Reachable Workspace of Instruments for Performing a Combined ETV-ETB Procedure

The results of the simulation, completed on all fifteen patients, indicates that 100% of the area of the floor of the third ventricle is reachable by the ANI and $56 \pm 4\%$ of the tumor volume is reachable. This analysis assumes that the trocar is held in a "collision-free" fixed position. The trocar placement trajectory used in this study is identical to the established Split-the-Difference technique described by Knaus et al. in [5].

6.6 Surgical Task Simulation

To further assess the performance of the ANI prototype, a simulated ETV-ETB surgery was performed. The experimental setup is shown in Fig. 6.9. For this experiment, a synthetic brain simulator, designed and validated for teaching neuroendoscopy, was used [20]. A Hopkins 2.7mm x 20cm 30° neuroendoscope (Karl Storz) was held in place using an articulated stand holding system, passed through a 6 mm diameter

operating sheath, used in lieu of a trocar. An Olympus camera system and light source with an OTV SP1H-NA-12E PAL camera head were used to acquire images.

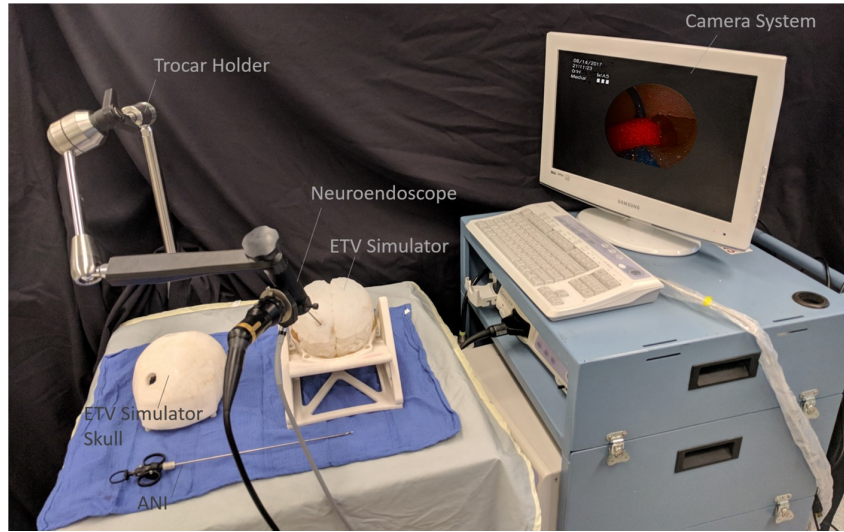


Figure 6.9: Simulation set-up used for ANI validation in ETV-ETB simulator

6.6.1 Surgical Task Results

As shown in Fig. 6.10, the ANI instrument is capable of reaching "around corners" and through anatomical obstacles such as the foramen of Monro. In panel (A) and (B), the endoscope was held further away from the surgical target in order to better appreciate the shape of the ANI. Panel (C) depicts the instrument biopsying the tumor and panel (B) shows the tool reaching the floor of the third ventricle. In this simulation, a 30° angled endoscope was held in place and first used to view the anterior aspect of the third ventricle to perform a ventriculostomy. Then, holding the position of the endoscope fixed and rotating its view, the ANI tool was used to reach and biopsy the pineal tumor.

6.7 Discussion

This work presents the development of a new neuroendoscopic instrument using a patient specific, data-driven approach. The articulate neuroendoscopic instrument (ANI) was designed and built based on the specifications set-out by [9], a prior study that focused on tool design optimization for endoscopic third ventriculostomy (ETV) and tumor biopsy (ETB). We begin by presenting the major components of the ANI, including the assembly of the instrument handle and the wristed tube-shaft. Next, the fabrication process, using laser machining and 3D-printing is discussed. Section 6.4 outlines a kinematics model for the ANI and presents an experimental validation completed to assess the limitations of this model. Following this assessment, the proceeding sections directly compare the ANIs function to the design specifications set-out in [9]. This assessment is completed in three parts. First, the geometry of the ANIs wrist was measured and the bending radius and joint length was compared to the predicted values from [9]. The ANI achieves a range of bending radii that encompass the predicted values and its joint length combined with the length of its end-effector is similar to the predicted joint length. However,

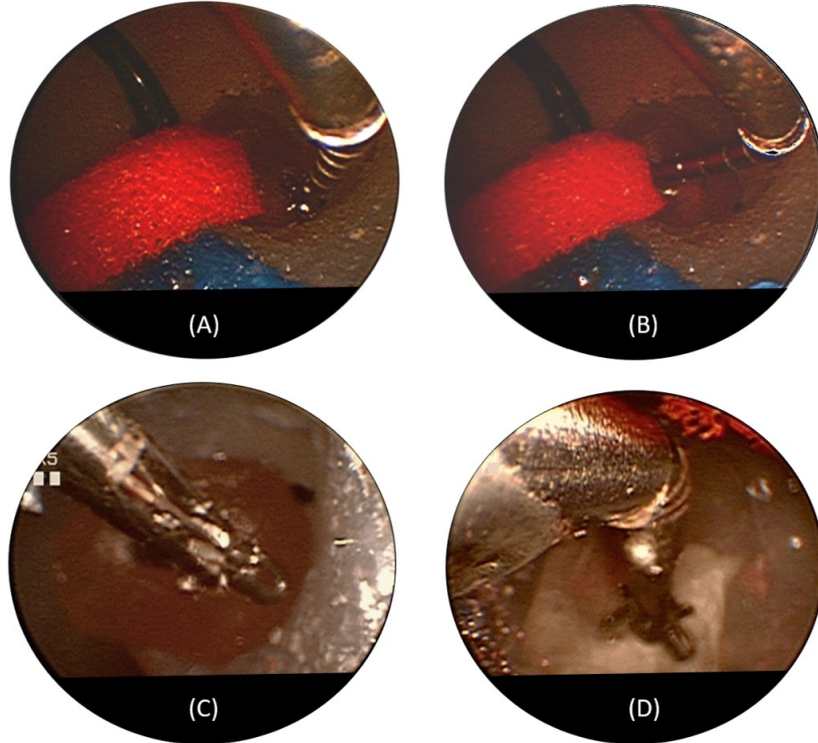


Figure 6.10: View of ANI through 30° neuroendoscope reaching through foramen of Monro to biopsy Pineal tumor

since the predicted and actual shapes deviate, the kinematics model was used to generate the reachable workspace of the tool and a second analysis was completed using this data. The workspace of the ANI was superimposed over each of the 3D-patient models used in the original data-set from [9], and the percentage coverage of the surgical targets were measured. The ANI was found to have 100% coverage of the ETV targets and 56% coverage of the tumors. Finally, the ANI tool prototype was assessed with a physical ETV-ETB simulator. In this simulation, the ANI was used to reach the tumor and the floor of the third ventricle in a physical model of a patient with hydrocephalus and a pineal region tumor. Overall, the ANI demonstrates a significant improvement in the achievable instrument reach compared to standard tools. The ability to access multiple targets, collision-free, is not possible using convention tools which require the surgeon to reposition the trocar during operation.

In terms of its design, the ANI has the following limitations. First, the instrument shaft has many openings that will need to be enclosed or protected in the future to make the device suitable for live-animal or human use. Second, the fabrication techniques used to develop the prototype are not sterile, and must be updated in the future for clinical testing. In particular, methods used to laser cut and laser weld components are subject to contamination, and the 3D printing material is not currently serializable. Third, the flexible tip is at risk of failure from fatigue, and presently, it is not easily interchangeable if broken. Finally, the increased reach of the ANI has the benefit of improving a surgeon's ability to use two instruments to perform bi-manual maneuvers. For example, grasping tissue with one tool and cutting the tissue with another tool. However, with the current design, if the handles are too close together, the user's hands may collide. Therefore, to make the ANI more ergonomic, a new trocar design may be required to maximize its potential benefits, instead of using it with a plain introducing sheath.

The experimental assessments conducted on the ANI included the following limitations: First, the measurements comparing the design of the ANI to the specifications set-out in [9], are subject to the bias from the methods used in [9]. For example, the selection of the target points for the ETV and ETB sites are somewhat subjective and biased by the neurosurgeons selecting the targets. Second, the "optimal" positioning of the trocar is based on the appropriate selection of surface landmarks on the surface of the skull. Identifying these landmarks is also subject to human error. These factors contribute to some uncertainty about the exact position of the target points, which also contribute to uncertainty in the predicted shape of the tool. These variabilities partially explain why the ANIs actual geometry and the predicted geometry requirements in [9] do not perfectly match, as seen in Section 6.5.2. Using two neurosurgeons to select the target points, and using multiple patients in the data-set, help to mitigate these uncertainties but do not eliminate them. Additionally, the approach in [9] does not consider the instrument tip's orientation when analysing the workspace. This limitation arises from the difficulty in conceptually defining orientation constraints in a computer simulation. To address these issues, the ANI was also assessed by comparing its reachable workspace to the surgical workspace and also by a physical simulated surgery. All three of these experiments were interpreted together to assess the performance o the ANI.

The results of the shape comparison in Section 6.5.2 are further challenging to interpret because the ANI is capable of reaching the ETV-ETB targets, despite not having a one-to-one correspondence with the predicted shape. The initial assumption used in [9] to approximate the shape of the tool overly simplified the problem. For example, it did not consider the attachment of an end-effector, since the exact shape of end-effectors can be variable. As well, the shape assumption did not consider the possibility that the tool may take on non-constant curvatures. However, without this data as a starting point, it would be difficult to understand the shape and size constraints associated with ETV-ETB, and use this information to select a technology with which to build the tool. Particularly for neuroendoscopy, finding an actuation technology that is small and compact enough to fit into the surgical workspace is challenging. Combining these constraints with the forces required to manipulate brain tissue results in a significant design challenge. Specifically, the need for a joint design that can be easily miniaturized, and that is both stiff and capable of compact bending, led to the development of the novel contact-aided notch tube-shaft design presented in [19].

A second limitation of the experimental methods pertains to the kinematics model. The tip-position-error discrepancy between the kinematics model and the physical tools reachable workspace introduces uncertainty in the reachability assessment of Section 6.5.3. The percentage coverage of the surgical targets by the tool is affected by the position error of ± 1 mm. It can be estimated that the reachable volume of the instrument can vary by up to $\pm 14\%$ and therefore the estimates of the percent coverage of the surgical workspace may be affected. The tip position error is affected by both the assumptions inherent to the kinematics model and the set-up used to collect the experimental results. First, the model which is adapted from [19], uses a simplified geometric approach to predict the bending of the notches and assumes that the majority of bending occurs around the contact-aid region. In the future, developing a kineto-static model using an approach such as the pseudo-rigid-body-model may reduce errors by more closely matching the deformation of the contact-aid region. Another source of error is in the experimental set-up shown in Fig. 6.6. The samples were aligned in the specimen fixation clamp manually and therefore their alignment was not completely orthogonal to the plane of the optical breadboard. A stereo-camera measurement system was used to minimize this error in order to capture

out-of-plane bending. However, the uncertainty in the measurements taken using the camera still ranged from $\pm [0.01\text{-}0.1]$ mm.

Considering these limitations, the physical surgical simulation assessment was completed to complement the first two bench-top evaluations. The physical simulations of the instruments in the synthetic brain model demonstrate that the surgeon-operator now has the ability to reach across the field of view of the camera and target both the ETV and ETB sites following a non-linear trajectory. This capability is not feasible using conventional tools, and it significantly contributes to the goal of allowing neuro-endoscopes to dissect in the same manner as conventional microsurgery. In practise, the trocar undergoes small movements which will further increase the reach of the tool in combination with the wrist joint. Therefore, the results of the first two bench-top evaluations, based on the constraint of holding the trocar fixed, give a very conservative estimate of the tools coverage of the surgical workspace. Nevertheless, these assessments are useful because they help to assess how closely the final design agreed with the initial design specifications. Further, they highlight improvements that can be made to future studies aimed at elucidating design specifications for neurosurgical instruments.

Future work for this project will focus on collecting user-feedback from expert surgeons as they perform a series of simulated surgical tasks while using the new instruments. This study will use a mixed-methods design, and consider the use of the tools in basic bench-top pick-and-place maneuvers and also compare their performance to using standard instruments when operating on the synthetic brain simulator.

6.8 Conclusion

The ANI demonstrates a significant improvement in the achievable instrument reach compared to standard tools. The simulations and physical experiments indicate that both ETV and ETB targets sites are reachable from a fixed trocar position for a wide range of anatomies encountered in a series of patients. This collision-free result is not possible using convention tools which require the surgeon to reposition the trocar during operation.

6.9 References

- [1] A. Grotenhuis, Neuroendoscopic Instruments and Surgical Technique, in *Neuroendoscopy*, 2014, pp. 8191.
- [2] M. R. Gaab, Instrumentation: Endoscopes and equipment, *World Neurosurg.*, vol. 79, no. 2 SUPPL., p. S14.e11-S14.e21, 2013.
- [3] P. F. Morgenstern, N. Osbun, T. H. Schwartz, J. P. Greenfield, A. J. Tsioris, and M. M. Souweidane, Pineal region tumors: An optimal approach for simultaneous endoscopic third ventriculostomy and biopsy, *Neurosurg. Focus*, vol. 30, no. 4, pp. 15, Apr. 2011.
- [4] P. F. Morgenstern and M. M. Souweidane, Pineal region tumors: Simultaneous endoscopic third ventriculostomy and tumor biopsy, *World Neurosurg.*, vol. 79, no. 2, pp. 913, 2013.
- [5] H. Knaus, S. Matthias, A. Koch, and U.-W. Thomale, Single burr hole endoscopic biopsy with third ventriculostomy-measurements and computer-assisted planning, *Childs Nerv. Syst.*, vol. 27, no. 8, pp. 12331241, Aug. 2011.
- [6] X. L. Zhu, R. Gao, G. K. C. Wong, H. T. Wong, R. Y. T. Ng, Y. Yu, and R. K. M. Wong, Single burr hole rigid endoscopic third ventriculostomy and endoscopic tumor biopsy: What is the safe displacement range for the foramen of Monro?, *Asian J. Surg.*, vol. 36, no. 2, pp. 7482, 2013.
- [7] L. Qiao and M. M. Souweidane, Purely endoscopic removal of intraventricular brain tumors: A consensus opinion and update, *Minim. Invasive Neurosurg.*, vol. 54, no. 4, pp. 149154, 2011.

- [8] H. J. Marcus, T. P. Cundy, A. Hughes-Hallett, G.-Z. Yang, A. Darzi, and D. Nandi, Endoscopic and keyhole endoscope-assisted neurosurgical approaches: A qualitative survey on technical challenges and technological solutions., *Br. J. Neurosurg.*, vol. 28, no. August 2013, pp. 15, 2014.
- [9] K. W. Eastwood, V. P. Bodani, and J. M. Drake, Three-dimensional simulation of collision-free paths for combined endoscopic third ventriculostomy and pineal region tumor biopsy: Implications for the design specifications of future flexible endoscopic instruments, *Oper. Neurosurg.*, vol. 12, no. 3, pp. 231238, 2016.
- [10] H. Fischer, B. Vogel, W. Pfleging, and H. Besser, Flexible distal tip made of nitinol (NiTi) for a steerable endoscopic camera system, *Mater. Sci. Eng. A*, vol. 273275, pp. 780783, 1999.
- [11] J. Peirs, H. Van Brussel, D. Reynaerts, and G. De Gersem, A Flexible Distal Tip with Two Degrees of Freedom for Enhanced Dexterity in Endoscopic Robot Surgery, in *The 13th Micromechanics Europe Workshop*, 2002, pp. 271274.
- [12] M. D. M. Kutzer, S. M. Segreti, C. Y. Brown, R. H. Taylor, S. C. Mears, and M. Armand, Design of a New Cable-Driven Manipulator with a Large Open Lumen: Preliminary Applications in the Minimally-Invasive Removal of Osteolysis, in *IEEE International Conference on Robotics and Automation*, 2011, pp. 29132920.
- [13] S. C. Ryu, P. Renaud, R. J. Black, B. L. Daniel, and M. R. Cutkosky, Feasibility Study of an Optically Actuated MR-compatible Active Needle, in *IEEE International Conference on Intelligent Robots and Systems*, 2011, pp. 25642569.
- [14] Y. Haga, Y. Muyari, S. Goto, T. Matsunaga, and M. Esashi, Development of Minimally Invasive Medical Tools Using Laser Processing on Cylindrical Substrates, *Electr. Eng. Japan*, vol. 176, no. 1, pp. 6574, 2011.
- [15] J. A. Bell, C. E. Saikus, K. Ratnayaka, V. Wu, M. Sonmez, A. Z. Faranesh, J. H. Colyer, R. J. Lederman, and O. Kocaturk, A Deflectable Guiding Catheter for Real-Time MRI-Guided Interventions, *J. Magn. Reson. Imaging*, vol. 35, no. 4, pp. 908915, 2012.
- [16] D. Wei, Y. Wenlong, H. Dawei, and D. Zhijiang, Modeling of Flexible Arm with Triangular Notches for Applications in Single Port Access Abdominal Surgery, in *IEEE International Conference on Robotics and Biomimetics*, 2012, pp. 588593.
- [17] J. Liu, B. Hall, M. Frecker, and E. W. Reutzel, Compliant articulation structure using superelastic NiTiNOL, *Smart Mater. Struct.*, vol. 22, no. 9, 2013.
- [18] P. J. Swaney, P. A. York, H. B. Gilbert, J. Burgner-Kahrs, and R. J. Webster III, Design, Fabrication, and Testing of a Needle-sized Wrist for Surgical Instruments, *ASME J. Med. Devices*, no. c, 2016.
- [19] K. W. Eastwood, P. Francis, H. Azimian, A. Swarup, T. Looi, J. M. Drake, and H. E. Naguib, Design of a Contact-Aided Compliant Notched- Tube Joint for Surgical Manipulation in Confined Workspaces, *J. Mech. Des.*, vol. Accepted, 2017.
- [20] G. E. Breimer, V. Bodani, T. Looi, and J. M. Drake, Design and evaluation of a new synthetic brain simulator for endoscopic third ventriculostomy., *J. Neurosurg. Pediatr.*, vol. 15, no. 1, pp. 828, Jan. 2015.

Chapter 7

Future Directions for Contact-Aided Notch-tube Compliant Joints

7.1 Overview

This chapter summarizes the key results of this thesis, outlines the major obstacles and limitations of the work, and proposes future directions for the project. The first sections of the chapter will describe the limitations of the current design, followed by a description of the next steps including multi-instrument applications, navigation and procedure planning, biocompatibility and commercialization. The end of the chapter synthesizes the main concepts from each of these topics, and proposes future studies that will move the project towards addressing these next-steps.

7.2 Overview of Contributions and Limitations of Proposed Technology

7.2.1 ETV-ETB Specific Articulate Neuroendoscopic Instruments

The device developed in this study was specifically designed to increase the reach of the instruments used to perform a combined endoscopic third ventriculostomy (ETV) and endoscopic tumor biopsy (ETB). Although this procedure is not extremely common, the challenges encountered during this surgery highlight the limitations of current standard neuroendoscopic equipment. Specifically, that there is an interrelationship between the reach and dexterity of the tools, and the safety and feasibility of performing the procedure. Small, anteriorly located pineal region tumors are more likely to be accessible through a single burr-hole, compared to larger posteriorly located tumors, based in part by what is reachable in a straight-line direction by the instruments.

In this work, we have developed a compact joint design capable of increasing the reach of neuroendoscopic tools, with the aim of allowing surgeons to biopsy or excise larger tumors located more posteriorly in the third ventricle. Through increasing the dexterity of the instrument tip, the need to reposition the endoscope during surgery can be reduced. Displacement of the endoscope/trocar during operation places pressure on surrounding healthy brain tissue, causing ischemia and potentially permanent damage. This

factor is one of the considerations surgeons use when planning an operation, and can determine whether the tumor can be safely accessed.

The proposed mechanism is based on a monolithic design, which reduces the number of micro components needed build the joint and the complexity of its assembly. These benefits allow for more cost-effective scaling of the joint to submillimeter sizes compared to traditional revolute pin-joint mechanisms. Further, the design is based on laser-machining fabrication, which is commonly used to make medical stents and catheters. This technology allows production to be easily scaled-up in terms of quantity and already has measures in-place to ensure the components are sterile and biocompatible. Many different notch-tube compliant joint mechanisms have been described for other medical applications, however, the mechanism presented here incorporates contact-aids for the first time. The contact-aids allow this joint to undergo sharp and compact bends while also retaining stiffness so that the mechanism can transmit adequate joint forces when manipulating tissue. Many previous notch-tube compliant joints were implemented in laser or camera-steering applications that do not involve bearing externally applied loads. Thus, many of the existing notch-tube compliant joint designs are prone to unacceptable deformation when manipulating tissue.

This thesis demonstrates a patient specific, data-driven approach to the development of a neuroendoscopic instrument. A set of patients with neuroanatomies representative of the surgical workspace typically encountered during ETV-ETB were identified. These workspaces were studied to predict the ideal shape and reach of a dexterous neuroendoscopic tool, and this data was used to identify and select the notch-tube compliant joint technology for further development. The inherent trade-off between range-of-motion and joint stiffness for notch-tube joints was analysed in the context of the forces and workspace requirements of neuroendoscopy. This analysis led to the identification of the need for contact-aids to reinforce the joint design. Following this discovery, a contact-aid joint was developed and incorporated into a neuroendoscopic instrument with an articulate tube-shaft. In parallel with this process, a new handle mechanism was developed, using input from neurosurgeons at the Hospital for Sick Children, and the handle and tube-shaft were combined into a working prototype instrument. This prototype was then assessed in bench-top experiments to compare its function to the design specifications elucidated from the initial patient data-set. This development process has been iterative, and based on these assessments, the present prototype has limitations that must be addressed.

The experiments in the previous chapter where the instrument is used in a simulated ETV-ETB surgery highlight functional limitations that were not considered in the computer simulations used to develop the initial design specifications. Specifically, the maximum outer diameter of the instrument was selected as 2 mm based on the design of existing neuroendoscopic tools. However, added dexterity of the instrument tip creates visibility problems where the tool shaft blocks the field of view as it articulates. Therefore, there is still significant need to reduce the diameter below $\pm 1\text{mm}$ to increase visibility and see around the instrument shaft. As well, during operation, surgeons may wish to reposition the camera closer to target site than initially anticipated in the computer simulations. For example, to better inspect the operating environment. Moving the trocar closer to the surgical target increases the need for more compact bending in the joint even further. Therefore, the required bending radii for ETV-ETB procedures may be closer to the smaller end of the range predicted by the initial computer simulations. Finally, during the development of these tools, a significant amount of information qualitative feed-back was collected from neurosurgeons. One of the most common issues brought forward is the need to add a roll mechanism to the end-effector to change its orientation during operation.

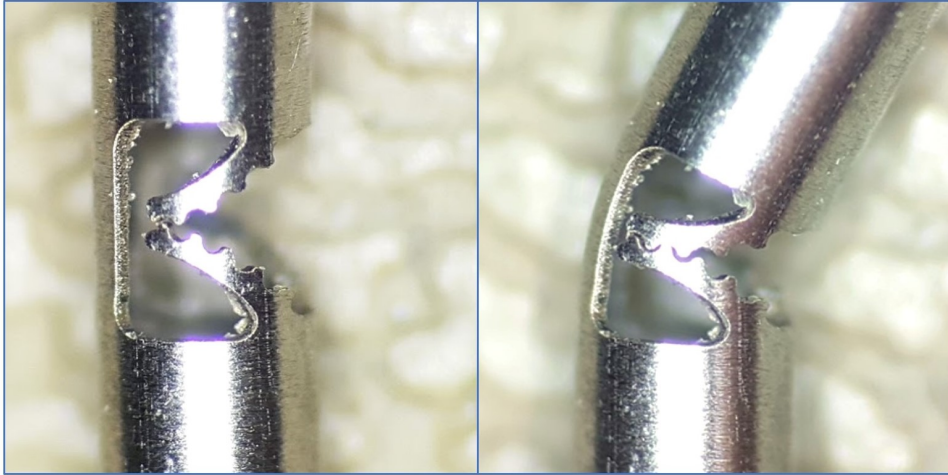


Figure 7.1: Proposed future contact-aided notch-tube compliant joint addressing limitations of current prototypes

These factors should be taken into consideration as future design cycles are continued for the development of ETV-ETB specific instruments.

7.2.2 Notched-Tube Contact-Aided Compliant Joints

Considering the future development of contact-aided compliant notch-tube joints as a whole, there are several limitations that should be addressed. First, there is a significant strain concentration that occurs at the contact-point between the contact-aid and compliant joint region. This effect limits the fatigue life of the joint and may also limit a given notches total elastic bending. The experimental fatigue life of the proposed joints in this thesis range between 1800-2000 full range-of-motion articulations before failure. Second, the present design requires complex modelling techniques be implemented to capture the non-linear material properties and contact-aid behavior, as well as, the large deflections of the compliant joint beam. Third, the present contact-aid geometry poses some fabrication challenges using laser cutting because it requires off-axis alignment of the laser. The theoretical design of the joint requires the cut be made in a direction parallel with the axis of rotation of the joint. This cutting configuration cannot be directly achieved using the conventional laser cutting techniques implemented for cutting stents. Instead, the cutting direction must deviate greater than 15° from the axis of rotation of the joint. With this compromise, there is still some thermally induced plastic deformation of the compliant joint region, and the possibility that the contact-aid and compliant joint region slip during contact.

One possible future direction for implementing contact-aided notched tube compliant joints is to investigate the performance of the geared compliant mechanism shown in Fig. 7.1. This design includes features that are hypothesized to specifically address many of the limitations of the first-generation design.

The geared tooth design is similar to the first-generation design in that it relies on a contact-aid that reinforces the joint and provides increased joint stiffness throughout its range-of-motion. However, the gear shape and teeth are designed to provide a more predictable bending motion that can be accurately anticipated in manner that may simplify and decouple its kinematics and statics models. This feature may increase the accuracy of using analytical models for predictive design. Further, this geared prototype

is designed such that the contact-aids act in parallel with the compliant bending region of the joint, instead of directly contacting it. This feature may significantly increase fatigue life by removing the strain concentration that occurs between the contact-aid and the compliant region. Finally, designing the contact-aid in this gear shape also improves the manufacturability of the joint. These contact aid features can be fabricated through laser cutting on-axis which follows established and conventional laser machining practises used in stent design.

7.2.3 Instrument Handle Design

The major contributions of this thesis focus on the development the dexterous tube-shaft of the neuroendoscopic instrument. However, the instruments handle design is just as important as the wristed shaft. In particular, the usability and ergonomics of the handle will affect the overall ease-of-use of the tool and this factor will directly affect its adoption by surgeons.

The handle proposed in this thesis was developed based on a series of assumptions that were generated using informal focused interviews, and include the following:

- Surgeons must be able to control the tool using one hand
- The tool should not depend on external stabilization
 - The tool should be stabilized using one hand
 - The tool should not apply forces to the patient in a location other than the intended surgical target
- The tool should be comfortable to hold
- The tool should be comfortable to operate
- The tool should be intuitive to operate
- The tool should be as familiar as possible to existing handle designs
- The tool should have a minimal number of components
- The tools design should minimize the time and cost of assembly

These assumptions were developed based on feed-back from neurosurgeons at the Hospital for Sick Children, however the validity of the assumptions require further investigation. In particular, the statement that the tool should be controlled and stabilized using one hand. This assumption is based on the concern that if the instrument rests on the neuroendoscope or trocar it may unintentionally transmit forces onto the brain. For example, if the instrument is stabilized against the trocar, the trocar may displace and apply pressure to the brain parenchyma. Further, this action and the magnitude of the force may not be easily appreciated by the surgeon while using the equipment. The requirement that the instrument be controlled and stabilized using a single hand significantly constrains the design, and the difficulty of independently controlling multiple degrees-of-freedom using a single hand is well known.

Alternatively, there are several technologies used in laparoscopic surgery and trans-oral surgery that stabilize dexterous manual instruments using the trocar. For example, the SPIDER Surgical System (TRANSENTERIX, USA) and the Flex Robotic System (Medrobotics, USA) both have either fixed or

robotically positioned trocars that are used to stabilize manual instruments. With this approach, the surgeon uses his or her wrist to control the wrist of the instrument, and their fingers to control the end-effector. Future work could consider if this design approach is suitable for neuroendoscopy, and whether the perceived risks of unintentionally displacing the trocar and injuring the brain are likely.

Another assumption of the current handle design is that the instrument should be as familiar as possible to existing neurosurgical handles. The present design was motivated by an amalgamation of the design of flexible biopsy forceps (Olympus Corporation, Japan) and the standard loop handles used in current neuroendoscopic instruments. This approach relies on the fact that these instrument configurations have been thoroughly investigated in terms of ergonomics and human-factors, as well as proven in the market. Further, these designs are familiar to surgeons and therefore lower the learning barriers. Finally, these designs are light weight, employ simple mechanisms and use minimal material. Nevertheless, other custom handle design solutions may exist that are better suited to work with the existing line of neuroendoscopic instrumentation.

7.3 Next Steps in Instrument Development

7.3.1 Multi-Instrument Design Considerations

The instruments developed in this work focus on increasing distal dexterity so that surgeons can reach multiple target points from a single incision. Generally, performing an ETV and ETB procedure may not require multiple instruments be used simultaneously. However, the joint mechanisms presented in here could be configured to better enable bi-manual instrumentation. That is to say, the joints could be used to construct instruments with articulate tips that also triangulate at the trocar tip to reduce instrument-instrument collisions while operating.

One such means of achieving this goal is to arrange multiple joints in series along the tube-shaft such that the distal end of the instrument undergoes an S shaped motion. By achieving this bending shape, the proximal end of the wrist will deviate away from the center-line of the trocar to create space for additional tools, while the distal end of the wrist will curve back towards the trocar midline so that multiple instruments end-effectors can be opposed tip-to-tip. This functionality could allow surgeons to perform more complex maneuvers similar to the techniques used in conventional open microsurgery.

One obstacle to implementing the technology in this manner is determining the total length of the instrument tip that can reasonable extend past the trocar. Each additional joint and degree-of-freedom (DOF) will increase the total length of the tool, and this fact must be balanced against ensuring the tools remain within the field-of-view of the endoscope and within the boundaries of the operative workspace. Another obstacle lies in developing an intuitive and ergonomic means of controlling these additional DOF with a manual handle. The choice of independently controlling the DOF used for triangulation, or coupling them with active DOF is not clear. As well, the choice of articulating these DOF dynamically or statically fixing them in position once the trocar is in place is also non-obvious.

7.3.2 Navigation and Procedure Planning

With the development of new instrumentation capable of following curvilinear paths, new strategies for pre-operative planning and intra-operative navigation is important. There are a variety of technologies

under development focused on continuum robot path-planning, however, these developments do not specifically focus on manual instruments. Some examples include:

7.3.3 Biocompatibility

As discussed, the current prototype is not biocompatible or safe for human use. The following considerations must be addressed to develop a biocompatible version of the tool. First, a new cable anchoring method is needed. The current anchoring design involves soldering the joints actuation cable into an anchoring hole. This approach results in a connection that is weak, not repeatable and includes toxic contaminants. To address this concern, Fig. outlines a slot feature than can be laser-cut into the joint during the machining process. This slot will mechanically anchor the actuation cable inside of the tube-shaft.

Further, to construct a sterile instrument, the laser cutting and laser welding processes used to assemble the end effectors and actuation cables must be done using a sterile system. The machinery currently being used is not set-up in a sterile environment, and uses gas that may contain contaminants.

Additionally, the instruments tube-shaft must be sheathed in a flexible covering, such as a hypotube. This covering will contain the sharp edges of the compliant joint and protect the patient from unintentional injury. Further, the covering will reduce the number of biological contaminants that become lodged inside of the tube-shaft during use. Hypotubes are a family of flexible tube designs that are commonly used in medical device development. These designs are similar to notch-tube compliant joints in terms of their material and fabrication process. For example, hypotubes are commonly constructed from millimeter sized stainless steel or nitinol tubes using laser cutting. However, hypotubes commonly have a continuous spiral cutting pattern that resembles an extension spring, and they are designed to minimize bending stiffness, and therefore are not generally load bearing.

Another important modification that must be addressed includes the materials used for the instrument handle. Presently, the 3D-printed components are not capable of withstanding autoclaving.

These concerns can largely be addressed by identifying vendors capable of producing sterile components. Their machining processes must ensure that contaminants do not enter the material during processing, laser cutting or welding. Further, all raw materials used for construction must come with ISO certification.

Once these concerns have be addressed, a quality assurance protocol, Device Master Record (DMR) or similar must be developed (ISO 13485). This involves creating detailed documentation outlining the fabrication process, all possible failure points and safety concerns for the instruments, as well as risk mitigation strategies. This documentation is required for translating any medical devices into clinical testing, and will be required for Ethics approval for internal testing of the instruments at any hospital.

7.3.4 Education and Training

The development of new instruments, that function differently than standard equipment, require new training methods in order for surgeons to develop comfort and proficiency. As a starting point, the neuroendoscopy simulators used in this thesis for assessment of the instruments can also be employed for practise and training. This process should be iterative, so that feedback can be collected from surgeons to refine and update the tool while the surgeons train in the use and application of the tools.

7.3.5 Intellectual Property and Commercialization

This work was funded in part by the Canadian Institutes for Health Research (CIHR) which actively encourages translation and commercialization of funded projects. In keeping with the goal of translating this technology into practise, a provisional patent was filed on December 16th, 2016 with the United States Patent and Trademark Office (USPTO) entitled FLEXIBLE ARTICULATE SURGICAL TOOL (No. 62/435,439). A full patent application, under the Patent Cooperation Treaty (PCT), has been completed with the assistance of Hill and Schumacher LLP. and will be filed before December 2017.

7.4 Future Research Projects

7.4.1 Neurosurgical Instrument User Feed-back Study

This project focuses on formally collecting qualitative user-feedback from neurosurgeons regarding the functionality of the instrument prototypes. As suggested in the education and training section above, this study will consider the use of the tools in basic bench-top pick-and-place maneuvers and also while using the tools to perform a mock surgery with the neuroendoscopy training simulators. The ultimate goal of this research is to incorporate human factors into the continuing design of the instrument. A study protocol has been submitted and approved by the research ethics committee at the Hospital for Sick Children (REB No. 1000012946).

This single-center study will take place at the Surgical Skills Center of Mount Sinai Hospital (MSH) in Toronto, Canada. The center will provide standard neuroendoscopy equipment to compliment the instruments being tested.

A minimum of 10 participants will be recruited for the user-feedback study and will include neurosurgical residents with varying levels of experience (novice), neurosurgical fellows (experienced) and staff surgeons (experts) from the University of Toronto.

Using a mixed-methods design, all participants will complete a 12-item questionnaire (5-point Likert scales) to rate the design features of the instrument and will also provide open-ended feedback for each item. The survey will also include five separate questions regarding demographics and prior experience, as well as a final open-ended overall impressions section. Specifically, the 12-item questionnaire considers the instrument handles form and feel (Items 1-3), the rating of instruments range-of-motion (Items 4-6), the rating of the cognitive load required for using the instrument (Items 7-9) and ease/difficulty of using the tool alongside existing standard equipment (Items 10-12). The qualitative feedback obtained from the surveys will be organized by the same themes. The responses will be coded and recurring items will be grouped. Any coded items that occurred more than three times will be explicitly tabulated and discussed in the results.

This study will both aid in familiarizing the surgeons with the use of the tools while collecting information to guide future design cycles. The results of this analysis can also be used as further evidence to support funding for this project, and also to cultivate industrial-academic partnerships to aid with translation of the technology. The results of this work could be targeted for publication in the Journal of Operative Neurosurgery and disseminated through conferences such as the Congress of Neurological Surgeons Annual meeting or the Design of Medical Devices (DMD) conference.

7.4.2 Development of a Contact-aided Compliant Joint Robotic Prototype

The majority of this thesis has focused on the applications of contact-aided compliant notch-tube joints for manual instrument development. However, there are a significant number of possible robotic applications that could benefit from this technology. Of particular interest is the integration of this joint into customized tools for the da Vinci Surgical System (Intuitive Surgical, USA). This study proposes the development of a custom roll-pitch-roll wristed tool for the da Vinci research kit (DVRK) using the geared tooth contact-aid notch-tube design.

To implement the geared tooth contact-aid notch-tube design into a robotic mechanism, the behavior of an individual notch must be first studied. Following the methods outlined in chapter 5, the bending angle and cable displacement properties must be measured. Using this data, a kinematics model for an individual notch must be developed, and then extended to a multi-notch joint profile similar to chapter 6. The specific design of this joint lends itself well to using a purely geometric approximation for the kinematics of an individual joint. Following this assessment, the workspace of the joint can be assessed using the DVRK. This analysis will fit well into a robotics conference proceeding such as the IEEE International Conference on Robotics and Automation. This work will follow as a natural extension to this thesis by providing an improved contact-aided notch topology with reduced stress concentrations. The experimental protocol outlined here also extends the work of the Center for Image Guided Innovation and Therapeutic Innovation by building on their experience developing custom instruments for the DVRK.